NON DESTRUCTIVE SURFACE AND SUB-SURFACE MATERIAL ANALYSIS USING SCANNING SQUID MAGNETIC MICROSCOPE

Maria Adamo

DOCTOR OF PHILOSOPHY
AT
UNIVERSITA' DEGLI STUDI DI NAPOLI
FEDERICO II
ITALY
30^{TH} NOVEMBER 2008

UNIVERSITA' DEGLI STUDI DI NAPOLI
FEDERICO II
DEPARTMENT OF PHYSICAL SCIENCES

The undersigned hereby certify the acceptance of the thesis entitled "**Non Destructive Surface and Sub-surface Material Analysis using Scanning SQUID Magnetic Microscope**" by **Maria Adamo** in partial fulfillment of the requirements for the degree of **Doctor of Philosophy**.

Dated: 30^{th} November 2008

PhD Coordinator
Prof. Giancarlo Abbate
Department of Physical Sciences, University of Naples "Federico II"

PhD Coordinator: _____

UNIVERSITA' DEGLI STUDI DI NAPOLI
FEDERICO II

Date: 30^{th} **November 2008**

Author: **Maria Adamo**

Title: **Non Destructive Surface and Sub-surface Material Analysis using Scanning SQUID Magnetic Microscope**

Department: **Physical Sciences**

Degree: **Ph.D.** Convocation: 19^{th} **Dec** Year: **2008**

The research activity described in this thesis was performed at Istituto di Cibernetica of CNR of Pozzuoli (Napoli), where a semi-commercial Scanning SQUID Microscope prototype has been installed in the framework of the regional project "Centro di Competenza Regionale per la valorizzazione e fruizione dei Beni Culturali e Ambientali" (CRdC-INNOVA).

Supervisors
Dr. Ettore Sarnelli and Dr. Roberto Cristiano
Istituto di Cibernetica of CNR of Pozzuoli, Naples (Italy)

Signature of Author

Who has seen the wind?

Neither I nor you:

But when the leaves hang trembling

The wind is passing thro'.

Table of Contents

Abstract

Non Destructive Testing (NDT) based on magnetic technique for the investigation of surface and sub-surface material properties is carried out using a room-temperature sample Scanning Magnetic Microscope. The performances of such instrument are well suited in the field of non destructive evaluation, thanks to the good combination of the spatial resolution and the magnetic field sensitivity of its own superconducting magnetic sensor.

The aim of this work is to show the capability and the advantages of the NDT technique based on Superconducting Quantum Interference Device (SQUID) sensors. We start by describing our Scanning SQUID Microscope in terms of its performances, the different non destructive techniques we can apply to perform the measurements, and the efforts we have done to improve its capability to detect weak magnetic field variations.

Two main applications are presented. On of this is based on the high magnetic field sensitivity of the SQUID sensor at low frequencies, and it consists to excite the sample with an alternating magnetic field (AC). This technique is applied to detect subsurface flaws in paramagnetic samples, for instance, in multilayer structures of aeronautical interest. The other field of application concerns the capability of the sensor to detect, with high spatial resolution, the direct magnetic field (DC) distribution on ferromagnetic samples, due to their residual magnetization. In this way, we can visualize magnetic domain structures of ferromagnetic particles. This capability is also exploited to evaluate the changing of magnetic field distribution in proximity of crack initialization on structural steels, subjected to fatigue cycles.

Acknowledgements

Many people I would like to thank since they followed me during the development of this PhD thesis. I sincerely thank my supervisors, Dr. Ettore Sarnelli and Dr. Roberto Cristiano, for their many suggestions and constant support during this research. In particular, I want to thank Dr. Ettore Sarnelli for his guidance through these years. He always believed in my personal skills and gave me a better perspective on my own results, and finally, he always let me followed my personal aptitudes. Moreover, he offered me a lot of opportunities since I could obtain the best possible results in this research activity.

Dr. Ciro Nappi expressed his interest in my research and gave me his constant help in the theoretical support of this work. He shared with me his knowledge and provided me many useful references and friendly encouragement.

Ing. Massimo Valentino and Dr. Carmela Bonavolontà for their collaboration and useful indications. Mikkel Ejrnaes, Antonio Prigiobbo for useful discussions and Carlo Salinas for his incomparable technical support.

Dr. Antonio Massarotti, director of the *Centro di Competenza Regionale per i Beni Culturali e Ambientali* (CRdC-INNOVA). He believed and supported the development of the high-quality laboratory for non invasive analysis, of which the SSM is an important facility. Dr. Carmen Santagata, since with her acquaintances she have obtained useful archeological samples.

I have the pleasure to thank Daug Paulson and all the guys who work in *Tristan Technologies* in San Diego (CA) for their support of my foreign experience. In particular, I wish to thank Kevin Pratt for his patient support, his encouragement of my work during my period far away from my house, his generosity and friendship.

Of course, I am grateful to my parents for their patience and *love*. Without them this work probably never come into existence.

Finally, I wish to thank the following: my boyfriend Simone (for his love and constant encouragements); my sister Brigida (for helping me); my friends (for their passion and love for the wind and sea), Bill, Matt and Steve (for their singular friendship).

Naples, Italy Maria Adamo
December, 2008

Introduction

In this research activity we present a Non Destructive Testing (NDT) based on magnetic technique for the investigation of surface and sub-surface material properties. NDT methods allow to examine materials or components, to detect, locate, measure, and evaluate discontinuities, defects and other imperfections. It is used in process control, in post-production quality control and in the testing of systems that are already in use in different industrial fields. The aim is to obtain non destructive quantitative information on magnitude and location of flaws, including depth. When using magnetic probes, the right compromise between a huge magnetic sensitivity and the ability to distinguish between two close magnetic sources has to be attained. As a simple rule, the obtainable spatial resolution is comparable to the distance between the measuring probe and the source of the magnetic or electromagnetic anomaly. Indeed, quite often, the limitation of an NDT method is not imposed by the sensor, but depend on the ability to distinguish between flaw signals and much stronger structural signal signatures.

One of the main aim of the present work is to show the capability and the advantages of the NDT technique based on Superconducting Quantum Interference Device (SQUID) sensors. Indeed, SQUIDs are the most sensitive magnetic sensors because

their properties to measure magnetic field variations are based on quantum mechanics. For this reason, since their discovery in the 1970s, SQUIDs have been used to image the magnetic fields from a wide variety of sources and have been applied in different fields of applications, ranging from the detection of human brainwaves to the observation of the persistent currents associated with quantized flux in superconductors.

The application of SQUIDs as magnetic field detectors allowed the fabrication of magnetic microscopes with the highest magnetic sensitivity ever obtained. These systems are nowadays known as *Scanning SQUID Microscopes* (SSMs). One of the limits of SQUID sensors is the need to work in a cryogenic environment. This condition increases the separation from room-temperature sample under investigation, influencing the final spatial resolution. The best scanning SQUID microscope systems are characterized by a spatial resolution of order of 10 - 50 microns. By minimizing both the distance and the effective sensor area, slight improvements in the spatial sensitivity during SSM operation may be achieved. With the introduction of high-temperature superconductors it has been possible to realize SQUIDs working in liquid nitrogen rather than in liquid helium and this has given a new impulse toward the fabrication of SSMs for the imaging of room-temperature samples.

The thesis work has been carried out at the CNR - Istituto di Cibernetica of Pozzuoli (Napoli), where a semi-commercial room-temperature scanning magnetic microscope prototype has been installed in the framework of the regional project "Centro di Competenza Regionale per la valorizzazione e fruizione dei Beni Culturali e Ambientali" (CRdC-INNOVA).

The microscope consists of a high-temperature dc SQUID magnetometer suspended in vacuum enclosure in contact with a liquid nitrogen refrigerate holder, an XY scanning stage, and a computer control system. The measured magnetic white noise spectral density is about 20 $pT/Hz^{1/2}$ in a magnetic shield, and a maximum spatial resolution of about 70 μm can be obtained, if the stand-off distance is conveniently optimized. The microscope is mounted inside two mu-metal shields, a high permeability material, to screen out the environmental magnetic filed noise.

In the first chapter, we describe general aspects concerning the superconducting SQUID magnetometers. The two macroscopic quantum effects, such as flux quantization in a superconductive ring and Josephson effect, which describe the SQUID-working principles, are introduced. Practical dc SQUID design and readout electronic are widely described for high-temperature dc SQUID.

The second chapter is dedicated to outline the most important features of the main Scanning Probe Magnetic Microscopes focusing the attention on the Scanning SQUID microscope. A characterization of the magnetic field noise and spatial resolution of our SQUID sensor is presented. The efforts we have done to improve our SSM system in terms of spatial resolution and system performance are also described. According to the type of measurement, we distinguish two different techniques we can apply: alternating magnetic field (AC) and direct magnetic field (DC).

In chapter 3, we describe the development and application of NDT based on the SSM. We discuss in detail several measurements of interest to the materials science

and aeronautical industry. In particular, we focused our attention to the application concerned with the analysis of damage in multi-layer joined structures used for wing splice or aircraft skin panel. A special effort has been devoted to analyze and confirm a series of experimental results obtained by a *phase angle rotation method* for depth-selective analysis of subsurface cracks.

AC techniques are based on the measurement of induced eddy currents in conducting objects in the presence of an external applied alternating magnetic field $B_{Excitation}$. The eddy current distribution in a metal (and its associated magnetic field B_{Eddy}) is disturbed when the eddy currents are induced in region containing a flaw or crack. As in other NDT fields, imaging technique are useful to facilitate the interpretation of measurement data obtained by SQUID magnetometry. There are essentially two approaches to the processing of SQUID NDT data: flaw detection and field deconvolution into current patterns. In this work, we emphasize the flaw detection.

The theoretical analysis for the eddy-current problem is important for the quantitative non-destructive evaluation. The analytical solutions for the eddy current distributions have been studied for the unflawed samples excited by the sheet inducer and circular excitation coil. However, for flawed conducting samples, it is difficult to obtain analytical formula for eddy-current distribution, because of complex boundary conditions imposed by the flaw. For this reason, many authors use to numerically investigate the eddy-current distribution in a conducting sample with a flaw, by using a Finite Element Method.

Nevertheless, we developed a novel theoretical approach to eddy current problem in the assumption that the thickness of the sample is negligible with respect to the

penetration depth. This condition is well carried out in low frequency regime and the novel analytical solution is used in this work to compare it with the experimental data.

In the last chapter, we propose two applications of NDT DC technique used in promising research fields. Since this technique is based on the measurement of the residual magnetic field on ferromagnetic samples, it is well-suited as detector of crack initialization and propagation in structural stainless steel objects subjected to fatigue cycles. On the other hand, exploiting the capability to detect magnetic dipole domains with high spatial resolution on the surface of ferromagnetic samples, we propose to apply it to image magnetic particles on magnetic data storage and archeological samples. In order to find a right interpretation of experimental DC data, we have developed a *finite dipole model*, which describes the magnetic measured macro-domains as a combination of single point magnetic dipoles.

Chapter 1

Superconducting Magnetic Sensors

The tunnel of electron pairs between two superconducting electrodes is the mechanism regulating the *Josephson effect*. Since the theoretical prediction of the Josephson effect (B. D. Josephson in 1962), a large effort to develop novel superconducting electronics has been devoted. One advanced superconductive device is certainly the Superconducting QUantum Interference Device (SQUID), which is the most sensitive detector of magnetic field. Any physical quantity that can be converted into a magnetic flux (such as magnetic field, magnetic field gradient, current, etc.) can be measured with this sensor. Since such devices base their working principle on quantum mechanics, they show high magnetic field sensitivity and linear response over a wide frequency range.

In the first section of this chapter, a brief introduction on the basic physical phenomena which govern the operation of SQUID devices, such as flux quantization in a superconductive ring and Josephson effect, are presented. A rapid description of bycristal Grain Boundary Junctions (GBJs) is reported, since the SQUID sensor used in our Scanning SQUID Microscope, has been fabricated with such technique.

In the second section, a description of SQUID working principles and different configurations to improve the device performances (flux transformers, washer SQUID) have been reported, focusing the attention on the adopted design solutions. SQUID readout electronics, used to linearize the sensor response, is widely described.

1.1 General Aspects

A number of applications require the magnetic characterization of sample surfaces with high spatial resolution and high field sensitivity. This can be achieved in different ways, using various magnetic sensors and phenomena. One of these is measuring the magnetic field produced by a sample using SQUID [25].

A dc SQUID is a superconductive loop interrupted by two Josephson junctions (see figure 1.1). The basic phenomena governing the operation of SQUID devices are the *flux quantization* in superconducting loop and the *Josephson effect*. Nowadays SQUID devices fabrication is based on thin film technology and the general trend is, in this field as in many others, toward a more high integration and miniaturization.

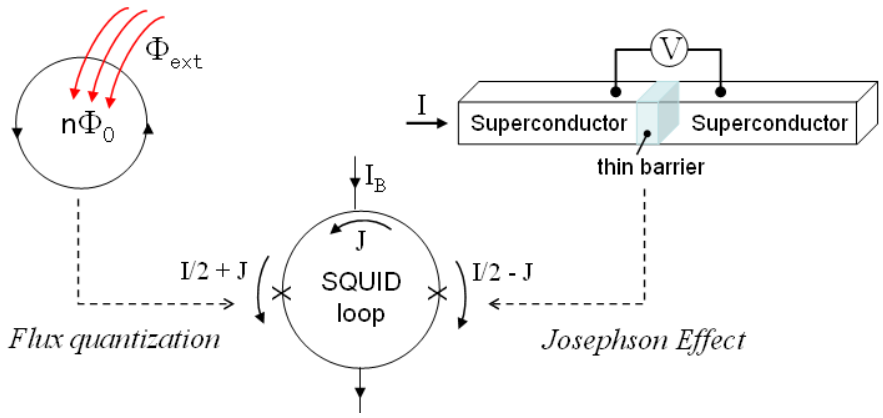

Figure 1.1: *Simplistic view of the phenomena governing a DC SQUID: flux quantization in a superconducting loop and Josephson effect between two weakly separated superconductors. An external magnetic flux* Φ *generates a screening current* J *in the SQUID loop that is periodic in* Φ_0.

A superconductive material enters the resistanceless state when cooled below a certain temperature, the *critical temperature* T_c of that specific material. The discovery

of the high-critical temperature superconductors (HTS), made in 1986 [12], has represented an important step towards the application of superconductivity. Since then, it is possible to work in liquid nitrogen baths instead of liquid helium, with materials which become superconductors at temperatures ten times higher. For instance, Yttrium Barium Copper Oxide (YBCO), one of the most used high-T_c leagues has a T_c of $92K$. Niobium, a typical conventional low-T_c material has $T_c \simeq 9.2K$.

Far from the intention to treat exhaustively the Josephson effect, in the following only some main aspects are reported. The microscopic interpretation of superconductivity was advanced in 1957 by three American physicists, John Bardeen, Leon Cooper, and John Schrieffer, through their microscopic theory of superconductivity, know as the BCS theory [7]. In superconductors, the resistanceless current is carried by pairs of electrons, known as Cooper pairs. Each pair can be treated as a single particle with a mass and charge twice that of a single electron. The Cooper pairs can move through the material effectively without being scattered, and thus carry a supercurrent with no energy loss. In a normal conductor the coherence length of the conduction electron wave is quite short due to scattering. The remarkable property of the superconductors is that all Cooper pairs have the same wave function, $\Psi(\vec{r},t) = |\Psi(\vec{r},t)|e^{i\varphi(\vec{r},t)} = \rho_s^{1/2} e^{i\varphi(\vec{r},t)}$, being ρ_s the density of Cooper pairs and φ the macroscopic phase, forming a macroscopic quantum state with the phase coherence extending throughout the material, as shown schematically in figure 1.2. Cooper pairs, hence, retain phase coherence over long distances, leading to interference and diffraction phenomena. For more important theoretical details, see [8, 20].

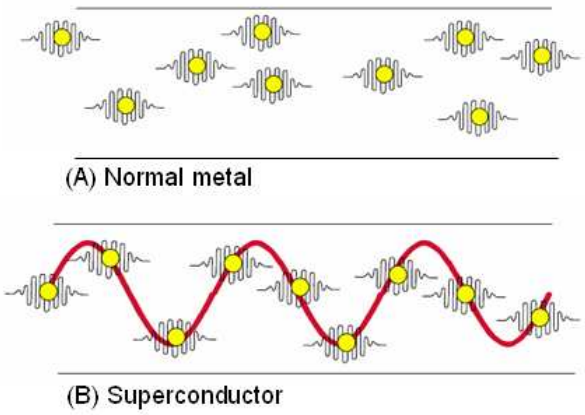

Figure 1.2: *A simplistic view of (A) electron waves in normal metal and (B) a macroscopic quantum state of Cooper pairs in a superconductor.*

1.1.1 Flux quantization

One of the most remarkable phenomenon in superconductors is the quantization of magnetic flux. First predicted by London, this phenomenon was observed experimentally by Deaver and Fairbank [32]. When a superconductor loop undergoes a normal-superconductor phase transition (by lowering its temperature below T_c), in the presence of an external magnetic field, a residual magnetic flux may remain in the loop even after the external magnetic field has been switched off. This flux is produced by the persistent supercurrent generated in the loop and, remarkably, it cannot have arbitrary values but only integer multiple values of the fundamental flux quantum $\Phi_0 = h/2e = 2.07 \times 10^{-15}$ Weber, in other words it is *quantized*:

$$\Phi = n\Phi_0 \tag{1.1.1}$$

where n is an integer.

The quantization of magnetic flux in a superconducting ring is a direct consequence of the fact that the macroscopic wave function Ψ, describing the macroscopic quantum state due to the condensation of Cooper pairs into a single state,

$$\Psi(\vec{r},t) = |\Psi(\vec{r},t)|e^{i\varphi(\vec{r},t)} \tag{1.1.2}$$

must be single-valued. This means that in the absence of applied magnetic fields, the macroscopic superconducting phase $\varphi(\vec{r},t)$ takes the same value for all Cooper pairs throughout the superconductor. However, in the case of loop threaded by a magnetic flux, the phase around the loop changes by $2\pi n$, where n is the number of enclosed flux quanta.

When an external magnetic flux is applied, the condition of quantization is preserved in the loop: an extra amount of supercurrent, a screening current, is generated in the loop to produce a magnetic flux so that the proper value of the total flux corresponding to the quantization condition is restored.

1.1.2 The Josephson junction

When two superconductors are separated by a thin layer, which can be an insulator, a normal conductor or a constriction, the superconductivity is weakened. Such *weak link* is known as Josephson junction (JJ). A typical realization of a weak link is a superconductor-insulator-superconductor (SIS) tunnel junction, consisting of two

superconducting films, separated by a very thin oxide layer, typically 1-2 nm thick. The most commonly used superconductors are Nb and Pb and the critical current density of these junctions may be in the range $10^3 - 10^4$ A/cm^2. Instead of a thin oxide layer other materials may be used, for instance a normal metal, corresponding to a superconductor-normal-superconductor (SNS) junction, in which the metal layer can be thicker.

However, a new class of Josephson junction, specially suited for the high-T_c superconductors, is based on the strong anisotropy of the high-T_c cuprates and involves weak coupling between two superconducting grains with different orientations, the so called *grain boundary junctions* (GBJs) [78, 52]. Due to a well defined grain boundary in a bycristal substrate, the fabrication technology for this junction type is the most reliable and successful currently appropriate for SQUIDs. A *bycristal GBJ* is fabricated by the epitaxial growth of a high-T_c thin film on a bycristal substrate with a predetermined misorientation angle θ (see figure 1.3). This method can be used to obtain arbitrary misorientation angles and geometries, enabling a systematic study of transport properties across high-T_c grain boundaries. The grain boundary is formed along a straight line running across the substrate.

Actually, a wide variety of JJs have been used to fabricate SQUIDs. They fall into three main classes: junction with intrinsic interface (grain boundary), extrinsic interface (extrinsic barriers) and without interfaces (weakened structures). Here, we have described the bycristal GBJs, since the SQUID sensor used in our SSM has been fabricated with such technique. For more details and references on fabrication and

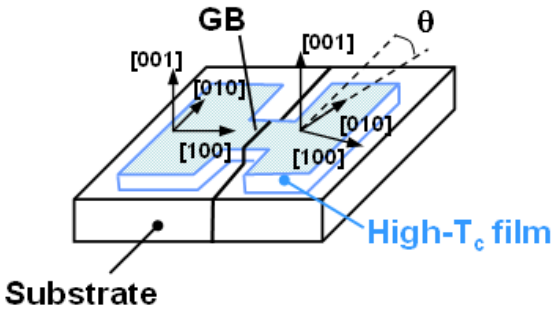

Figure 1.3: *Sketch of the thin-film bicrystal principle using the example of a symmetric [001]-tilt grain boundary with a tilt angle θ.*

properties of HTS JJs see [18].

1.1.3 The Josephson effect

If two superconducting regions are kept totally isolated from each other, the phases of the electron-pairs in the two regions are uncorrelated. However, if the two regions are brought together so that electron-pairs may tunnel across the barrier, the two electron-pair wave functions will become coupled. This means, in practice, that a supercurrent can flow in spite of the presence of the tunnel barrier as predicted by B. D. Josephson and this phenomenon is known as *Josephson tunneling* [61].

Thus, a Josephson junction is a superconductor interrupted by a thin insulating layer, where superconductive properties are weakened, as shown in figure 1.4. In the Josephson formulation, the phase difference between two superconductors is a well defined physical quantity and it obeys to the relation (*dc Josephson effect*)

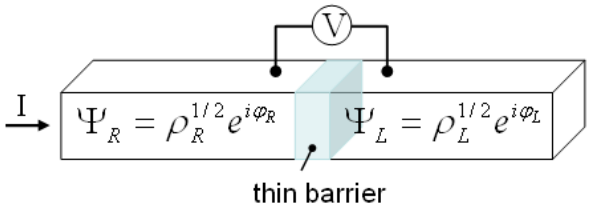

Figure 1.4: *A Josephson junction may be represented by a superconductor interrupted by a thin insulating layer. The applied current I controls the difference $\delta = \varphi_R - \varphi_L$ between the phases of the complex order parameters of the two superconductors according to the dc Josephson's relation (eq. 1.1.3).*

$$I_s = I_c \sin(\varphi_1 - \varphi_2) \tag{1.1.3}$$

Equation 1.1.3 describes the relationship between the supercurrent I_s passing across the junction, the difference between the phases φ_1 and φ_2 of the condensate states in the two superconducting electrodes, and the critical current, I_c, i.e. the maximum current which the junction can support without developing any voltage across it.

Furthermore, if a constant voltage V is maintained across the junction, the following relation (*ac Josephson effect*) predicts that

$$V = \frac{\hbar}{2e}\frac{d}{dt}(\varphi_1 - \varphi_2) \tag{1.1.4}$$

the phase difference $\delta = \varphi_1 - \varphi_2$ evolves linearly with time, i.e. $\varphi = \varphi_0 + 2e/\hbar V t$, the Josephson current alternates with a frequency $\nu = 2eV/h = 483.6 MHz/\mu V$ (ac Josephson effect), and the junction behaves as a frequency-voltage transducer.

As the current across the junction is increased from zero, for $I < I_c$ the phase difference has the value $\delta = \arcsin I/I_c$ constant in time, so that the voltage across the junction remains zero (V = 0). When the current exceeds the critical current $I > I_c$, the phase difference evolves according equation 1.1.4 and there is a voltage across the junction ($V \neq 0$).

The relation between the current and the voltage for a Josephson junction is represented by the I-V characteristic reported in figure 1.5 (A). The I-V curve shows that if the junction is biased with a constant current source, lower than the critical current I_c, there will be no voltage drop across the junction, although the passage of the current through the device will introduce a phase difference across it. When the bias current exceeds I_c, a voltage will appear and the phase difference become time-dependent.

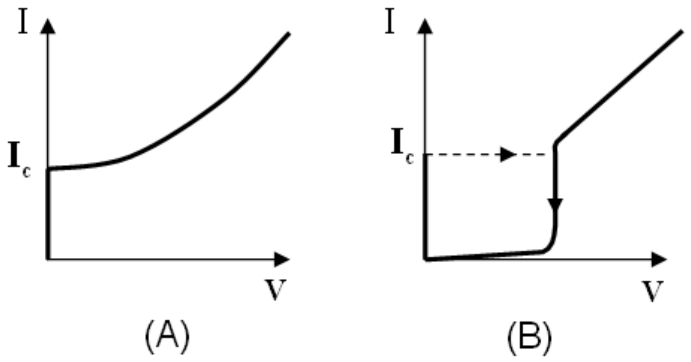

Figure 1.5: *I-V characteristic: (A) non-hysteretic junction and (B) hysteretic junction.*

Just one year later the discovery of Josephson tunneling, Anderson and Rowell [4]

made the first observation of the dc Josephson effect, using a thin-film, Sn-SnO_x-Pb junction cooled in liquid helium. They showed that the current voltage characteristic of a Josephson junction, owing to the capacitance associated with the structure, was strongly hysteretic (see figure 1.5 (B)). This hysteresis can be eliminated by shunting the Josephson junction by a normal ohmic resistor R. For dc SQUID realization, one uses exclusively resistively shunted non hysteretic junctions with a single valued current voltage characteristic.

Subsequently, Rowell [105] showed that a magnetic field B, applied in the plane of the thin films, caused a modulation of the critical current according to the relation

$$I_c(\Phi) = I_0(0)|\frac{\sin(\pi\Phi/\Phi_0)}{(\pi\Phi/\Phi_0)}| \tag{1.1.5}$$

Thus, the critical current becomes zero for Φ equal to integer units of the flux quantum $\Phi_0 \approx 2.07 \times 10^{-15}$ Wb.

The observation of this Fraunhofer-like result, which is analogous to the diffraction of monocromatic coherent light passing through a slit, is a validation of the sinusoidal current phase relation.

Later, Jaklevic et al. [57] demonstrated quantum interference between two thin-film Josephson junctions connected in parallel on a superconducting loop. The dependence of the critical current on the applied magnetic field is shown in figure 1.6. The rapid oscillations are due to the quantum interference between the two junctions, whereas the slowly varying modulation arises from the diffraction-like effect of

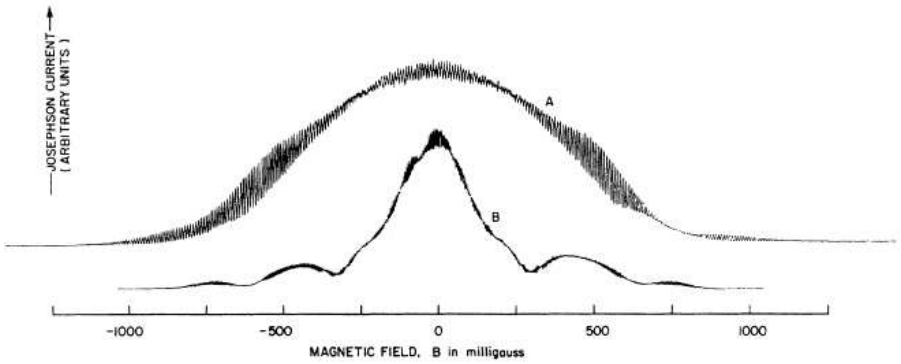

Figure 1.6: *Josephson current vs. magnetic field for two junctions in parallel showing interference effects. (as reported in ref. [57]).*

the two junctions. The period of oscillations is given by the field required to generate one flux quantum in the loop: thus, the maxima critical current occur at $\Phi/\Phi_0 = 0, \pm 1, \pm 2, ... \pm n$. The observations of these oscillations set the stage for the dc SQUID. A useful reconstruction of the sequence of events and the motivations about the discovery and the invention of the SQUID can be found in [110].

1.2 Superconducting Quantum Interference Devices (SQUIDs)

Steaming the more mature technology, the first kind of dc SQUID was obviously a low-T_c SQUID. First, the development of the planar dc SQUID with an integrated multiturn input coil [66] and second, the invention of high reproducible $Nb{-}AlO_x{-}Nb$ tunnel junction, ensured the robustness of most of the wafer devices.

However, the advent of high-T_c superconductivity in 1986 [12] resulted in the development of new types of SQUIDs based on high-T_c thin-film technology [26, 28]. Indeed, the first routinely fabricated thin-film dc SQUIDs were made from YBCO with grain boundary junctions, formed between randomly oriented grains in the film [77]. To date, the majority of high-T_c SQUIDs are made with more controlled by-cristal GBJs: a YBCO film is deposited on a bicrystal substrate of $SrTiO_3$ or MgO in which there is an in-plane misorientation of 24^o or 30^o. The films growth epitaxially on the substrate, is subsequently patterned into two bridges few micrometers wide. A configuration for bicrystal HTS dc SQUIDs is shown schematically in figure 1.7.

Adopting high-T_c SQUID technology, a major issue that was recognized early was the prevalence of $1/f$ noise at low frequencies, that is, noise with power spectral density scaling inversely with the frequency f. In fact, we may distinguish two independent sources of such noise: one is correlated to critical current fluctuations and the other one is produced by the uncorrelated hopping of flux vortices among pinning sites in the films. Both noise mechanisms yields a $1/f$ power spectrum.

The level of flux noise was greatly reduced by the progressive improvement of film quality, which lowered the density of pinning sites. The use of slots or holes in the film

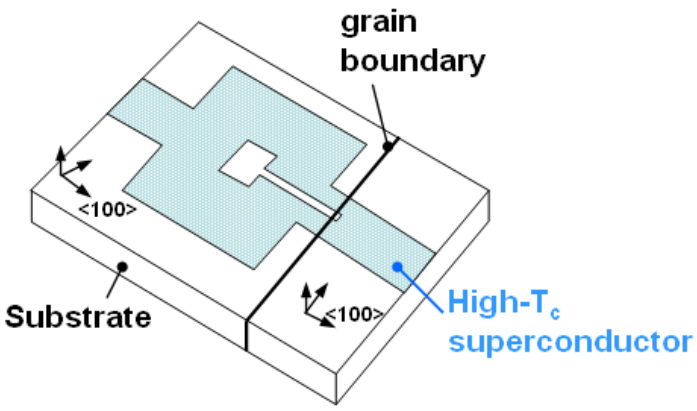

Figure 1.7: *Schematic presentation of a "square washer" dc SQUID based on bicrystal Josephson junctions.*

effectively reduced the generation of $1/f$ noise in devices cooled in weak fields [31]. On the other hand, for dc SQUIDs a modulation technique employing bias-current reversal has proved to be very effective in averaging out this noise signal [80].

1.2.1 The dc SQUID

The dc SQUID is a magnetic flux-to-voltage transformer. It consists of two Josephson junctions connected in parallel on a superconducting loop, as shown in figure 1.8. When a symmetric dc SQUID is biased with an external dc current I_B, a current $I/2$ flows through each of the two junctions; the critical current of the SQUID, or the maximum current it can sustain without developing a voltage drop across it, in the absence of any external magnetic fields, is thus $2I_c$. When a magnetic flux is applied perpendicular to the plane of the loop, the loop responds with a screening current J

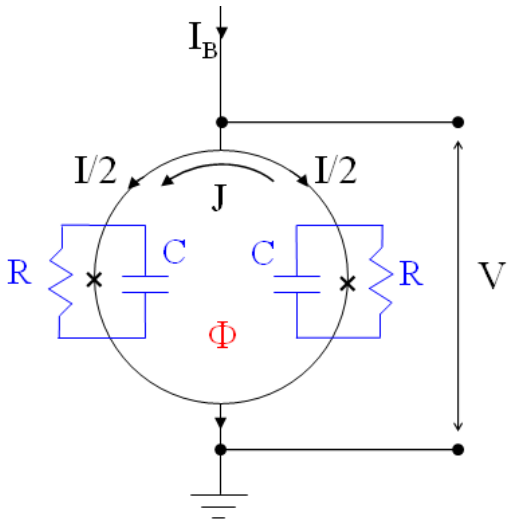

Figure 1.8: *Schematic representation of a dc SQUID. Two Josephson junctions (represented by the two crosses) interrupt a superconductive loop. A bias current can be feeded in both junctions through the parallel connection. A dc SQUID is operated by biasing the device at a constant current I_B, a variation of the voltage V is achieved when the externally applied magnetic flux Φ changes. There are also shown the two shunt resistances R and the capacitance C of each junction.*

to satisfy the requirement of flux quantization

$$\Phi = \Phi_{ext} + LJ = n\Phi_0 \tag{1.2.1}$$

where L is the inductance of the loop and the total flux of equation 1.1.1 has been explicitly expressed as an external contribution plus a screening contribution. Each junction is resistively shunted to eliminate any hysteresis on the current-voltage characteristic so that the latter appears as sketched in figure 1.9 (A).

The screening current J is zero when the applied external magnetic flux is an

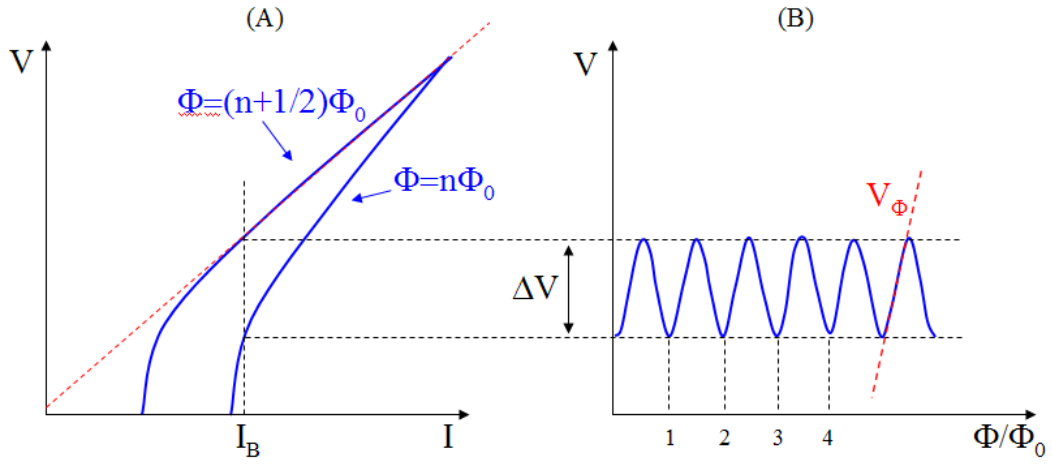

Figure 1.9: *(A) Schematic representation of a dc SQUID IV characteristic. Varying externally the applied magnetic flux, the IV curve will oscillate periodically between two states: the integer* $\Phi = n\Phi_0$ *and half integer flux* $\Phi = (n + 1/2)\Phi_0$. *The two limiting branches differ essentially for the maximum critical current. (B) dc SQUID voltage modulation measured at constant bias current as a function of the applied magnetic flux.*

integer number of Φ_0 and has a maximum value equal to $\pm(\Phi_0/2L)$, as derived by equation (1.2.1), when the external flux is exactly between two integer values of Φ_0, i.e. when it is $(n + 1/2)\Phi_0$. Thus, J exhibits a periodic variation with the externally applied magnetic flux. As the flux is increased above the value $(n+1/2)\Phi_0$, a transition from the state n to $n+1$ takes place, corresponding to the entrance of a flux quantum in the loop and J abruptly changes the sign, as shown schematically in figure 1.10 (A).

The effect of the screening current J flowing around the SQUID loop is the reduction of the critical current of the SQUID from $2I_c$ to $(2I_c - 2J)$. In fact, this circulating current adds and subtracts respectively itself to the bias current flowing in the two branches of the loop containing the junctions, so that the critical current

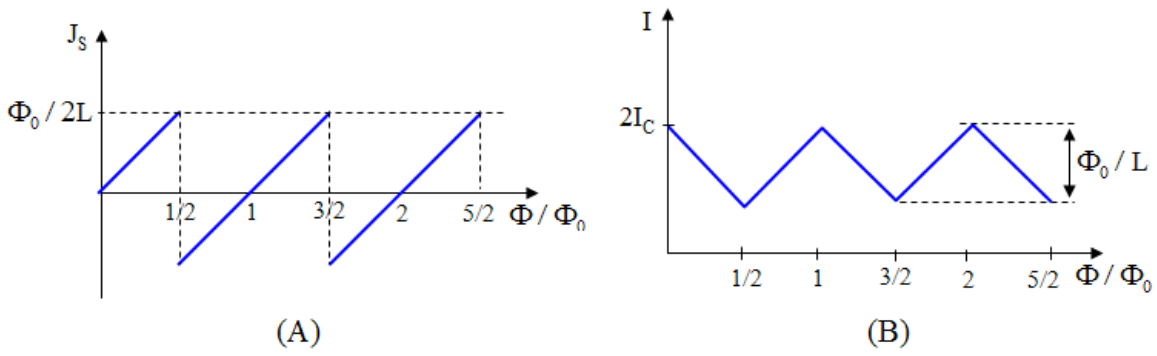

Figure 1.10: *Variation of (A) the screening current J_s and (B) the maximum critical current as a function of the applied flux.*

of the junction is reached when $I/2 + J = I_c$.

Thus the SQUID switches to the voltage state when $I > I_c - 2J$. Since J is a periodic function of the externally applied flux, the critical current of the SQUID is also a periodic function of the externally applied flux, as shown in figure 1.10 (B).

As a consequence of these considerations, if the SQUID is biased with a current slightly larger than $2I_c$, the output voltage of the SQUID turns out to be a periodic function of the magnetic flux applied perpendicular to the plane of the SQUID loop, as shown in figure 1.9 (B). The SQUID device thus works as a transducer of magnetic flux producing measurable voltage, which changes its output for small changes of the applied magnetic flux.

An important parameter characterizing the efficiency of this operation is the *flux-to-voltage transfer coefficient* V_Φ. In fact, the maximum response to a small flux change $\delta\Phi \ll \Phi_0$ is obtained by choosing the bias current so that it maximizes the amplitude of the voltage modulation and sets the external flux at $\Phi_a \approx (2n+1)\Phi_0/4$,

where the transfer coefficient $V_\Phi = |(\partial V/\partial \Phi_a)_I|$ is a maximum. The resulting voltage change $\partial V = V_\Phi \partial \Phi_a$ is approximatively linear in this regime.

The maximum value V_Φ can be obtained observing that, as the flux varies by $\Phi_0/2$, the critical current variation is Φ_0/L, and the corresponding voltage variation is $\Delta V = (\Phi_0/L)R/2$, where $R/2$ is the parallel resistance of the two shunts. This gives the value $V_{\Phi max} \approx \Delta V/(\Phi_0/2) \approx R/L$.

A very important issue in connection with the SQUID operation is the voltage noise which affects the SQUID performances. Of course, one would keep noise as low as possible. The major source of noise is related to the presence of shunt resistance in the junctions constituting the SQUID. Resistors are universally affected by voltage noise because of the thermal fluctuation of the electron density, the so called Nyquist noise.

The Nyquist noise in the shunt resistors introduces a white voltage noise across the SQUID with a spectral density $S_V(f)$, which turns into the *flux noise spectral density*

$$S_\Phi(f) = S_V(f)/V_\Phi^2 \tag{1.2.2}$$

Since the latter parameter takes in count the dimension of the SQUID loop, it is often useful to characterize SQUIDs in terms of their *energy noise*

$$\varepsilon(f) = S_\Phi(f)/2L \tag{1.2.3}$$

Equation 1.2.3 is independent of the SQUID loop inductance L and the energy noise

becomes a good parameter to compare different SQUIDs and other magnetic sensors, as it will be shown in chapter 2.

1.2.2 SQUID readout

Since the response of the SQUID is a periodic transfer function (see figure 1.9 (B)), in order to linearize it, John Clarke et al. [27] came out with the idea of operating the SQUID in a flux-locked loop (FLL).

Figure 1.11 shows a schematic of a dc SQUID operated by a FLL. An oscillator applies a modulation flux at frequency f_m (100 kHz signal) to the SQUID through a feedback coil. The voltage signal of the SQUID, V_s, goes through a preamplifier, is synchronously detected and then sent through an integrating circuit. The output of the integrator is connected to the feedback coil through a resistor R_f.

When the flux in the SQUID is $n\Phi_0$, the V-Φ curve is symmetric about this local minimum and the resulting voltage is a rectified sine wave, as shown in figure 1.12 (a), with a frequency double of f_m. Thus the output of the lock-in detector is zero. On the other hand, if the flux is shifted away slightly from the local minimum, the voltage across the SQUID contains a component at frequency f_m and there will be an output from the lock-in detector. When flux is $(n + 1/4)\Phi_0$ (figure 1.12 (b)), the voltage across the SQUID contains only the component at frequency f_m and hence the output from the lock-in detector is a maximum. Thus, as one increases the flux from $n\Phi_0$ to $(n + 1/4)\Phi_0$, to output from the lock-in is steadily increases; if instead we decrease the flux from $n\Phi_0$ to $(n - 1/4)\Phi_0$, the output from the lock-in is negative (figure 1.12 (c)). After integration, this signal is fed back as a current through a

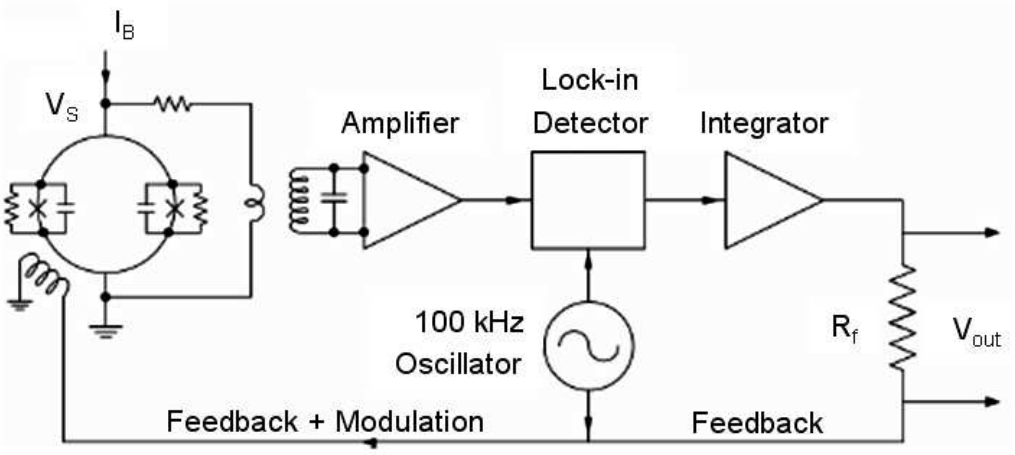

Figure 1.11: *Flux modulation and feedback circuit for the dc SQUID. The voltage response of the SQUID V_s is the input of the FLL, which uses a modulation flux scheme to maintain the SQUID in a point in which the slope of the $V - \Phi$ curve is a maximum. The user measures a change in V_{out}, which is proportional to the amount of flux variation detected by the SQUID.*

feedback resistor R_f to a feedback coil inductively coupled to the SQUID; usually the same coil is used for both flux modulation and feedback.

In this way, for a flux change $\delta\Phi$ detected by the SQUID, the feedback circuit will produce an opposing flux $-\delta\Phi$ and a voltage proportional to $\delta\Phi$ can be measured across the resistor R_f. In other words, the FLL is a negative feedback circuit that creates a null-detector of magnetic flux. More details about a variety of schemes can be found in [1, 5].

It is well known that, fluctuations in the critical current and resistance of the junctions are a major source of $1/f$ noise in dc SQUIDs. At the operating point, the critical-current noise dominates the resistance noise and contributes $1/f$ noise in two

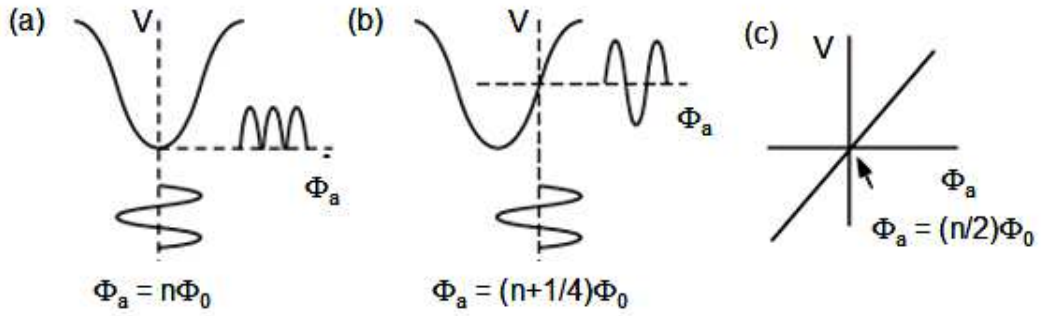

Figure 1.12: *Flux modulation scheme (as reported in [25]) showing voltage across the dc SQUID for (a)* $\Phi_a = n\Phi_0$ *and (b)* $\Phi_a = (n + 1/4)\Phi_0$ *, (c) the output* V_L *from the lock-in detector versus* Φ_a *is shown.*

ways. Fluctuations in the critical current, that are *in-phase* at the two junctions, induce a voltage noise across the SQUID, that is eliminated by flux modulation at frequency f_m. Fluctuations, that are *out-of-phase* at the two junctions, are equivalent to a flux noise that is not reduced by this scheme. Fortunately, this noise component can be eliminated by means of several methods in which the bias current is periodically reversed [75, 37, 42]. These latter schemes are rarely implemented for low-T_c SQUIDs where the cut-off frequency of the out of phase component of the critical current $1/f$ noise is extremely low, but it is essential for high-T_c SQUIDs [33, 76] where it is relatively high.

1.2.3 SQUID magnetometers

The previous description of a quantum interferometer is rather oversimplified. More detailed analysis of a SQUID include the explicit dynamics of the two phases in the presence of noise, asymmetries, etc. [115] so that the output voltage can be correctly

predicted as a function of the flux.

Moreover, to operate these structures efficiently as magnetic sensors requires the introduction of a number of practical solutions which in the course of the years have been recognized and reflect nowadays practical SQUID designs. Indeed, one of the main issue is the area of the superconducting loop containing the junctions. To ensure the largest possible flux change, being $\Delta\Phi = A_s \Delta B$, it appears advantageous to make the loop area A_s as large as possible. On the other hand, we know that the modulation depth of the maximum supercurrent decreases with increasing ring inductance oscillating between $2I_c$ and $2I_c - \Phi_0/L$. On the other hand, the inductance of the loop is required to be as small as possible. Consequently, although the magnetic flux noise $S_\Phi(f)$ may be very low, the magnetic field noise $S_B(f) = S_\Phi(f)/A_s^2$ is often too high for many applications. For this reason, most of applications require that an additional superconductive loop structure is coupled to the SQUID to enhance its magnetic field sensitivity.

Flux transformer

In order to avoid this problem and increase the effective area of the SQUID magnetometer, flux transformers are used [79]. A flux transformer is a closed superconducting loop in which the total magnetic flux is a constant. It is generally made by two sections, as shown schematically in figure 1.13, a receiving end (*pick up coil*), which can have several arrangements such as magnetometer, gradiometer etc. and a coupling end (*input coil*), which can be coupled directly or inductively to the SQUID, depending on technological and design requirements. If the external field through the pick up coil changes, a shielding current is generated in the whole loop to compensate

the magnetic flux associated with the field change. The final effect is the generation of a magnetic field in response to the magnetic field variation detected at the pick up location.

Figure 1.13 (a) shows the configuration of a *magnetometer*, with a pick up loop of inductance L_p connected to an input coil of inductance L_i that is coupled to the SQUID via a mutual inductance $M_i = k_i(LL_i)^{1/2}$, where k_i is a coupling coefficient.

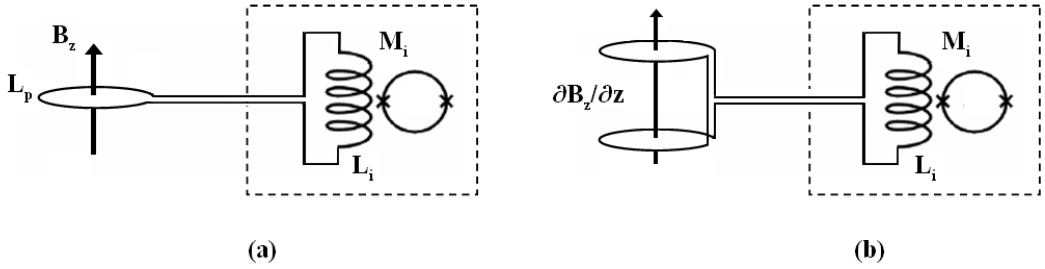

Figure 1.13: *Superconducting flux transformers: (a) magnetometers and (b) first-derivative axial gradiometer. The dashed box indicates a superconducting shield enclosing the SQUID.*

The magnetic-field noise is

$$S_B(f) = S_\Phi(f)/A_{eff}^2 \tag{1.2.4}$$

where A_{eff} is the effective area of the magnetometer. Clearly, one wants to make A_{eff} as large as possible without increasing $S_\Phi(f)$.

Washer SQUID

A way to increase the effective area of the SQUID without increasing its inductance can be fulfilled owing to the thin-film technology and to the diamagnetic (the ability to deviate magnetic field lines) properties of superconductors. Indeed, in the place of a thin loop, one uses flat large area superconductors known as washer SQUID (see figure 1.14) or Ketchen SQUID [66] from the name of the researcher who first introduced this solution.

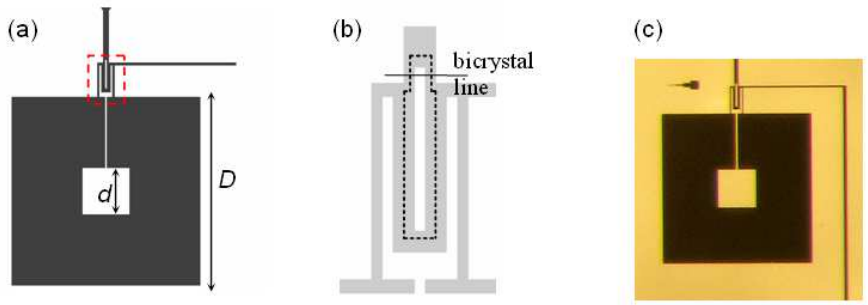

Figure 1.14: *A washer SQUID. (a) Directly coupled magnetometer: the DC SQUID is connected to the pick up loop. (b) a particular of the coupling between the SQUID and the input coil. Dashed line indicates grain boundaries. (c) A picture of such device made by HTS group of CNR - Istituto di Cibernetica "E. Caianiello" of Pozzuoli, Naples - Italy [101].*

When a magnetic field is applied normally to the film plane, shielding currents flow in the superconducting film. The screening currents, circulating around the inner gap ($\sim$ 10 μm for SQUID operated at $77K$), essentially determine the superconducting loop size of the SQUID and hence its inductance. The outer shielding currents contribute to focus the field in the inner opening, increasing the collected flux. In this condition, the *effective area* A_{eff} of the SQUID, may be reasonably approximated by

Dd, where d and D are the inner and outer dimensions of the washer, respectively. It is worth noting that the outer diameter cannot be too large otherwise during the cooling process, vortices start to be trapped into the structure hampering the normal operation of the device.

The inductance of the flux transformer is the sum of the pick up coil contribution L_p and the input coil (inserted upon the SQUID) contribution L_i. A flux change $\delta\Phi^{(p)}$ in the pick up loop induces a current J_s in the flux transformer determined by the zero flux condition in the flux transformer loop which gives $\delta\Phi^{(p)} + (L_p + L_i)J_s = 0$, i.e. $J_s = -B_p A_p/(L_p + L_i)$, where B_p is the magnetic field and A_p the area of the pick up coil, respectively. This current, through the input coil, generates in the SQUID the flux $\delta\Phi^{(s)} = M_i|J_s|$. Since the magnetic field of the SQUID $B_s = \Phi^{(s)}/A_{eff}$, it can be written as

$$B_s = -B_p \frac{A_p}{A_{eff}} \frac{\sqrt{L_s L_i}}{L_p + L_i} \tag{1.2.5}$$

B_s is maximum when $dB_s/dL_i = 0$, i.e. when $L_p = L_i$, so that B_s acquires the following value for the maximum

$$B_{smax} = -B_p \frac{A_p}{A_{eff}} \sqrt{\frac{L_s}{4L_p}} \tag{1.2.6}$$

Since the inductance L_p is proportional to $A_p^{1/2}$, from equation 1.2.6, we see that B_s is proportional to $A_p^{3/4}$. In conclusion, we see that the sensitivity of the magnetometer can be increased by choosing a large value of the pick up coil A_p.

Moreover, the input coil is required to have an inductance matching with the pick-up loop ($L_p = L_i$), while remaining tightly coupled to the SQUID loop. As the size of the pick-up loop is larger than the SQUID loop, to realize this matching the input coil is laid over the SQUID washer as a multiturn thin-film spiral, separated from the superconducting washer by an insulating layer.

This geometry has been adopted practically universally ever since its introduction although some workers have based their design on other geometries such as the multiloop SQUID. This consists of several relatively large pick up loops all connected in parallel across the same junctions to reduce the SQUID inductance. A comprehensive theory for thin-film multiloop SQUIDs and their performance at 77 K has been given by [38].

Chapter 2

Room-Temperature Scanning SQUID Microscope

Scanning SQUID microscope (SSM) is a Scanning Probe Microscope (SPM), where a SQUID sensor is used to map the magnetic flux at a certain height above the surface of the sample. The measurement after a scan operation yields a two-dimensional image of the measured magnetic flux value, as a function of the relative sensor-to-sample position. A SSM has the advantage to incorporate the most sensitive magnetic flux detector (SQUID), although it has a modest spatial resolution compared with the other common scanning magnetic microscope (MFM, SHPM, etc.). However, it remains the most powerful technique for measuring the surface and sub-surface magnetic field distribution.

This chapter is dedicated to the description of the room-temperature sample Scanning SQUID Microscope located at *Istituto di Cibernetica* of CNR of Pozzuoli, Naples (Italy). In particular, a description of the system in terms of sensor characteristics and system optimization is carried out. The most commonly used Scanning Probe Magnetic Microscopes have been introduced in the first section. A brief overview of

the different approaches to Scanning SQUID Microscope design is reported in terms of sample-temperature and SQUID sensors employed.

The second section is focalized on the description of the our Scanning SQUID Microscope and the strategies adopted to reduce the noise level system. Essentially two main operational modes, alternating field (AC) or direct field (DC), are described. *Injection currents* or *alternating currents* can be apply based on the sample characteristics. A brief description of the lock-in technique used for the AC measurements is also reported.

In the last section, the liquid nitrogen-cooled SQUID sensor used in our system is described in terms of its configuration and magnetic noise performance. Spatial resolution and field sensitivity have been calculated and some useful considerations about our system performance have been reported.

2.1 Scanning Probe Magnetic Microscopy

Here we want to focus the attention on the many techniques for imaging local magnetic field or flux above a sample surface which are in use nowadays. Scanning SQUID microscopy is one of the most powerful and promising techniques to measure and image magnetic field distributions. This is mainly due to the SQUID unsurpassed sensitivity, its linear and ability to operate without perturbing the sample, as well as the versatility of the technique itself to measure a great variety of samples.

In addition to SSM, which is the subject of this thesis, widely used techniques include decoration technique and magnetic-optical imaging, which are known for their relative simplicity, and Scanning Electron Microscopy with Polarization Analysis (SEMPA) [107], which can achieve high spatial resolution.

Moreover Magnetic Force Microscopy (MFM) [102, 54] can be used to combine topographic and magnetic information. It measures the gradient of the magnetic field and allows the imaging of very small magnetic structures of order of tens of nm. In addition, the localized magnetic field from the MFM tip will change the micromagnetic state of the sample which can complicate interpretations of the measurements. On the other hand, its magnetic sensitivity is orders of magnitude lower than that of SQUIDs.

Finally, Scanning Hall Probe Microscopy (SHPM) [96, 106] is a technique which allows a good spatial resolution but shows a flux sensitivity lower than SQUIDs and the sensor does not need to operate at low temperature. However, SQUIDs rapidly become more sensitive than Hall bars with increasing pickup loop area. An interesting

review on such magnetic techniques can be found in [30].

A comparison between the spatial resolution and the magnetic field sensitivity of different types of systems is shown in figure 2.1.

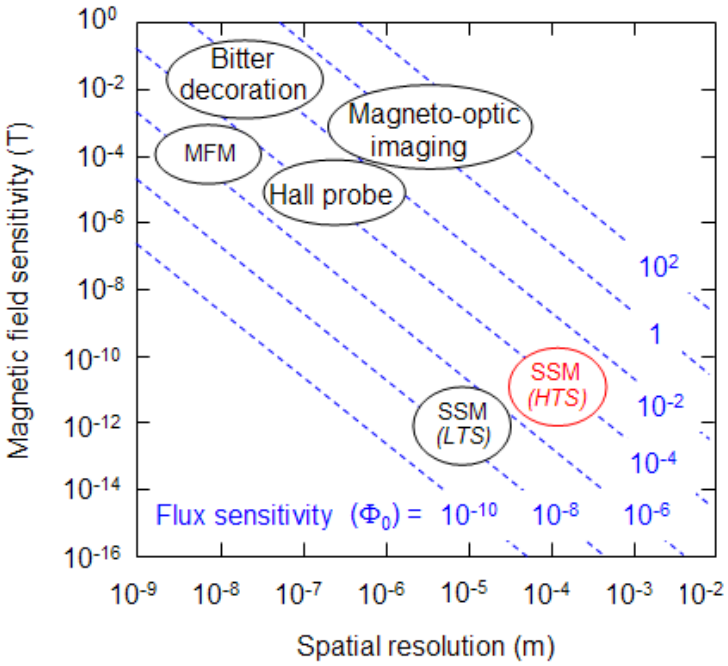

Figure 2.1: *Comparison of the spatial resolution and magnetic sensitivities of different magnetic microscopy techniques.*

.

However, each technique has its own advantages and disadvantages and the decision to use one versus the other one depends on several factors such as: sensitivity, spatial resolution, frequency response, source-to-sensor distance, detection of fields versus gradients, need to operate in an externally applied field, ability to reject external noise, ability to make measurements without perturbing the sample, and the required operating temperatures of both the sample and the sensor.

2.1.1 Scanning SQUID Microscopy

Scanning SQUID systems can be used for the detection of weak magnetic fields generated, for instance, by electronic circuits or biological samples. Compared to other magnetic evaluation methods for microscopic objects, the SMM has a higher magnetic field sensitivity and high linearity over a wide dynamic range. The disadvantages of this instrument are modest spatial resolution and the requirement for a cooled sensor. Further improvement of the spatial resolution is possible using a better combination of a smaller-sized SQUID pick-up loop and reduced distance to the object. By minimizing SQUID-to-sample separation for higher field and spatial resolution represents a problem for room temperature objects, which are placed outside the cryostat.

Here we describe a SMM for room temperature objects with a liquid nitrogen-cooled SQUID sensor. Its capability to operate in magnetic fields up to about 5 G allows to perform 2D mapping of the local dc and ac susceptibility of the objects.

2.1.2 Volumetric energy resolution

SQUID magnetometers show a optimal combination of field sensitivity and spatial resolution compared with the other magnetic sensors. There are different parameters used to compare magnetic sensors as reported in [39, 35], but the energy resolution with respect to the sensor volume is proposed as a convenient way to compare high sensitivity magnetic sensor, as reported in [103]. Such *volumetric energy resolution* parameter is now defined as

$$\varepsilon(f) \approx \frac{S_\Phi(f)}{2L} \approx \frac{S_B(f)}{2L}\Omega \tag{2.1.1}$$

where $S_\Phi(f)$ and $S_B(f)$ are the flux noise and magnetic field noise spectral density, respectively, L is the pick-up coil SQUID inductance, and Ω is the sensor volume.

A comparison between SQUID and the recent advances in room temperature solid state sensors, which include magnetoresistive devices (AMR, GMR, spin valve, and spin dependent tunnelling device), giant magneto-inductive devices, atomic vapor laser magnetometers, is shown in table 2.1.

Device	**Energy Resolution (J/Hz)**
SQUID w/pickup	1×10^{-30}
SERF	3×10^{-29}
Hybrid GMR/SC	4×10^{-29}
GMI	6×10^{-28}
AMR	7×10^{-26}
CSAM	2×10^{-25}
He4	4×10^{-24}
Fluxgate	3×10^{-23}
GMR w/feedback	4×10^{-23}
Hall	5×10^{-23}
Magnetoelectric	5×10^{-23}
TMR w/FC	1×10^{-19}

Table 2.1: Comparison between different magnetic sensors by means of their energy resolution-to-volume [103].

It is possible to show that the sensor with the better spatial and magnetic resolution is the one with the minimum value of $\varepsilon(f)$. In the specific case, SQUID sensor, with an energetic resolution of order of 10^{-30} J/Hz, is the device showing the best compromise between these two parameters, as it is presented in table 2.1.

2.1.3 Low-T_c and high-T_c SSM

In a scanning SQUID microscope the sample is scanned by a SQUID, which measures the magnetic field above the sample surface. At present there are several different approaches to design a scanning SQUID microscope, according to the sample temperature (cold or room-temperature (RT)) and also the type of SQUID sensor (low or high-T_c) used. These are well summarized by Kirtley and Wikswo in [69] and shown in figure 2.2.

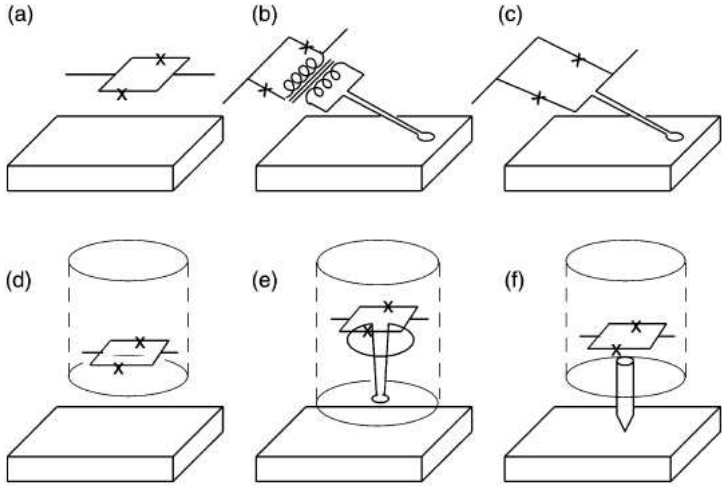

Figure 2.2: *Various strategies have been used for scanning the sample relative to the SQUID, as reported in [69]. Both sample and sensor can be cooled (a-c) or only the SQUID (d-f). The field at the SQUID can be detected (a, d), or a superconducting pickup loop can be inductively coupled to the SQUID (b, e), or the pickup loop can be integrated into the SQUID design (c). In (f), a ferromagnetic tip is used to couple flux from a room temperature sample to a cooled SQUID.*

.

Historically, low-T_c cold-sample SQUID microscope was the first to be developed

immediately after the invention of the SQUID magnetometer [122, 57]. The first two-dimensional scanning SQUID microscope was invented by Rogers and Bermon [104]. They observed flux trapped in a superconducting niobium thin film. More recently, low-T_c SQUID microscopy for cold samples has been extensively used to study a great variety of superconducting phenomena: vortex trapped in a planar superconducting film [72], Meissner imaging [73], phase-sensitive symmetry tests [74, 44], diamagnetic shielding above T_c [56].

Black et al. introduced high-T_c SQUID microscopy to study cold samples with a variety of techniques, including static magnetization [13], eddy currents [14], radio frequency [15] and microwave imaging [16]. On the other hand, high-T_c SQUID microscopy for RT samples has been extensively developed by two groups: Wellstood group at University of Maryland [119, 21, 22] and John Clarke group at University of California, Berkeley [89, 88, 45].

For some applications, the higher operating temperatures of high-T_c SQUID microscopes provide an important advantage in comparison with low-T_c SQUID systems. Indeed, the cryogenic as well as the shielding requirements are much less restrictive. However, higher operating temperatures impose higher intrinsic noise levels. High-T_c SQUIDs also suffer from excess of $1/f$ noise at low frequencies. Therefore, high-Tc SQUIDs have not yet achieved the key combination of low-noise performance, low-frequency sensitivity and high spatial resolution, as request for some kind of applications. Efforts to improve its spatial resolution by meas of a ferromagnetic flux focusing tip [112, 99, 51] have been made over the last few years.

However, SSM for RT-samples has found an important area of development in the field of non-destructive evaluation (NDE) [36, 63, 62, 64]. The sensitivity at low frequencies allows them to work as eddy-current sensor with high depth resolution to detect flaw on paramagnetic materials. In addition, SQUID wide dynamic range make them suitable to image defects in ferromagnetic structures.

2.2 Scanning SQUID Microscope System Design

The microscope consists of a high-T_c dc SQUID sensor, placed in vacuum with a self-adjusting standoff, close spaced liquid nitrogen dewar, XY scanning stage and a computer control system. The microscope is mounted on actively damped platform, which reduces the vibrations from the environment as well as the internal stepper motor noises. Two μ-metal shields enclose the overall system to eliminate environmental electromagnetic field noise, which could degrade the system performance. A picture of the SMM out of the μ-metal shields is shown in figure 2.3.
Moreover, to reduce low-frequency noise signals, including 50 Hz line noise, low-pass hardware and software filters are used. A laser profilometer, high-resolution camera and a 1 μm precision z-axis positioning system allow to achieve a close positioning of the sample under the sensor.

Intrinsic noise system

Since our SSM is a semi-commercial prototype system, it has required a series of tricks to reduce its intrinsic noise level. When the sample is scanned under the SQUID sensor and the computer records the SQUID response as a function of the XY position, the movement of the stepper motors increases the environmental noise detected by the sensor by about 10 times at 100 Hz, as shown in figure 2.4 by a measurements of spectral density noise.

The moving mechanism is constituted by high precision stepper motors with a minimum step size of 12.5 μm and it is located inside the two μ-metal shields. For this

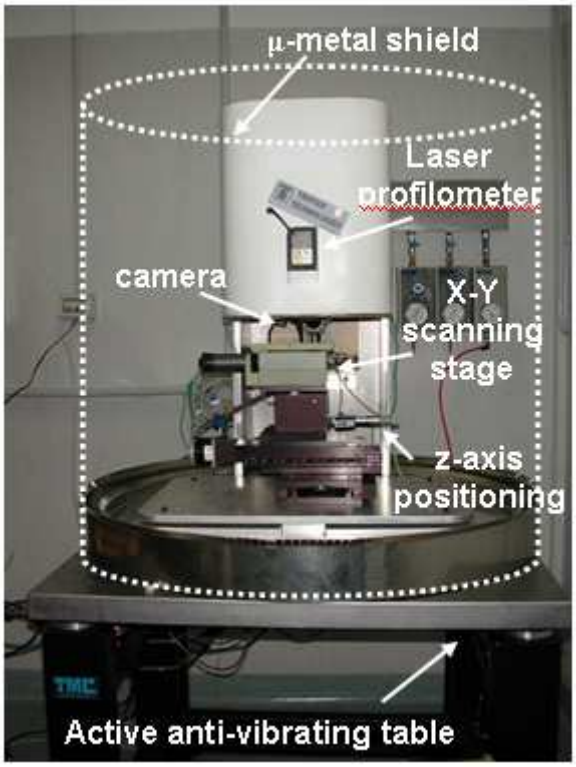

Figure 2.3: *A photograph of the Scanning SQUID Microscope located at CNR - Istituto di Cibernetica of Pozuuoli, Naples (Italy).*

reason, the residual magnetization of the scanning table and the movement of the drive mechanism can reduce the SQUID performance. Thus, we proposed to reduce the noise due to the movement of the motors with a trick in the software control. Indeed, during the measurement the sensor is moving along a XY path and the motors are turned off when the sensor is fixed in a measurement position.

However, the noise due to a residual magnetization of the metallic parts, which form the scanning table and the rotational mechanisms, is reduced at the end of the

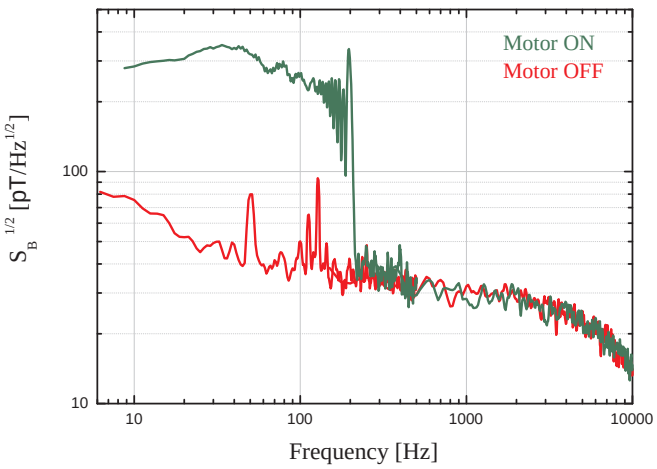

Figure 2.4: *Magnetic field noise of the microscope SQUID sensor in two μ-metal shields when the motor are turned on or off.*

measurements applying a background subtraction. In this way, the intrinsic peak-to-peak noise we measured, obtained by subtraction of two subsequent background measurements, was about 20 nT. We observed that it was a consequence of a residual magnetization of the sample-support due to a foregoing mechanical processing. In figure 2.5, on the left is shown the magnetic signal due to the sample-support, as it was supplied with the system. On the right, there is the magnetic signal of the background without the sample-support. The residual magnetization we observe is essentially due to the metallic parts of the rotational mechanism. Changing the sample support with one completely nonmagnetic and not subjected to mechanical working, the lowest intrinsic noise we measured was reduced by two orders of magnitude, and it is now of about 0.2 - 0.3 nT. Magnetic signals lower than this value cannot be distinguish by background noise.

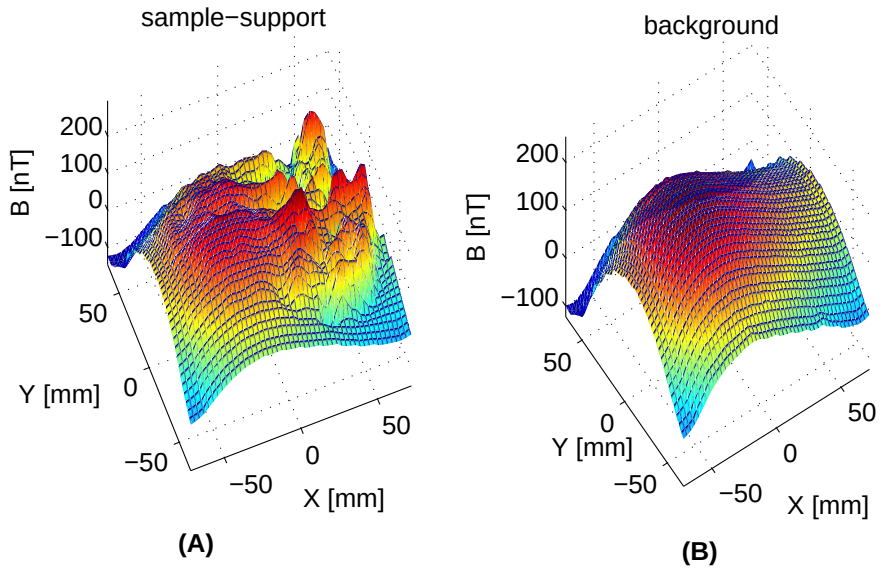

Figure 2.5: *Magnetic signal of sample-support due to foregoing mechanical processing (A) and after we substituted it with a nonmagnetic support (B).*

2.2.1 DC and AC measurements

The Scanning SQUID Microscope has been widely and successfully applied to study the basic physical properties of superconductor materials, such as the measurement of flux quantization in high-T_c superconducting microdisk [50], vortices trapped in YBCO thin-film [48, 70], observation of diamagnetic precursor to the Meissner state above Tc in high-Tc cuprates [55], imaging half-integer Josephson vortices in high-T_c YBCO grain boundaries [73], revealing antiferromagnetic ordering in arrays of superconducting π-rings [71], etc. [68, 116], and for the observation of domain structure in

magnetic materials, such as epitaxial thin film fabricated with growth temperature-gradient method [67]. These systems usually use low-T_c SQUID as sensor, which assures high magnetic field sensitivity only for low temperature samples.

However, there are prominent examples of successful applications of DC technique for samples at room-temperature. These are, for example, the study of magnetic properties of magnetic thin films [41, 47], detection of magnetic domain structures on data storage media [46, 49], geological [11, 9] or biological samples [43, 10], ferrous inclusions in aircraft turbine disks [114], few tiny ($\sim 100\mu m$) undesirable metallic or magnetic contaminants (Fe, Co, Ni, etc.) in products for food and pharmaceutical industry [36, 113, 111], and mechanical degradation of alloy steel caused by tensile deformation or by fatigue cycles [65].

The ability of the sensor to operate with relatively high magnetic fields allowed measurements of the dc and ac susceptibility of the microscopic objects. For this reason, according to the type of measurement, we distinguish two different techniques: alternating magnetic field (AC) and direct magnetic field (DC).

AC technique: it is actually used to detect surface and sub-surface defects in paramagnetic samples. We can apply an alternating magnetic field essentially in two different ways: *injecting* directly an AC current into the sample to find, for instance, fault currents in electronic devices, or *inducing* an AC current (known as *Eddy currents*) by means of an induction coil to find subsurface defects in a paramagnetic samples.

DC technique: it is used to measure the residual magnetization of ferromagnetic samples or, alternatively, in the presence of an additional static magnetic field (DC magnet ring) to enhance the magnetic response of paramagnetic and diamagnetic samples. Such techniques are schematically reported in figure 2.6.

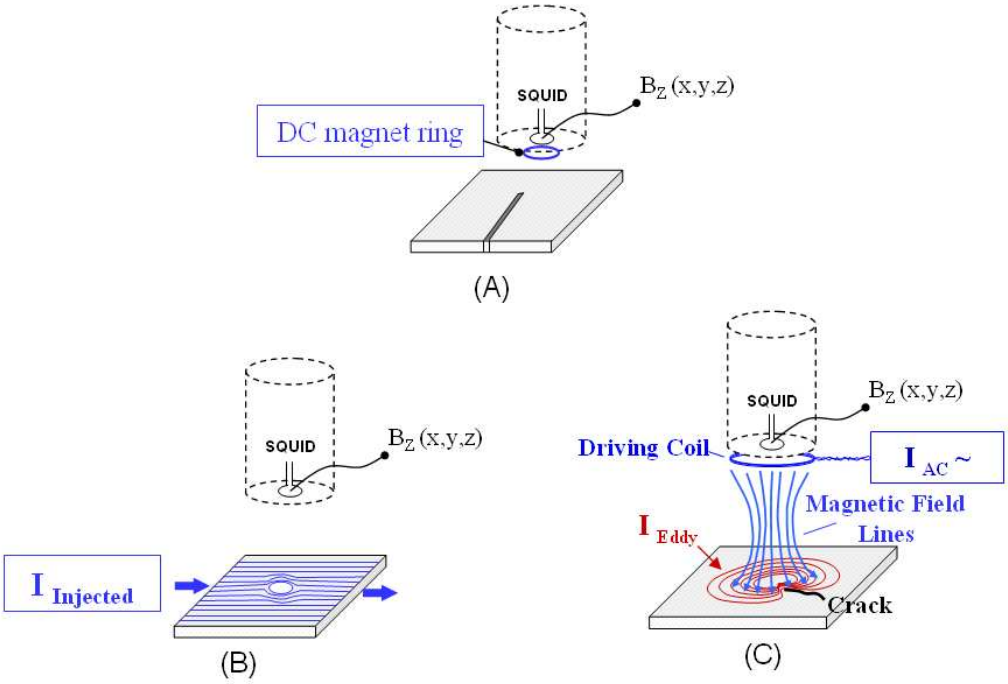

Figure 2.6: *Schematic representation of DC and AC techniques performed with SSM. (A) A direct measurement of the residual magnetization above a ferromagnetic sample surface. A magnet ring fixed on the bottom of the dewar can be used to enhance the signal of paramagnetic or diamagnetic samples; (B) and (C) Alternating magnetic field measurements: injection current and induced current technique, respectively.*

2.2.2 Lock-in technique

In the AC operational mode, a time-varying vertical magnetic field can be applied to the sample at frequencies up to 1 kHz. The AC field option includes an AC field coil, a filter-box, a control lock-in software for the excitation, and an imaging software to display both in-phase and in-quadrature information.

The AC coil is wound around a 18.8 mm diameter bobbin located at the bottom of the liquid nitrogen dewar, as shown in figure 2.7.

Figure 2.7: *Bottom view of the dewar showing the excitation coil, for AC measurements, centered to the SQUID loop. In the inset is shown a front view of the circular induction coil.*

A lock-in technique is used for AC measurements. It provides a DC output proportional to the AC signal under investigation [108]. A phase-sensitive detector (PSD), making such AC to DC conversion, which is essentially a multiplier, forms the heart of the instrument. It rectifies only the signal of interest, suppressing the effect of noise or interfering components which may accompany such signal. However, the noise at the input of the lock-in is not rectified, but it is returned at the output as an AC

fluctuation. This means that the desired signal response, now a DC level, can be separated from the noise by means of a narrow low-pass filter.

A wire diagram describing the operational modes of the SSM is shown in figure 2.8. In this configuration, the SQUID electronic (iMag-303, *Conductus*) is directly controlled by PC trough a GPIB card, the SQUID output and the filter box are connected to BNC box, the data are acquired through an Analog-to Digital Acquisition Card, and the XY stage position is connected to a motion control card.

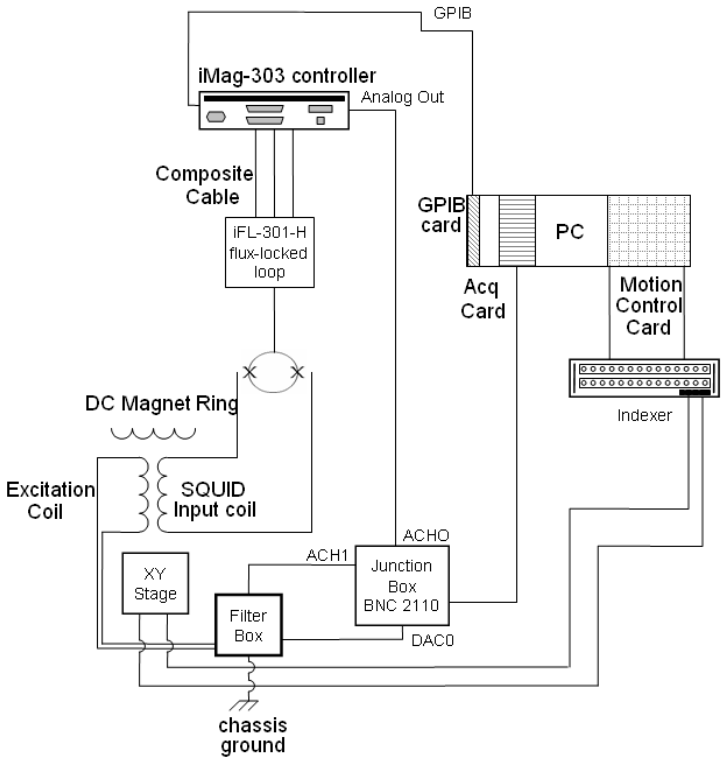

Figure 2.8: *DC and AC option SSM wiring diagram.*

In our SSM the lock-in is implemented via software. In figure 2.9, the wiring diagram for a software lock-in is shown. The excitation signal $V_L \sin(\omega t)$, a sinusoidal signal with chosen amplitude and frequency, is sent to the induction coil via software, by means of an output Digital-to-Analog Converter (DAC).

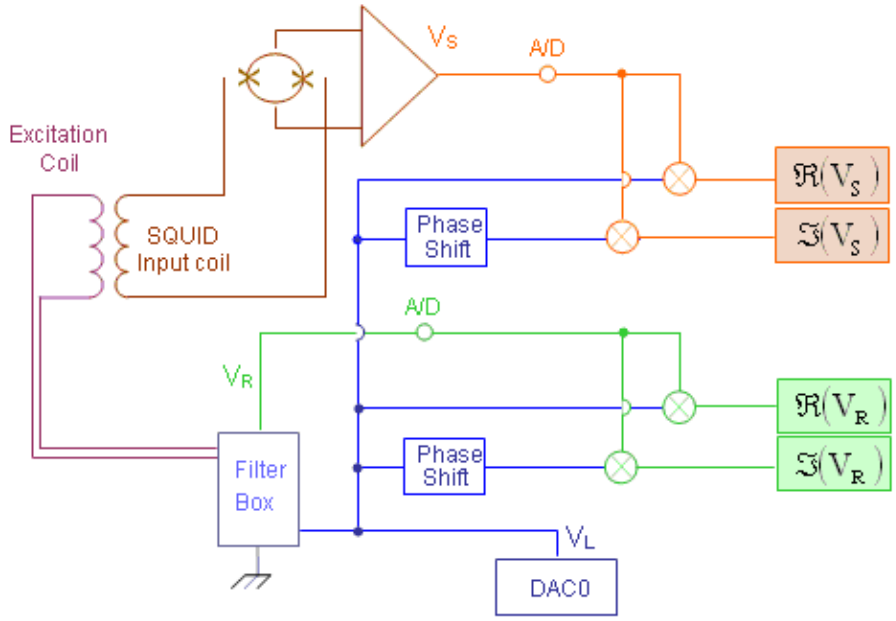

Figure 2.9: *Wiring diagram used to implement the lock-in software. The signals of the SQUID and the reference are multiplied by an internally generated signals, in-phase and out-of-phase with the excitation signal, respectively.*

The SQUID output signal V_S, coupled inductively to the pick-up of the SQUID, has the same frequency of the excitation signal V_L, but different phase. This signal is multiplied by $2\sin(\omega t)$ and $2\cos(\omega t)$, filtered and integrated, obtaining the "in-phase" and "in-quadrature" portion of the SQUID signal, respectively

$$\Re(V_S) = 2\sum[\sin(\omega t) \cdot V_S \sin(\omega t + \vartheta_S)] \approx V_S \cos\vartheta_S \tag{2.2.1}$$

$$\Im(V_S) = 2\sum[\cos(\omega t)\cdot V_S \sin(\omega t + \vartheta_S)] \approx V_S \sin\vartheta_S \tag{2.2.2}$$

At the same time, a reference signal V_R measured across a 330 Ω resistor in the filter box, is used to solve the uncertainty on the phase. It has the same frequency of the excitation signal V_L but different phase, not necessarily equal to the phase of V_S, so that the same algorithm has been applied to it. Again, it is multiplied by $2\sin(\omega t)$ and $2\cos(\omega t)$, filtered and integrated, obtaining $\Re(V_R) \approx V_R \cos\vartheta_R$ and $\Im(V_R) \approx V_R \sin\vartheta_R$, respectively. Finally, the ratio between these two quantities gives the measured complex signal $\frac{V_S}{V_R}e^{i(\vartheta_S - \vartheta_R)}$, where V_R is a known quantity. A description of how we use the in-phase and out-of-phase signals is widely dealt with in the next chapter.

2.3 Scanning SQUID Microscope Sensor

In this work a semi-commercial Scanning Magnetic Microscope model 770 purchased by *Tristan Technologies, Inc.* has been used. It utilizes high-T_c dc SQUID micro-magnetometer, positioned to measure the vertical component of the magnetic field. The SQUID structures were prepared from $YBa_2Cu_3O_{7-x}$ c-oriented films by a high oxygen pressure dc-sputtering technique [100]. The measured magnetic flux-to-field transfer coefficient of the SQUID is about 500 nT/Φ_0, and the magnetic flux-to-voltage transfer function is about 960 mV/Φ_0. The estimated energy resolution value for this sensor is 6.7 $\cdot 10^{-30}$ J/Hz in the white part of the noise spectrum.

The high-T_c SQUID is optimized for best compromise between spatial and magnetic field resolution, for operation at the liquid nitrogen temperature [40]. Sensitivity and spatial resolution depend on the sensing area dimension and the sensor-to-sample distance. The SQUID coil diameter δ is evaluated to be about 63 μm, which is the parameter that more influence the ultimate system spatial resolution.

The SQUID is glued on the end of a sapphire rod which provides the thermal contact of the SQUID assembly to the liquid nitrogen reservoir. The sensor is positioned in a Cu radiation shield and the SQUID-window standoff distance is fixed to be several tens of μm. The SQUID is read out with commercial dc-SQUID electronics (iMag Controller, Tristan Inc.) in a flux locked loop bias reversal mode [37].

The field resolution of the sensor was measured in shield and in unshielded laboratory environment, as shown in figure 2.11. During the measurements the stepper motors

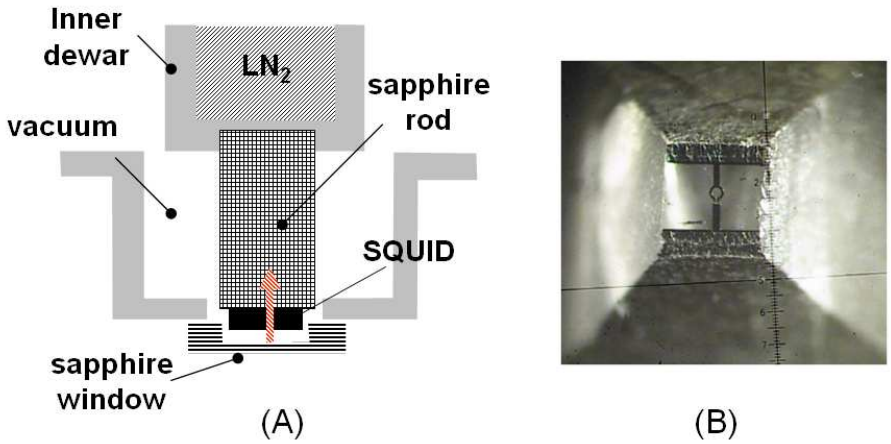

Figure 2.10: *(A) Schematic view of the bottom dewar and SQUID location. (B) Optical image of the SQUID sensor. The inner diameter of the loop is about 63 μm.*

of the positioning system were not connected. The white noise level is observed to be the same for both spectra. The magnetic field white noise spectral density is 20 pT/$Hz^{1/2}$ (measured at 5 kHz) and the operating bandwidth ranges from dc to 10 kHz. At frequencies below 100 Hz the signal spectrum shows $1/f$ noise knee, and the unshielded sensor demonstrates mainly environmental noise.

In order to achieve the best spatial resolution, the SQUID must be positioned as close as possible to the sample; a 50 μm thick sapphire window separates the sensor from room temperature, allowing to operate at a sample-to-sensor distance of few hundred microns. The effective distance between the sensor and the sample is adjusted through a laser beam. In order to calibrate the effective distance between the sample and the pickup coil, a 150 mm long and 25 μm diameter straight copper wire carrying a static current of I = 20 mA was scanned. The measured magnetic field

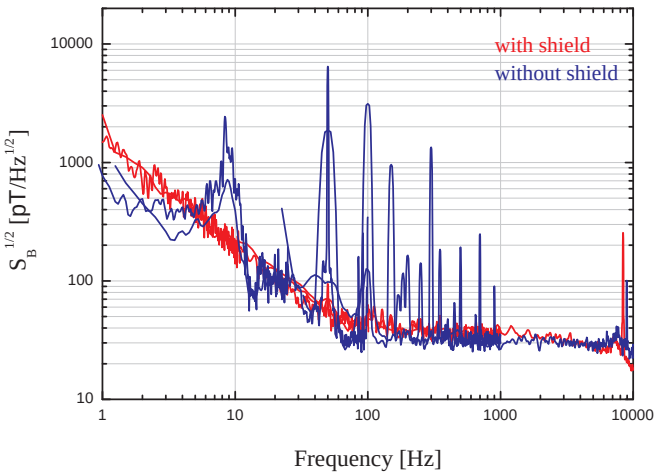

Figure 2.11: *Magnetic filed noise of the microscope SQUID sensor in the presence of two μ-metal shields (red curve) and in unshielded condition (blue curve).*

generated by the current in the wire is shown as cross-shaped dots in figure 2.12. The solid line results from the data fit through the equation $B_z(x, z_0, I)$

$$B_z(x, z_0, I) = \frac{\mu_o I}{2\pi} \frac{x - x_0}{[(x - x_0)^2 + z_0^2]} \tag{2.3.1}$$

where I is the applied current, x_0 is the location of the wire, z_0 is the SQUID to sample separation, and μ_0 is the permeability of the vacuum.

The only free parameter used was the wire-to-coil spacing. For the shown data the fit resulted in a wire to pickup coil distance of about $\approx 120\ \mu m$. The estimated separation value is in good agreement with the sum of the pickup coil-to-window distance, the thickness of the sapphire window, and the sample-to-window spacing.

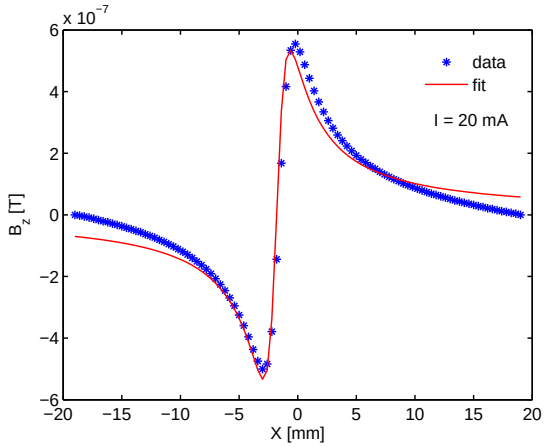

Figure 2.12: *Magnetic field from a 150 mm long, 25 µm diameter thick, straight copper wire carrying a current of 20 mA measured at a fixed height. The effective height was determined to be 120 µm by fitting (solid line) the magnetic field data from a wire (cross-shaped dots).*

2.3.1 Spatial Resolution and Magnetic Field Sensitivity

As it is well known, the sensitivity and spatial resolution depend both on the sensor diameter and sensor-to-sample distance. Here, we compute them in terms of dimensions of a simple SQUID magnetometer. The results can be useful to design, characterize and optimize new magnetometers and to do some considerations about our system performance.

Sensitivity

One way to compute sensitivity is to determine the minimum detectable magnetic moment at a given location on the coil axis. Let us to consider a magnetic dipole of

moment m_z oriented along the z-axis and positioned in the center of the pick-up coil, as shown in figure 2.13

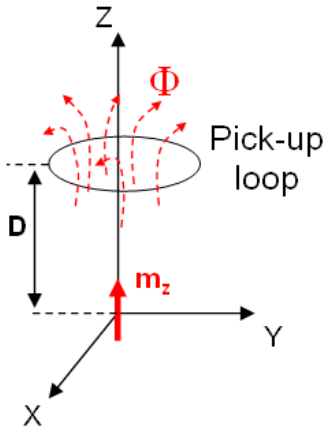

Figure 2.13: *Magnetic field generated by a magnetic dipole oriented along the z-axis and coupled to the pick-up loop of a magnetometer.*

The vector potential at position $\vec{r}$ (x, y, z) due to the magnetic moment $\vec{m}$ is

$$\vec{A}(\vec{r}) = \frac{\mu_0}{4\pi}\frac{m(x\hat{j} - y\hat{i})}{r^3} \tag{2.3.2}$$

where $\hat{i}$ and $\hat{j}$ are the unit vectors along the X and Y axes, respectively. The magnetic flux through the SQUID sensor Φ_{c0} is calculated integrating the vector potential along the closed loop of the circular sensor coil of radius r_s positioned at a height D. The integration gives [117]

$$\Phi_{c0} = \mu_0 m \frac{r_s^2}{2(D^2 + r_s^2)^{3/2}} \tag{2.3.3}$$

Equation 2.3.3 can be used to estimate the smallest detectable magnetic moment m^{min} by choosing Φ_{c0} as the total instrument flux noise $\Phi_{noise} = \sqrt{S_\Phi \Delta f}$. Therefore we write

$$m^{min} = \frac{2(D^2 + r_s^2)\Phi^{noise}}{\mu_0 r_s^2} \tag{2.3.4}$$

The equation 4.1.7 shows that the moment sensitivity is a function of the sensor size r_s, the sensor-to sample distance D, and the total flux noise Φ^{noise}. This latter quantity diverges for very small sensing area ($r_s \longrightarrow 0$), due to the small effective area of the sensor, and for very large SQUID sensors ($r_s \longrightarrow \infty$), due to the annulment of the magnetic moment flux through the loop. Deriving the equation 4.1.7, we obtain the optimal condition for $r_s = \sqrt{2}D$.

Spatial resolution

It is defined as the smallest detectable change in position of a single magnetic source, or the smallest detectable separation of multiple magnetic sources.

When the point magnetic dipole is scanned from the origin of the XY plane, along the x-axis with a small displacement $\delta \ll max(r_s, D)$, the flux $\Phi_{c\delta}$ becomes a complex function, as calculated and reported in [2]. However, it is possible to obtain an analytical expression for the spatial resolution, defined as the least detectable displacement

$$\delta^{min} = \{\frac{\Phi^{noise}}{\mu_0 m G(r_s, D)}\}^{1/2} \tag{2.3.5}$$

where G is a geometrical factor. Deriving the equation 4.1.8, we obtain the optimal condition $r_s = 0.59D$. However, δ shows an additional singularity at the critical point $r_{sc} = 2D$, where the worst resolution for a circular pick-up loop is obtained.

These considerations will be more incisive if we report on a graph the normalized values of m^{min} and δ^{min} as a function of the ratio between the sensor size r_s and the stand-off distance D, as shown in figure 2.14.

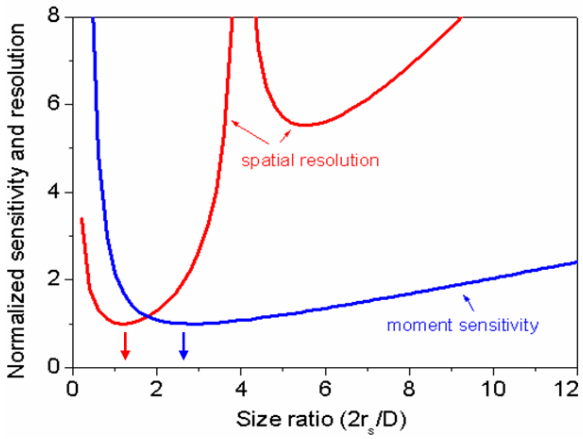

Figure 2.14: *The normalized moment sensitivity and spatial resolution versus the ratio between a circular-shaped sensor loop $2r_s$, and a sample-to-sensor distance D. The optimum size-to-distance ratios for moment sensitivity and spatial resolution are $2r_s/D = 2.82$ and 1.2, respectively. The spatial resolution diverges at $2r_s/D = 4$.*

In conclusion, the best condition for a high spatial resolution is reached when the sensor standoff distance is about double than the diameter coil. This is well realized in our SSM, where the SQUID diameter is about 63 μm, the standoff distance was estimated to be about 120 μm, and the coil diameter is about 60 μm. By increasing

the stand-off distance, the spatial resolution of the system gets worse. On the other hand, the worst critical condition for the spatial resolution (for $D = r_s/2$) is never realized in our SMM, because the radius of the pick up coil is always smaller than the minimum standoff distance that could be realized.

Chapter 3

Eddy Current Non Destructive Analysis

The principle of eddy current non destructive analysis (NDA) is based on the measurement of induced eddy currents in conducting objects, in the presence of time-varying magnetic fields. In general, electromagnetic problems can be usually divided into three categories: low frequencies, intermediate frequencies and high frequencies. At low frequencies static conditions are assumed; at high frequencies wave equations are used. However, in the intermediate frequency range, where diffusion equations are used, very few problems have been analytically solved. Eddy current problems fall into this intermediate frequency region.

The first section of this chapter is dedicate to the state-of-art of the eddy current analysis in terms of penetration depth and current distribution. Fundamental *diffusion equation* to eddy current problem is shown starting from the Maxwell's equations. An analytical solution of Eddy current distribution is presented for a linear, homogeneous and flawless conducting sample.

The second section is entirely dedicated to find novel analytical solutions to eddy current problem in presence of sample with defects. Here, eddy current magnetic field distribution as a function of the sensor position is derived in the case of a "thin" conducting plate. In this assumption, the induced magnetic field may be considered uniform along the sample thickness. Such innovative theoretical approach is used to analyze the acquired data of AC NDA technique.

In the last section, the capability and advantages of NDA systems based on Scanning SQUID Microscope has been exploited, focusing on the analysis of damage in joined metallic structures of aeronautical interest. A complete description of the AC signals ("in-phase" and "out-of-phase" components) is carried out. A *phase rotation analysis*, based on the principle of phase variation for defects at different depths, is performed to distinguish hidden defect signals enhancing their signatures. This analysis is widely discussed and corroborated by a series of experimental results on multi-layer metallic structures.

3.1 Eddy Currents

The principle of SQUID eddy current nondestructive analysis is based on the measurement of induced eddy currents in conducting materials when they are subject to time-varying magnetic fields $B_{Excitation}$, as shown in figure 3.1. The eddy current distribution in a metal (and its associated magnetic field B_{Eddy}) is disturbed when the eddy currents are induced in a region containing defects, like flaws or cracks. The presence of a flaw in conducting plates can be detected by measuring the change in B_{Eddy} as the sensor moves from a flawless region to that containing a flaw.

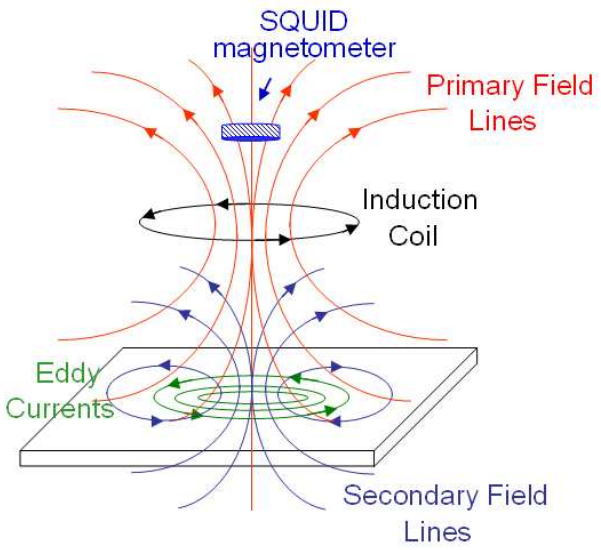

Figure 3.1: *Schematic representation of the primary and secondary magnetic field.*

.

Eddy currents are closed loops of induced current circulating in planes perpendicular to the magnetic flux. They normally travel parallel to the coil's winding and flow is limited to the area of the inducing magnetic field. Eddy currents concentrate near the

surface adjacent to the excitation coil and their strength decreases with distance from the coil. Eddy current density decreases exponentially with depth. This phenomenon is known as the *skin effect*.

The skin effect arises when the eddy currents flowing in the test object at any depth produce magnetic fields which oppose the primary field, thus reducing the net magnetic flux and causing a decrease in current flow as the depth increases. Alternatively, eddy currents near the surface can be viewed as shielding the coil's magnetic field, thereby weakening the magnetic field at greater depths and reducing induced currents. The depth that eddy currents penetrate into a material is affected by the frequency of the excitation current, electrical conductivity, and magnetic permeability of the specimen, as shown in the figure 3.2. In particular, it decreases with increasing frequency, conductivity, and magnetic permeability.

The depth at which eddy current density has decreased to 1/e, or about 37% of the surface density, is called the *standard depth of penetration* δ defined as

$$\delta = \sqrt{\frac{1}{\pi \mu \sigma f}} \tag{3.1.1}$$

where f [Hz] is the test frequency, μ [H/m] is the magnetic permeability of the material and σ [S/m] is its conductivity. Although eddy currents penetrate deeper than one standard depth of penetration, they decrease rapidly with depth. At two standard depths of penetration 2δ, eddy current density has decreased to $1/e$ squared or 13.5% of the surface density. At three depths 3δ the eddy current density is down to only 5% of the surface density.

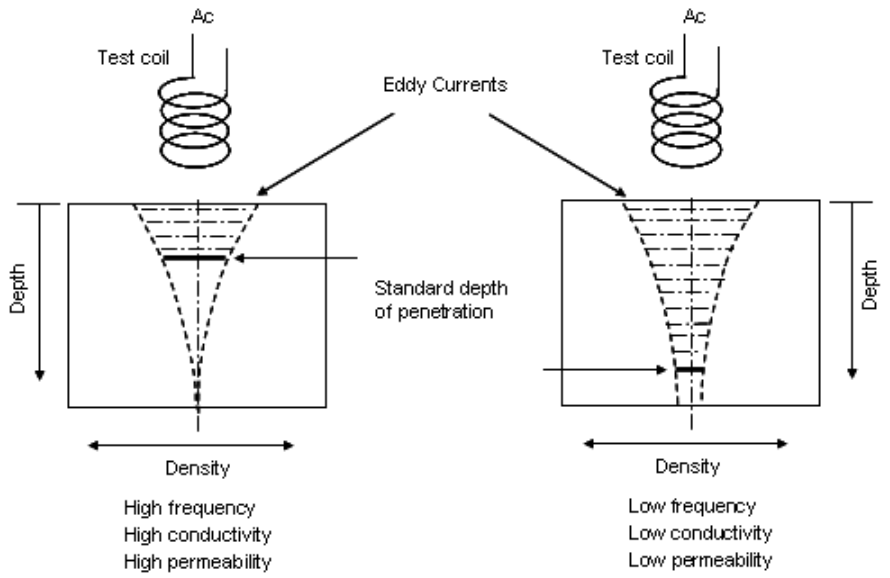

Figure 3.2: *Penetration depth as a function of excitation frequency, conductivity, and permeability of the sample.*

To date, many papers dealing with both theoretical and practical aspects of eddy current testing of materials have been produced [120, 36, 60, 19, 82]. The theoretical analysis for the eddy-current problem is important for the quantitative nondestructive evaluation. Till now, analytical solutions for the eddy current distributions have been studied for the unflawed samples excited by a sheet inducer [92] and a circular excitation coil [34, 29].

However, for flawed conducting samples, it is difficult to obtain the analytical formula for eddy-current distribution because of complex boundary conditions imposed by the presence of the flaw. For this reason, many authors investigate numerically the eddy-current distribution in a conducting sample with a flaw by using a Finite Element Method (FEM) [97, 86, 58, 24].

3.2 Mathematical Derivation of Eddy Currents

For the calculations in this work, it was assumed that the excitation field generated by the circular coil is less than few MHz, so that the displacement term in Maxwell's equations can be neglected. In addition, the sample was assumed to be non-magnetic with permeability $\mu = \mu_0$. A current carrying coil will give rise a magnetic field according to the Ampère's equation:

$$\nabla \times \mathbf{H} = \mathbf{J} \tag{3.2.1}$$

H can be written in terms of vector potential,

$$\nabla \times \mathbf{A} = \mu \mathbf{H} \tag{3.2.2}$$

Substituting Eq (3.2.2) into Eq (3.2.1),

$$\nabla \times \nabla \times \mathbf{A} = \mu \mathbf{J} \tag{3.2.3}$$

and remember the identity $\nabla \times \nabla \times \mathbf{A} = \nabla \cdot (\nabla \cdot A) - \nabla^2 \mathbf{A}$, with $\nabla \cdot A = 0$, we obtain

$$\nabla^2 \mathbf{A} = -\mu \mathbf{J} \tag{3.2.4}$$

where the total current **J** is given by the superposition of the current source and eddy current contribution:

$$\mathbf{J} = \sigma\mathbf{E} + \mathbf{J}_{source} \tag{3.2.5}$$

As a consequence, the Eq (3.2.4) can be written:

$$\nabla^2\mathbf{A} = -\mu\sigma\mathbf{E} - \mu\mathbf{J}_{source} \tag{3.2.6}$$

Using the Faraday's equation:

$$\nabla \times \mathbf{E} = -\partial\mathbf{B}/\partial t \tag{3.2.7}$$

B can be written in terms of vector potential:

$$\mathbf{B} = \nabla \times \mathbf{A} \tag{3.2.8}$$

Substituting Eq (3.2.8) into Eq (3.2.7), we obtain the relation:

$$\nabla \times (\mathbf{E} + \partial\mathbf{A}/\partial t) = 0 \tag{3.2.9}$$

that written in terms of the scalar potential ϕ becomes:

$$\mathbf{E} + \partial\mathbf{A}/\partial t = \nabla\phi \tag{3.2.10}$$

In the approximation of absence of free charge, the scalar potential can be chosen equal to zero, so that Eq (3.2.10) becomes:

$$\mathbf{E} = -\partial\mathbf{A}/\partial t \tag{3.2.11}$$

Finally, substituting the Eq (3.2.11) into Eq (3.2.6) we obtain the *vector potential diffusion equation*

$$\nabla^2\mathbf{A} = \mu\sigma\partial\mathbf{A}/\partial t - \mu\mathbf{J}_{source} \tag{3.2.12}$$

The Eq (3.2.12) is fundamental to understand the NDE techniques based on eddy-currents. For time harmonic fields, $\mathbf{E} = -\partial\mathbf{A}/\partial\mathbf{t} = -\jmath\omega\mathbf{A}$, so that Eq (3.2.4) becomes

$$\nabla^2\mathbf{A} = \jmath\omega\sigma\mu\mathbf{A} - \mu\mathbf{J}_{source} \tag{3.2.13}$$

Here, $\mathbf{A}$ is the magnetic vector potential, μ the magnetic permeability, $\mathbf{J}_{source}$ the current flowing through the excitation coil, σ the electrical conductivity and ω the frequency of the current flowing through the excitation coil, and $\jmath = \sqrt{-1}$. The first term on the right-hand side of Eq (3.2.13) represents the induced eddy currents.

In analogy to the diffusion equation (3.2.12), the same relations for $\mathbf{E}$, $\mathbf{J}$ and $\mathbf{H}$ can be written:

$$\nabla^2 \mathbf{E} = \mu\sigma \partial \mathbf{E}/\partial t \tag{3.2.14}$$

$$\nabla^2 \mathbf{J} = \mu\sigma \partial \mathbf{J}/\partial t \tag{3.2.15}$$

$$\nabla^2 \mathbf{H} = \mu\sigma \partial \mathbf{H}/\partial t \tag{3.2.16}$$

3.2.1 Penetration Depth

It is well know in NDE technique, that the sensitivity of flaw detection is decreased by raising the operation frequency.

In this section, we show how to calculate the penetration depth on a conductor of semi-infinite extension starting from the *magnetic field diffusion equation* reported previously.

If we consider a semi-infinite conductor and a time harmonic excitation field applied in the x direction, $H_x = H_0 e^{\jmath\omega t}$, the diffusion equation (3.2.16) becomes:

$$\frac{\partial^2 H_x(z,t)}{\partial z^2} = \mu\sigma \frac{\partial H_x(z,t)}{\partial t} \tag{3.2.17}$$

Assuming $H_x(z,t) = h(z)e^{\jmath\omega t}$ and substituting into Eq (3.2.17), $h(z)$ has to satisfy the equation:

$$\frac{\partial^2 h(z)}{\partial z^2} - \jmath\omega\mu\sigma h(z) = 0 \tag{3.2.18}$$

If we choose $h(z) = e^{-\jmath kz}$ as particular solution of Eq (3.2.18) with k to be determined, we find $k^2 = -\jmath\omega\sigma\mu$ and so:

$$k = \mp(\jmath - 1)\sqrt{\frac{\omega\mu\sigma}{2}} \tag{3.2.19}$$

Since k has the dimension of a length, we can obtain an expression for the *skin depth* δ defined as:

$$\delta = \frac{1}{k} = \sqrt{\frac{2}{\omega\mu\sigma}} \tag{3.2.20}$$

Hence, the skin depth effect limits the maximum depth of detection for any particular flaw size. The skin depth can be increased by lowering the operating frequency and therefore the typical dc to kHz bandwidth of the SQUID is a real advantage for SQUID NDE in the detection of subsurface flaws in conducting structures.

3.2.2 Eddy Current Distribution

In this section we find an expression for eddy current distribution as a function of δ and the depth z measured from the surface of conducting sample. Using the expression (3.2.19) found for k, we can write the solution of Eq (3.2.17) as:

$$H_x(z,t) = C_1 e^{-z/\delta} e^{\jmath(\omega t - z/\delta)} + C_2 e^{z/\delta} e^{\jmath(\omega t + z/\delta)} \tag{3.2.21}$$

To determine the constants, we derive $H_x = 0$ and $C_2 = 0$ for $z \to \infty$ and at the sample surface $H_x = H_0 e^{-\jmath\omega t}$ and $C_1 = H_0$, for $z = 0$.

Finally, by substituting the constants C_1 and C_2, the solution of Eq (3.2.17) can be written as

$$H_x(z,t) = H_0 e^{-z/\delta} e^{\jmath(\omega t - z/\delta)} \tag{3.2.22}$$

At the surface of the sample, the generated magnetic field has the same time dependence as the source current. However, as the magnetic field penetrates into the sample, because of the finite conductivity of the sample a phase-lag result and, $H_x \sim H_0 e^{\jmath(\omega t - z/\delta)}$, where the term $-z/\delta$ takes into account the penetration depth.

If we choose to express the *real component* of the magnetic field, we can write:

$$H_x(z,t) = H_0 e^{-z/\delta} \cos(\omega t - z/\delta) \tag{3.2.23}$$

where δ is the given by $(2/\mu\omega\sigma)^{1/2}$. The first term on the right side, $e^{-z/\delta}$, describes the penetration of the magnetic field in the medium, whereas the second term $\cos(\omega t - z/\delta)$ represents the wave propagation.

Consequently, using the Ampére's law $\mathbf{J} = \nabla \times \mathbf{H}$, we calculate the current distribution into our medium induced by a time-varying applied magnetic field. These currents are referred to as *eddy currents*, due to their similarity with the eddies in river water. Thus, deriving Eq (3.2.22), we observe that only the current component

in the y direction J_y is different from zero:

$$\nabla \times \mathbf{H} = \hat{\jmath}\frac{\partial H_x(z,t)}{\partial z} = \hat{\jmath} J_y \tag{3.2.24}$$

finally, we obtain an expression for the induced current, as follows:

$$J_y = \frac{H_0}{\delta} e^{-z/\delta}[e^{\jmath(\omega t - z/\delta - \frac{\pi}{2})} - e^{\jmath(\omega t - z/\delta)}] \tag{3.2.25}$$

In qualitative terms, the eddy currents are out of phase with the inducing field, proportional to the frequency of the applied field, and flow to oppose the changes in the applied field with time.

As done previously, arranging the Eq (3.2.25), we can express the *real component* of the induced current as:

$$J_y = -\frac{\sqrt{2}H_0}{\delta} e^{-z/\delta}\cos(\omega t - z/\delta + \pi/4) \tag{3.2.26}$$

The phase of the eddy current with respect to the excitation field is given by $-z/\delta + \pi/4$. The sign minus indicates that the induced currents generate a magnetic field which opposes itself to the applied field with time.

This approach has been possible because we have supposed an applied magnetic field $H_x = f(z,t)$ and so, we were able to solve directly the diffusion equation (3.2.16) for the magnetic field. In this contest, Dodd and Deeds [34] in 1968 found an analytical solution to eddy current problem with excitation coil located above plates of

various thickness, when a sinusoidal driving currents and linear, isotropic, and homogeneous media was assumed. This "closed-form" solution was obtained for two different conductor geometries and with the assumption of cylindrical symmetry.

More in general, for this electromagnetic problems, most people typically solve numerically the diffusion equation for the vector potential **A** (Eq 3.2.12).

When there is a defect in the plate, the eddy current distribution around the the flaw gets distorted. This modified distribution can be thought as a sum of the unperturbed distribution and a local perturbed distribution. The magnetic field associated with such a modified distribution is the defect magnetic field. Therefore, its phase $\phi(z)$ should also scale as $-z/\delta$, where z is now the depth of the flaw from the top of the plate. The linear relationship between the phase of the magnetic field generated by the defect and the flaw depth is in agreement with experiments with both the double-D [58, 59] and the sheet inducer excitation geometries [92]. The phase ϕ is also equal to $\tan^{-1}(B_{90^o}/B_{0^o})$, where B_{0^o} and B_{90^o} are the in-phase and in quadrature magnetic field components of the defect.

3.3 Eddy Current in Thin Conducting Plates

Another case can be solved analytically is when the thickness of the sample is negligible respect to the penetration depth δ. This condition is well carried out in low frequency regime. In this assumption, if we consider an external time-varying magnetic field $H_z^{(0)}$, applied normally to the plate, we can observe that the component of the applied magnetic field in the z direction is only a function of the variables (x, y) on the plane and is independent of z.

The induced eddy current in the plate is defined by the curl of the z component $H_z(x, y, t)$ of the magnetic field:

$$\mathbf{J} = \nabla \times (H_z \hat{k}) = -\hat{k} \times \nabla H_z \tag{3.3.1}$$

and expressing the previous relation in terms of the field components, it becomes:

$$\mathbf{J} = -\hat{k} \times (\hat{\imath}\frac{\partial H_z}{\partial x} + \hat{\jmath}\frac{\partial H_z}{\partial y}) = \hat{\imath}\frac{\partial H_z}{\partial y} - \hat{\jmath}\frac{\partial H_z}{\partial x} \tag{3.3.2}$$

The Eq (3.3.2) guarantees that the induced current $\mathbf{J}$ has only the two in-plane components, $J_x = \partial H_z/\partial y$ and $J_y = -\partial H_z/\partial x$, respectively.

The governing diffusion equation (3.2.16) for $H_z(x, y, t)$, becomes:

$$\frac{\partial^2 H_z}{\partial x^2} + \frac{\partial^2 H_z}{\partial y^2} = \mu\sigma\frac{\partial H_z}{\partial t} \tag{3.3.3}$$

3.3.1 Magnetic Field Distribution in a flawed plate

Equation (3.3.3) could be solved analytically, as done for the Eq (3.2.17), in the assumption of flawless thin conducting plate. More interesting, it would be to find a solution to eddy current problem when there is a flaw in the sample and thus, when the cylindrical symmetry is no longer valid. Nevertheless, we have derived an analytical solution in the case of "thin" flawed conducting plate. In this assumption, we can neglect the variation of the magnetic field along the thickness of the sample.

As a simple case, we consider a thin conducting plate with a defect of circular shape of radius a and we assume that the plate is large enough to neglect the border effects, as shown schematically in figure 3.3.

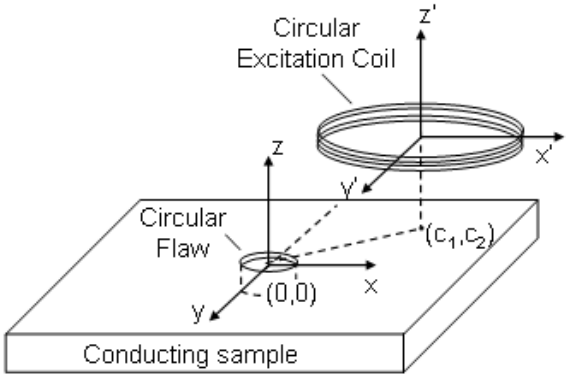

Figure 3.3: *A circular flaw of radius a is positioned in the center of the plate and in the origin of the reference system. The circular induction coil is located on the plate and the projection of its center has coordinates* (c_1, c_2).

The magnetic field in the Eq. (3.3.3) can be written as the sum of two components, $H_z = H_z^{(0)} + H_z^{(1)}$, where $H_z^{(1)}$ is the self-magnetic field due to the eddy current **J** in the plate. Substituting this relation in the equation 3.3.3 and observing that for

the external magnetic field $H_z^{(0)}$ is $\nabla_{xy}^2 H_z^{(0)} = 0$, we obtain

$$\frac{\partial^2 H_z^{(1)}}{\partial x^2} + \frac{\partial^2 H_z^{(1)}}{\partial y^2} = \mu\sigma\frac{\partial H_z^{(0)}}{\partial t} + \mu\sigma\frac{\partial H_z^{(1)}}{\partial t} \tag{3.3.4}$$

Neglecting the time dependence of the self-magnetic field $H_z^{(1)}$ with respect to the applied field $H_z^{(0)}$, the Eq (3.3.4) becomes

$$\frac{\partial^2 H_z^{(1)}}{\partial x^2} + \frac{\partial^2 H_z^{(1)}}{\partial y^2} = \mu\sigma\frac{\partial H_z^{(0)}}{\partial t} \tag{3.3.5}$$

In addition, we chose an harmonic time dependence for the applied magnetic field, i. e. $H_z^{(0)} = H_0 e^{\jmath\omega t}$. We assume that H_0 has a constant value in a circular region of radius R under the coil and it is zero outside. If the solution of the Eq (3.3.5) is assumed to be $H_z^{(1)}(x, y, t) = \bar{H}_z(x, y)e^{\jmath\omega t}$, we finally obtain:

$$\frac{\partial^2 \bar{H}_z(x, y)}{\partial x^2} + \frac{\partial^2 \bar{H}_z(x, y)}{\partial y^2} = \jmath\omega\mu\sigma H_0 \tag{3.3.6}$$

The boundary condition requires that the current on the border of the defect has only a tangential component. This condition is equivalent to the requirement that H_z is equal to a constant on the border of the defect. More in general, $H_z(x, y) = const.$ determines the current density flux line family.

It is possible to show [6] that the solution to Eq (3.3.6), satisfying the required boundary condition, is the following:

$$\bar{H}_z - \bar{H}_z^{center} = \frac{\jmath H_0}{\delta^2}[(x-c_1)^2 + (y-c_2)^2 - c_1^2 - c_2^2] \times$$
$$(1 - \frac{a^2}{x^2+y^2}) + \frac{\jmath H_0}{\delta^2}(c_1^2 + c_2^2 - a^2); \qquad with \quad x^2 + y^2 \geq a^2 \tag{3.3.7}$$

As stated above, we assumed that an uniform applied magnetic field $H_z^{(0)}$ extends over a circular area of the plate having radius R. The constants (c_1, c_2), appearing in the solution 3.3.7, are just the coordinates of the center of this circle on the plate. In this point, the field is denoted as $\bar{H}_z^{center} \equiv \bar{H}_z(c_1, c_2)$.

This solution is shown in figure 3.4, where the lines represent the magnetic field distribution on the plate around the defect, which are obtained for constant values of the level curves $\bar{H}_z(x,y) - \bar{H}_z^{center}$ extending to a circular region of radius R. This solution can be calculated for each point on the horizontal scanning position.

3.3.2 Eddy Current Density in the plate

Knowing the spatial variation of the magnetic field on the plate $\bar{H}_z(x,y)$ from Eq (3.3.7), we can derive the expression for the magnetic field $H_z(x,y,t) = \bar{H}_z(x,y)e^{j\omega t}$. Since the current density is equal to the curl of the magnetic filed , we can calculate the components of the eddy current density excited in the plate, namely:

$$J_x = \frac{H_0}{\delta^2}\left[2y - \frac{(2a^2y)\,(2c_1x + 2c_2y)}{(x^2+y^2)^2} - c_2\left(2 - \frac{2a^2}{x^2+y^2}\right)\right]e^{j(\omega t + \pi/2)}$$
$$J_y = \frac{H_0}{\delta^2}\left[-2x + \frac{(2a^2x)\,(2c_1x + 2c_2y)}{(x^2+y^2)^2} + c_1\left(2 - \frac{2a^2}{x^2+y^2}\right)\right]e^{j(\omega t + \pi/2)} \tag{3.3.8}$$

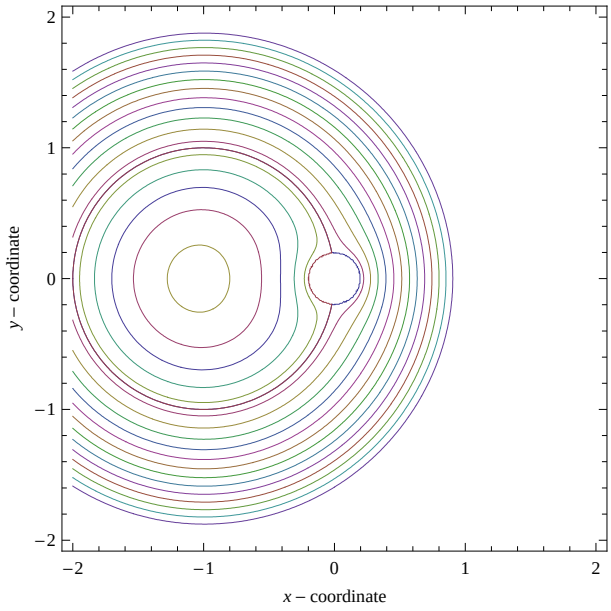

Figure 3.4: *A representation of the magnetic field distribution around the defect obtained by plotting the level curves of the magnetic field z component,* $\bar{H}_z - \bar{H}_z^{center} = const$*, as solution of the Eq 3.3.7. The flaw of radius a is in the origin of the reference system (0, 0) and the exciting coil center in this frame is positioned at (-1, 0). The linear increment of the current starting from the coil center is visible.*

We can observe that in the absence of flaw ($a = 0$), the current density represented by this solution varies linearly from the point (c_1, c_2) on the plate, corresponding to the center of the coil of an arbitrary radius R, which we consider as the extension of the eddy current on the plate. Moreover, this linear current behavior is related to the choice of an uniform normal field generated by the coil in the circular area of radius R.

3.3.3 Eddy Current Magnetic Field at the sensor position

However, we are interested to measure the magnetic field at the sensor position. In general, the magnetic field $\mathbf{B}(\vec{r})$ at point $\vec{r}$ is given by the law of Biot and Savart

$$\mathbf{H} = \frac{1}{4\pi} \int \frac{\mathbf{J}(\mathbf{r}') \times (\mathbf{r} - \mathbf{r}')}{|\mathbf{r} - \mathbf{r}'|^3} d\mathbf{r}' \tag{3.3.9}$$

where $\mathbf{J}$ is the current density at point $\vec{r}'$.

In our case, since the sensor we used measures the z-component of the magnetic field, we choose to calculate only H_z given by

$$H_z = \frac{d}{4\pi} \int \int \frac{J_x(x', y')(y - y') - J_y(x', y')(x - x')}{[(x - x')^2 + (y - y')^2 + z^2]^{3/2}} dx' dy' \tag{3.3.10}$$

where d is the thickness of the plate and z is the sensor to plate distance.

The signal detected by the sensor, when the defect is moving along the x-axis under the SQUID, can be calculated by evaluating the integral (3.3.10) over a cycle, in which the value of c_2 is fixed to zero and c_1 is incremented of an arbitrary step. This is equivalent to move the exciting coil over the flaw, as done in the simulating program. The results of this procedure are reported in figure 3.5, where the magnetic field at sensor position generated by a circular defect of radius $a = 1$ is calculated for different z distances. Each dimensions used in the simulations are normalized in terms of the skin depth δ.

Although the magnetic field signals, calculated through Eq (3.3.10) has an amount of uncertainty due to the introduced approximations, the results we obtained are in

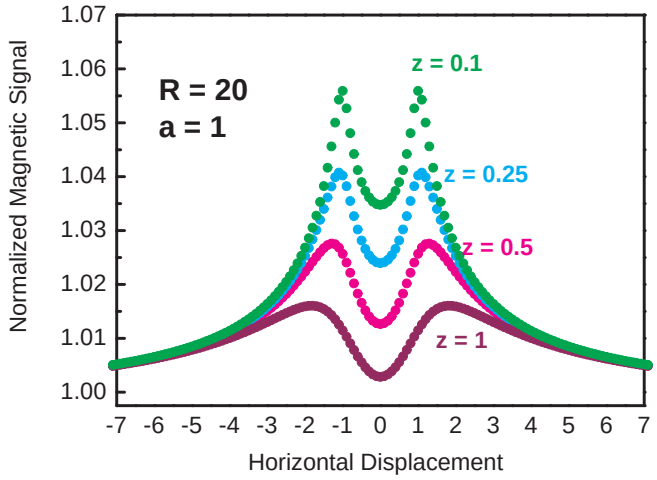

Figure 3.5: *Scan simulations of magnetic field recorded as a function of the horizontal position above a circular defect of radius a. The value used for the area of interest for the eddy current is* $R = 20$. *The curves correspond to different scanning quotes:* z *varies from 0.1 to 1 in units of* δ. *Each value must be meant as normalized with respect to the skin depth* δ.

qualitative good agreement with the experiment. This characteristic behavior shows two peaks, when the center of the induction coil is just above the border defect, and a valley when it is exactly on the center of the defect. Increasing the distance sensor-to-defect, the signature of peaks and valley becomes less intensive.

This result will be reminded in the following section, to compare it with the experimental eddy current data, detected above a circular defect of 4.5 mm diameter in a thin conducting plate.

3.4 Scanning SQUID Microscope for NDE Applications

Various non-destructive testing (NDT) techniques, such as ultrasonics, radiography, penetrants, magnetics, eddy currents and acoustic emissions have been tested to determine the integrity of the structure, component or material as requirement in both quality control for manufacturing processes and traditional flaw detection. The choice of the NDT industry for an appropriate NDT method focuses on an optimum balance between quality control and cost effectiveness.

Because of its higher costs and handling inconvenience, SQUID technology might be used only where standard NDT techniques fail to ensure sufficiently high reliability. The conventional eddy current techniques are sensitive in detecting the surface-breaking cracks. However, these methods are not sensitive enough for the detection of deep flaws due to their poor resolution at low frequencies.

One of the most important advantages to use a SQUID system is exactly the high field sensitivity at low frequencies which provides an outstanding dynamic range with remarkably high signal to noise ratio of the measured field distribution. This characteristic offers an advantage for application where low excitation frequency is necessary for detection at large penetration depth in multilayer structures, rivet plates and aircraft wheels [63, 94, 85, 84, 83, 3, 81].

In SQUID-based NDE systems, the sample is excited with an ac excitation field and the magnetic signal due to the generated eddy currents in the plate is measured. Typical excitation field devices are sheet inducers, absolute coil exciters and differential double-D coils, as reported by Braginski and Krause [19] and schematically shown

in figure 3.6.

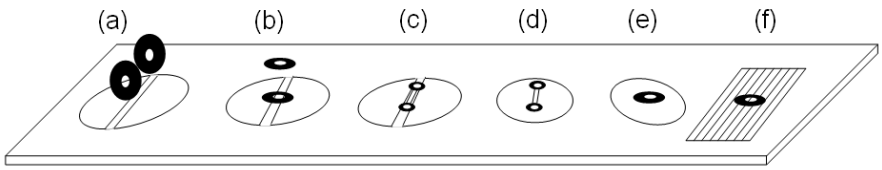

Figure 3.6: *Typical configurations of inducer coils as reported by Braginski and Krause [19]: (a) to (c) Differential double-D coils with (a) axial gradiometer in plane, (b) axial gradiometer normal to plane, (c) planar gradiometer; (d) and (e) absolute exciters with planar gradiometer (d) and magnetometer (e); (f) sheet inducer.*

The change of field response can be regarded as a function of a series of parameters as reported [19] and shown in figure 3.7, respectively. The defect magnetic field can be regarded as consisting of different components, as explained in [82]:

◦ the surface current density,

◦ the exponential decay of the excitation field, governed by a decay coefficient $-z/\delta$,

◦ the interaction process of the current density with the flaw

◦ the decay of the return field.

Many efforts have been made to find a correlation between the magnetic signal due to a flaw and the investigation of its dimension and depth. Yu Pei Ma and John Wikswo [92], using a sheet inducer, demonstrated that the analysis of the phase of the magnetic signal provides useful information about the depth of the flaw. In fact, it is well know that there is a relationship between the phase of the magnetic signal and the depth of the flaw due to the skin effect. It was found that for a fixed excitation frequency, the phase of the measured signal varies linearly to the depth of the slot,

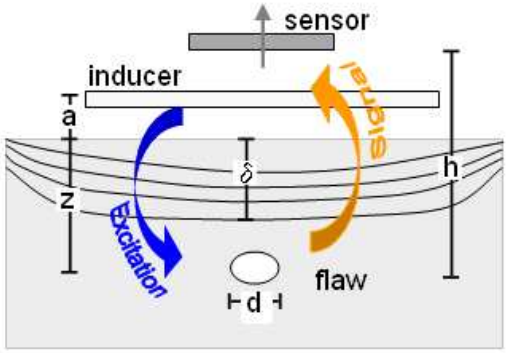

Figure 3.7: *Typical important parameters in NDE testing as reported by Braginski and Krause [19]: d - flaw diameter or size, z - flaw depth, h - sensor to flaw distance, a - separation of inducer above test object surface or stand-off distance, δ - skin depth.*

while the amplitude is correlated with the the height of the slot [59, 58, 53].

As in other NDE fields, imaging technique are useful to facilitate the interpretation of measurement data obtained by SQUID magnetometry. There are essentially two different approaches for processing of SQUID NDE data: flaw detection and field deconvolution into current patterns. In this work, we want to emphasize the flaw detection.

To this aim, we utilized a circular coil to characterize defects in conducting plates at different depths. We show that the components of the measured signal are useful in determining buried flaws in according with the high sensitivity of the SQUID system. Hence, quantitative evaluation of flaws can be achieved by analyzing the amplitude and the phase of the measured signals, in according with the experimental data. More in particular, we focalize the attention on a particular application of crack detection in aircraft components.

3.4.1 The Signal Components

Using the lock-in technique, for which more accurate description we refer to the lock-in paragraph in chapter 2, the SQUID signal and the reference signal are multiplied. The result after that the signal passes through a low pass filter is a dc signal proportional to the amplitude of the signal coming from the sample and the cosine of the phase angle between the SQUID and the reference signals, namely $\frac{1}{2}V_s V_L \cos\theta_s$. To obtain phase information, the reference signal is also connected to a 90^o phase shifter. Multiplying again the SQUID signal and the reference signal shifted by 90^o, we obtain again a dc signal $\frac{1}{2}V_s V_L \sin\theta_s$.

Since V_L is the amplitude of the reference signal and it is known, we can define two quantities: $B_{0^o} = V_s \cos\theta$ and $B_{90^o} = V_s \sin\theta$. These are, respectively, the *"in-phase"* or *real* and *"in-quadrature"* or *imaginary* portions of the signal. Thus, two data fields are typically recorded during each scan and together they represent the complex response of the sample.

To probe the dependence of the excited magnetic field from the crack in a sample and to show how it can be used to detect buried defects, as first simple case, we considered an aluminium plate with a circular defect. The geometry of the simulated flawed sample is shown in figure 3.8. The circular defect has a diameter of 4.5 mm and the thickness of the plate is 3 mm. The circular coil, which is 18.8 mm in diameter, is fed with 0.4 V at 889 Hz excitation frequency generating the applied magnetic field.

When the coil scans over the slot, the in-phase B_{0^o} and in-quadrature B_{90^o} components of the excited magnetic field are recorded as a function of the horizontal position, as shown in figure 3.9, and they are found to oscillate up-and-down.

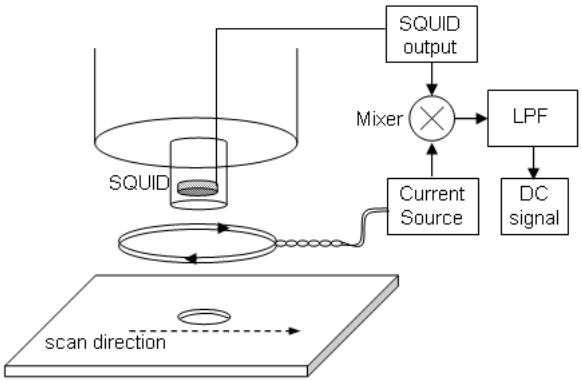

Figure 3.8: *A schematic description of the lock-in technique: the SQUID and the reference signals are multiplied and filtered through a low-pass filter. The result are two dc signal "in-phase" and "in-quadrature" with the inducing signal. The sample, an aluminium plate with a circular defect 4.5 mm in diameter, moves under the sensor in the x-direction.*

At position a or c of figure 3.9, the real and imaginary components show a large variation since the center of the circular coil is just above the slot. As a consequence of their phase shift, B_{0^o} and B_{90^o} show a maximum and a flex in the points a and c, respectively. At point b, the center of the circular coil is exactly in the middle of the slot, and the two components of the signal show a coincident valley or a peak, respectively.

The magnetic field component, in-phase with the inducing field, shows the behavior we found in our simulation (see figure 3.5), with a valley when the the center of the coil is exactly above the slot (position b), and two peaks when the center coil is just above the slot (positions a and c).

We may solve these two signals for the magnitude, $V_S = \sqrt{B_{0^o}^2 + B_{90^o}^2}$, and phase,

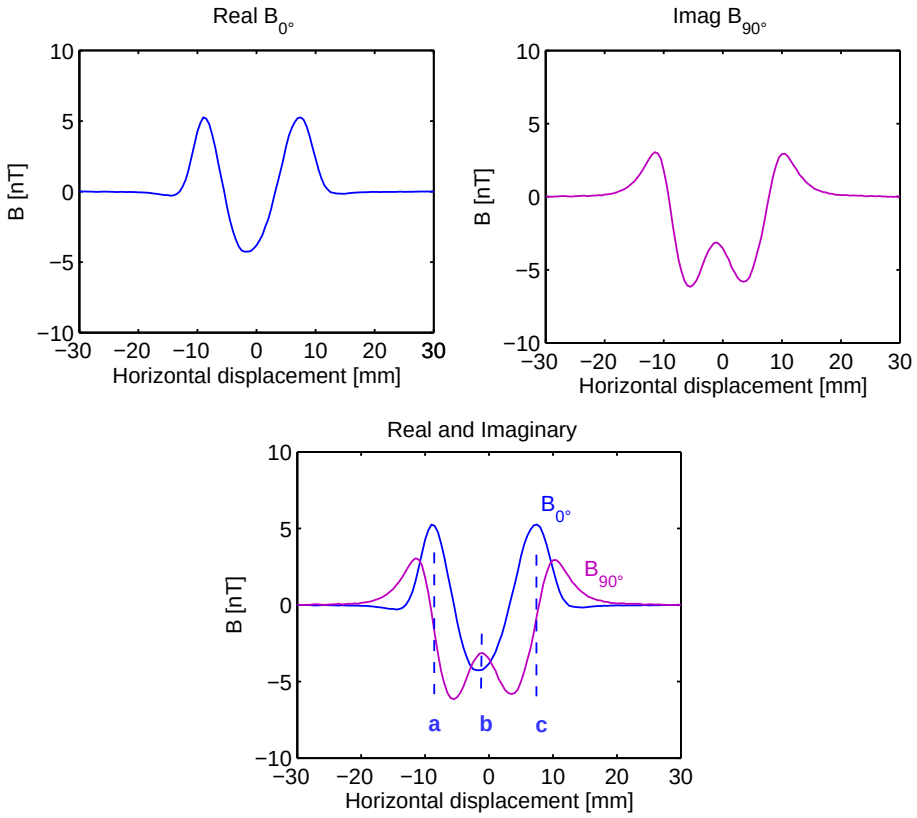

Figure 3.9: *Above: the real B_{0^o} and imaginary B_{90^o} components of the excited magnetic field recorded as a function of the horizontal position above a circular slot of 4.5 mm diameter. Below: the superposition of the two signals: a and c are the extremes on the border of the defect and b indicates the center of the defect.*

$\theta = \tan^{-1}(B_{90^o}/B_{0^o})$, of the SQUID signal, shown in figure 3.10 as a function of the horizontal position. The phase at the position far away from the slot differs from that near the slot. It was found [59] that the phase rises linearly with an increased defect

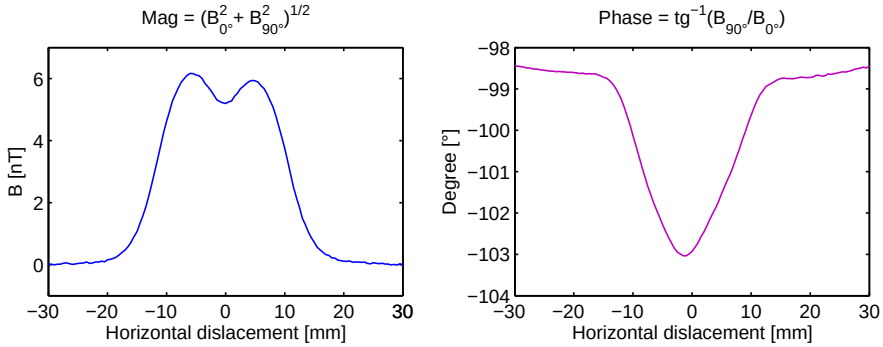

Figure 3.10: *The magnitude* $\sqrt{B_{0^o}^2 + B_{90^o}^2}$ *and the phase* $\tan^{-1}(B_{90^o}/B_{0^o})$ *of the SQUID signal as a function of the horizontal position above a circular slot of 4.5 mm diameter.*

depth and the slope of this linear function is found to be proportional to $f^{1/2}$. This dependence can be argued by considering the skin effect for a semi-infinite conducting slab with an uniform excited current density on the surface.

However, the defect field is usually accompanied by an offset field, which may be caused by different reasons, such as the tilting of the coil exciter or the residual magnetization of components close to the sample. The figure 3.11, for example, shows magnitude and phase of the SQUID signal when scanned above an aluminium alloy plate with two circular defects on the surface, separated by a 25 mm distance. The *lift-off effect* on the magnitude and phase SQUID signal is shown in the two images on the left side, while on the right side these signals are depurated of the lift-off effect. It was reported that the unwanted offset can be removed by using proper adjustment

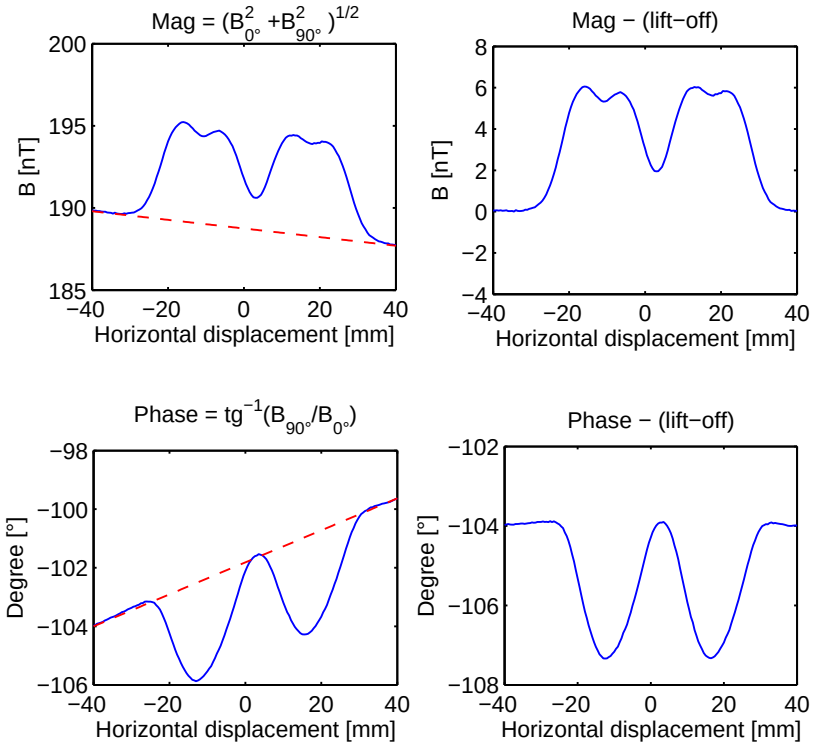

Figure 3.11: *Basic principle of straight line subtraction we used to minimize the lift-off effect. Above: (left) Magnitude of SQUID signal across two circular slots in an aluminium alloy plate both 4.5 mm in diameter and (rigth) the effect of the correction. Below: (left) Phase of SQUID signal across two circular slots and (right) the effect of the correction.*

of the phase or software filtering [95] or an additional compensation [59, 91]. Until now, we have dealt with signals due to a defects on the surface. In the next section, we will explore how we can enhance the induced eddy current data due to defects buried under the surface with a depth-selective analysis, as shown by Ma and Wikswo [92] for a sheet inducer. Reducing the lift-off effect can be useful to enhance the signal with respect to the system intrinsic noise.

3.4.2 Phase Rotation Analysis for Investigation of Hidden Defects

In this section, we show how to obtain information on the depth of subsurface defects from the eddy current induced in a plate by a perpendicular uniform ac field.

To this aim, we have tested aluminium-titanium alloy planar samples of $200 \times 200 \times 3\ mm^3$ with artificial defects. A plate with two circular flaws is inserted between two flawless plates to simulate the presence of defects inside a slab. The geometry of the simulated flawed sample is show in figure 3.12. The two circular defects are both 4.5

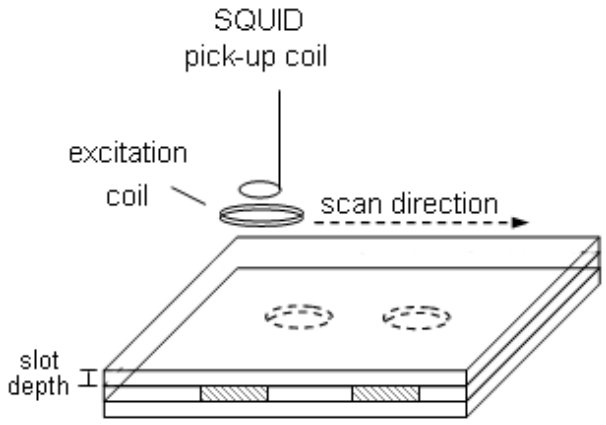

Figure 3.12: *Sketch of AlTi sample with two defects under a flawless plate. Every plate is* $200 \times 200 \times 3mm^3$ *in dimension and two circular defects are 4.5 mm in diameter are positioned in the middle plate.*

mm in diameter and the horizontal distance between the defects is $\Delta x = 25$ mm. The depth of the defects is measured from the top of the stack to the half thickness of the slotted plate. The top surface is estimated 2 mm away from the bottom of the dewar. Thus, in this first configuration, the the distance of the two hidden defects from the sensor is longer than 5 mm. The positioning stage was moved along the

x-direction with a scanning step of 500 μm and the excitation coil is fed sinusoidally with frequency 889 Hz and amplitude 400 mV. Due to the fact that the defects are buried under the surface, the induced magnetic field is lower than the previous case and the lift-off effect has a considerable weight.

For this reason, in order to separate the defect signal from the background, we apply a *phase rotation* analysis at the component of the induced magnetic field. Indeed, since at any particular depth, the magnetic field component in-phase with the inducing magnetic field is $B_{0^o} = V_s \cos\theta$, the component 30^o out-of-phase with the inducing field is $B'_{30^o} = V_s \cos(\theta - 30^o)$ that for any angles becomes $B'(\phi) = V_s \cos(\theta - \phi)$.

Figure 3.13, shows the results of the calculations for $\phi = 0^o$, 45^o, 95^o, and 135^o. At $\phi = 0^o$, the in-phase signal is small and it is evident the lift-off effect; at $\phi = 45^o$ the signal increases; at $\phi = 95^o$ the signal through the defects has the largest increment; finally, at $\phi = 135^o$ the signal reverses its polarity. This shows the promise of this analysis to detect subsurface flaws and to distinguish them from features in a magnetic image obtained at the surface.In addition, the horizontal distance between the slots is found to be 2.5 cm according to the distance between the minimum peaks. This evaluated distance is exactly the distance between the defects.

After that, the flawed plate has been covered with two flawless plates to simulate deeper hidden defects. The dimensions of the samples are the same as in the previous example. The only difference, now, is that the sensor-to-defect distance is estimated to be about 8 mm. The circular coil is fed sinusoidally with an excitation frequency of 421 Hz and amplitude of 2 V. During the scan, the in-phase and out-of-phase

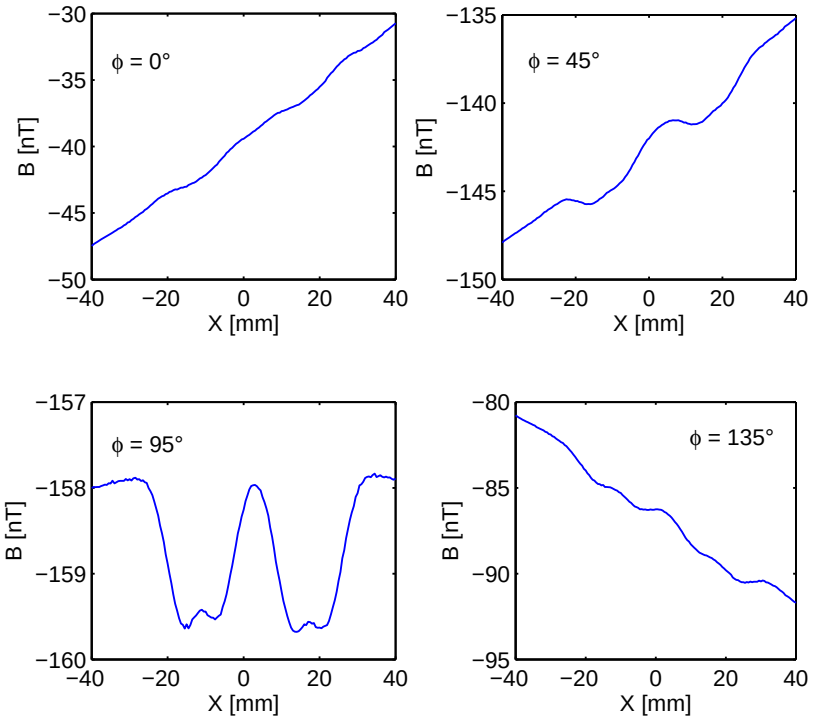

Figure 3.13: *The phase angle rotation analysis in the excited magnetic field normal to the plate surface due to two circular defects, as a function of the horizontal position. Both the defects were 4.5 mm in diameter and they were hidden under the top plate. At $\phi = 0^o$, the signal is completely covered by lift-off effect; for $\phi = 45^o$ the signal is incremented; at $\phi = 95^o$ the signal through the defects has the largest increment since the lift-off effect is completely eliminated; for $\phi = 135^o$ the signal reverses its polarity.*

components of the excited magnetic field are aquired as a function of the horizontal position with a scanning step of 500 μm.

Due to the screening current induced on the top surface and the reduction of eddy current with the depth, we applied again a phase rotation to minimize the surface signal and enhance the defect signal. As an example, in figure 3.14, are shown the resulting field after this signal processing step for $\phi = 0^o$, 45^o, 55^o, and 75^o. It is clear that the best result is obtained for $\phi = 55^o$, even though we can observe that the excited magnetic field is noisier than the previous case, since it is closer to the system intrinsic noise of order of 0.2 - 0.3 nT. However, the horizontal distance between the slots is estimated to be 2.5 cm, once again in agreement with the actual distance between the two defects.

Finally, we treat the case in which we are in presence of signals generated by both surface and sub-surface defects. The specimen, two piled up aluminium alloy plates with two defects on the surface and two defects under the surface as shown in the sketch in figure 3.15, was scanned in the X-Y plane using the induction coil.

Figure 3.16 shows this analysis applied to a specimen with two simulated defects under the surface. The 2D contour plots for the acquired signals across the sample are reported for different values of the phase angle. We see that the signal component at $\phi = 0^o$, in-phase with the inducing field, shows that only the defect on the surface has large signature; when we increase the values of the phase angle, for instance $\phi = 45^o$, the two defects under the surface appear; for $\phi = 95^o$, the signature of the two hidden

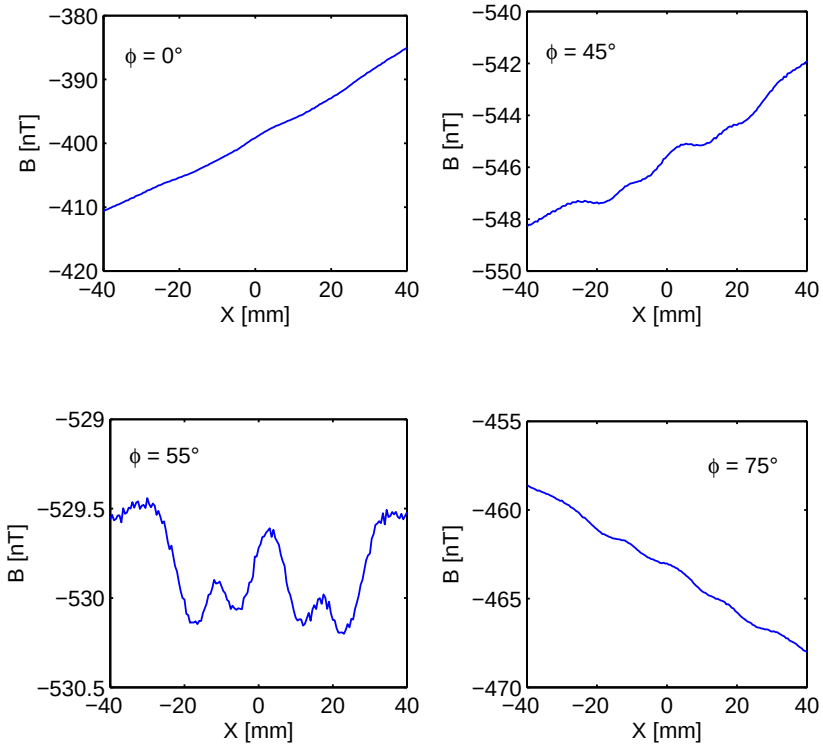

Figure 3.14: *The phase angles rotation analysis in the excited magnetic field normal to the plate surface due to two circular defects, as a function of the horizontal position. Both the defects were 4.5 mm in diameter and they were hidden under two plates. At $\phi = 0^o$, the signal is completely covered by lift-off effect; for $\phi = 45^o$ the signal is incremented; at $\phi = 55^o$ the signal through the defects shows the largest increment since the lift-off effect is completely eliminated; finally, at $\phi = 75^o$ the signal reverses the polarity.*

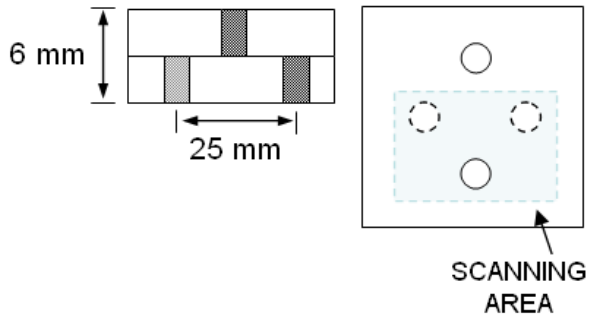

Figure 3.15: *The specimen is a pair of aluminium alloy plates* $200 \times 200 \times 3\ mm^3$ *in dimensions. There are two defects on the top plate and two hidden defects on the bottom plate. The scanning area reported in the magnetic maps in figure 3.16 is shown in blue color.*

defects under the top plate became larger. Finally, incrementing the phase angle to $\phi = 135^o$, they become smaller again. The two hidden defects, both 4.5 mm in diameter, were detected with high resolution, even though their distance from the sensor is more than 5 mm.

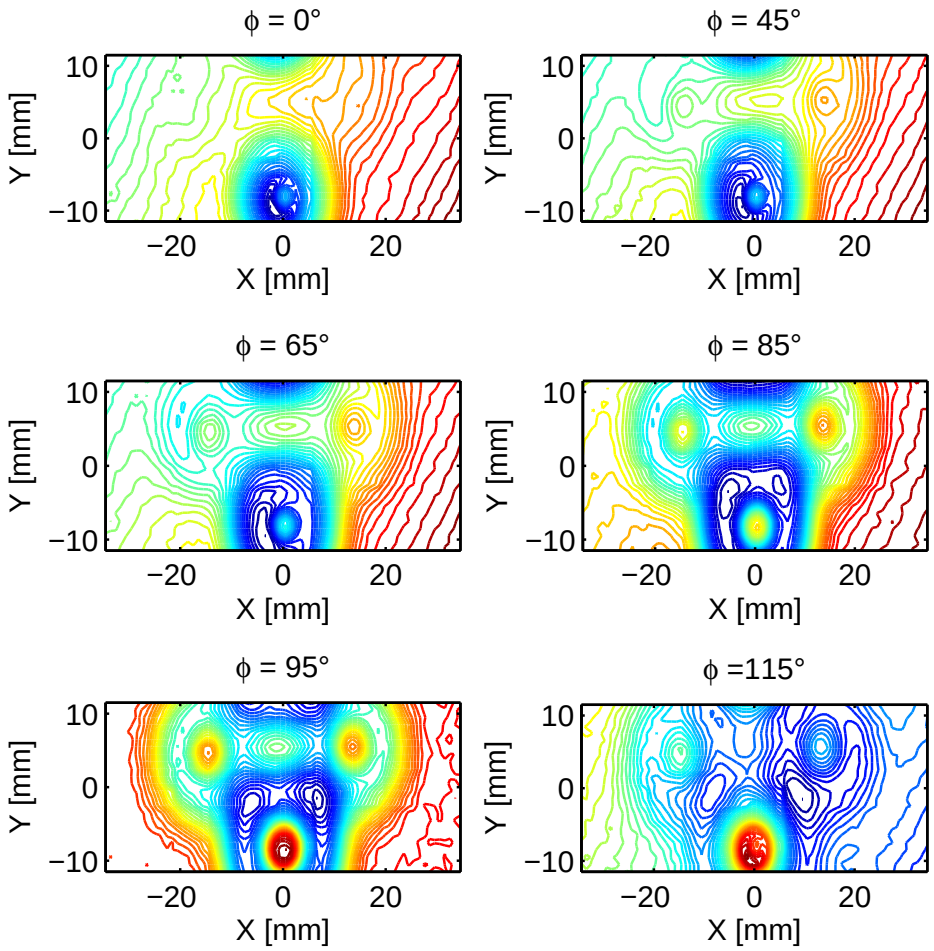

Figure 3.16: *The phase angle rotation analysis in the excited magnetic field applied to a specimen, constituted by two piled up aluminium alloy plates with two defects on the surface and two defects under the surface, respectively, as shown in the sketch in figure 3.15. At $\phi = 0^o$, only the defect on the top plate is evident; $\phi = 45^o$ the signal due to the hidden defects becomes more evident until $\phi = 95^o$, where it shows the largest increment since the lift-off effect is completely removed; $\phi = 135^o$ the signal reverses the polarity.*

3.4.3 Crack Detection in Structures for Aeronautical Applications

Usage of new materials and technologies in modern aircraft design allows reaching high long-time quality and efficiency but also requires the application of qualified inspection techniques during the whole aircraft lifetime. The inspection of new materials with stronger requirements becomes possible using new technologies of non-destructive testing.

The most frequently used inspection techniques for metallic components of aircrafts are ultrasonic testing (UT) and eddy current testing (ECT). For metallic structures ECT is the preferred technique for the detection of surface-breaking flaws as well as for hidden flaws in regions with specific geometry (e.g. joints, respectively riveted lap joints) as well as in areas which are difficult to access with UT. The higher inspection depths are only possible at low ECT frequencies because of the electromagnetic skin effect. Therefore the standard testing method for lap joints in part of fuselage and wings is eddy current testing.

However, since the thickness of the aircraft aluminium alloy is relatively large, in general > 3 cm, very low excitation frequencies must be chosen for sufficient deep penetration of the eddy currents (skin effect). To account for the decreased field sensitivity at low frequencies of induction coils, commonly used in conventional ECT systems, the SQUID system provides the best solution for deep defects. In addition, its high field sensitivity at low frequencies enhances the probability of crack detection when small field variations are superimposed by large stray field variations of bolts and edges.

Detection of hidden fatigue cracks in riveted aircraft structures as shown in figure 3.17 is a known challenge. Aircraft structures (wings, panels, etc.) often show hidden cracks close to rivets as a consequence of thermal and mechanical stress. Since the specific geometry (rivet holes, etc.) produces strong eddy current signals, they should be separated as much as possible from defect indications. An enhanced inspection effort is usually required and the result can be obtained just after a single scan with the sensor along the rivet row [83, 121].

To simulate this complex structure we used three-layer aluminium-titanium alloy

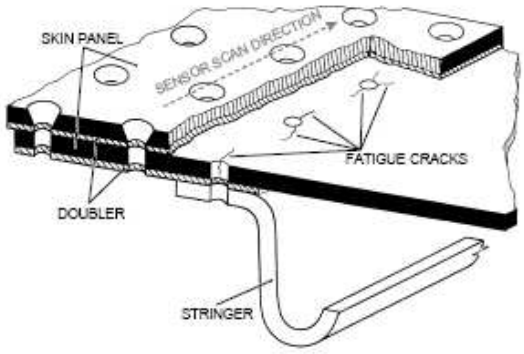

Figure 3.17: *Longitudinal lap joint with fatigue cracks in an aircraft skin panel (typical example) as reported in [121]. The layers are bolted together by means of titanium bolts.*

plates, in which slits with length l have been introduced adjacent to the rivet at two different depths of 3 mm ("upper" defect) and 6 mm ("lower" defect), respectively. The sketch of this configuration is shown figure 3.18. During the measurements we used two different excitation frequencies generated by a circular coil located below the cryostat and centered with the sensor. The highest is used to provide depth selective information about the upper defect; the lowest is used to localize the deeper defect.

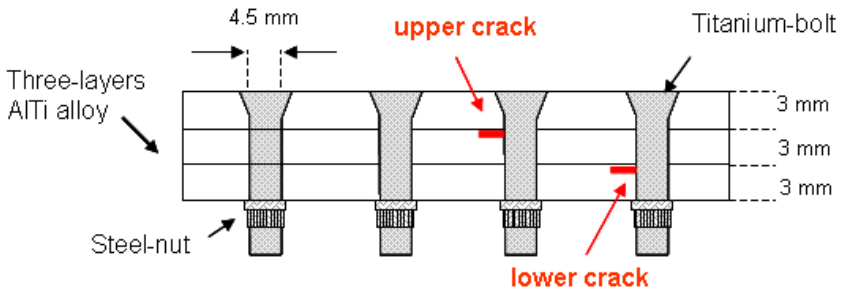

Figure 3.18: *Sketch of a simulated wing splice. In the three-layer aluminium titanium alloy (AlTi) sample, the slots are positioned adjacent to the rivet in two different depths of 3 mm ("upper" defect) and 6 mm ("lower" defect), respectively.*

When the coil scans over the plates, the in-phase and out-of-phase SQUID readout at the excitation frequencies are recorded as a function of X-Y positions. The stand-off distance, the spacing between SQUID and top sample, was chosen to be more than 2 mm.

The figure 3.19 shows field map distribution above the first sample configuration, three aluminium plates with simulated fatigue crack close to the rivet in the second layer. The excitation coil, aligned perpendicular to the z-axis, is fed sinusoidally with an excitation frequency of 889 Hz and an amplitude of 400 mV.

We perform the phase rotation analysis for six different values of phase angles: $\phi = 0^o$, 65^o, 75^o, 83^o, 97^o, and 125^o. The bolt and crack signals are best enhanced for a phase angle $\phi = 83^o$, due to a reduction of the lift-off effect. For this angle value, it is evident the different current distortion around the bolt caused by the simulated fatigue crack. However, the bolt signals are enhanced as the defect, thus having equal phase shift. Nevertheless, the defect with a length of 4 mm and a width of 100 μm located to a depth larger than 5 mm, has been detected applying this technique.

Finally, the figure 3.20 shows the magnetic field map distribution above the second sample configuration, three aluminium plates with simulated fatigue cracks close to the rivet in the third layer. In this case, to enhance the density of eddy currents in the bottom plate, we decreased the excitation frequency at 421 Hz and increased the voltage amplitude to 2 V. From the experimental results, it is absolutely clear that the crack was well detected applying the phase angle rotation analysis, even though we doubled the distance between the lower defect and the sensor, that in the present case is of order of 8 mm. The enhancement of the signal obtained at $\phi = 53^o$ was broader than the signals collected in the previous case, due to the increment of the stand-off distance and the slower variation of signals that now are close to the noise system limit. However, it is still evident the current distortion around the bolt caused by the simulated fatigue crack.

In conclusion, with this examples we have demonstrated how to performe eddy current NDT with our scanning SQUID microscope. In addition, we have demonstrated the validity of the *phase rotation method* used as depth-selective analysis of cracks in structures of aeronautical interest. Superior system performance may be obtained by increasing the dynamic range of the SQUID [98]. This requires an additional feedback coil inductively coupled to the input SQUID coil. Nulling the SQUID signal is advantageous because the passive field minimization procedure described above does not guarantee perfect signal cancellation. Then, the SQUID response to the the unflawed sample can be minimized by adjusting the current fed to the feedback coil.

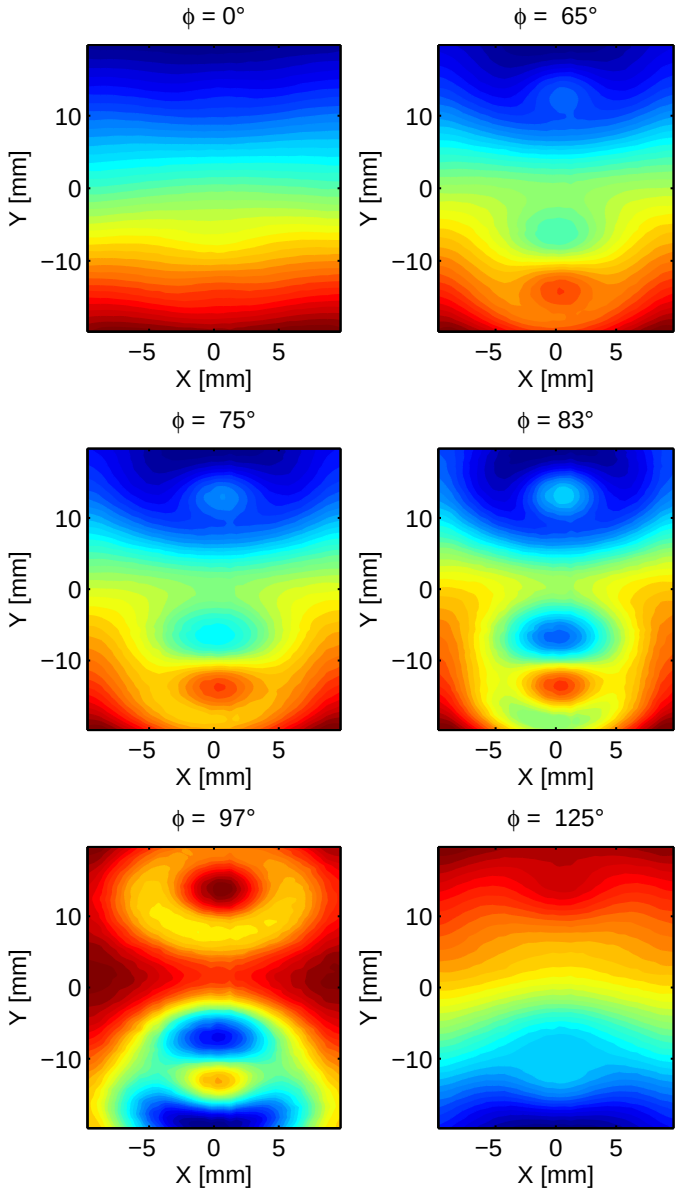

Figure 3.19: *The phase angles rotation analysis in the excited magnetic field applied to a specimen, three aluminium alloy plates with a simulated fatigue crack close to the rivet in the second plate. At $\phi = 0^o$, the component of the signal in phase with the exciting field does not give information about the presence of buried defects; by incrementing the values of the phase angle, we observe that for $\phi = 83^o$ the signal due to the hidden defects has the largest increment since the lift-off effect is completely eliminated. At $\phi = 125^o$ the signal inverts its polarity.*

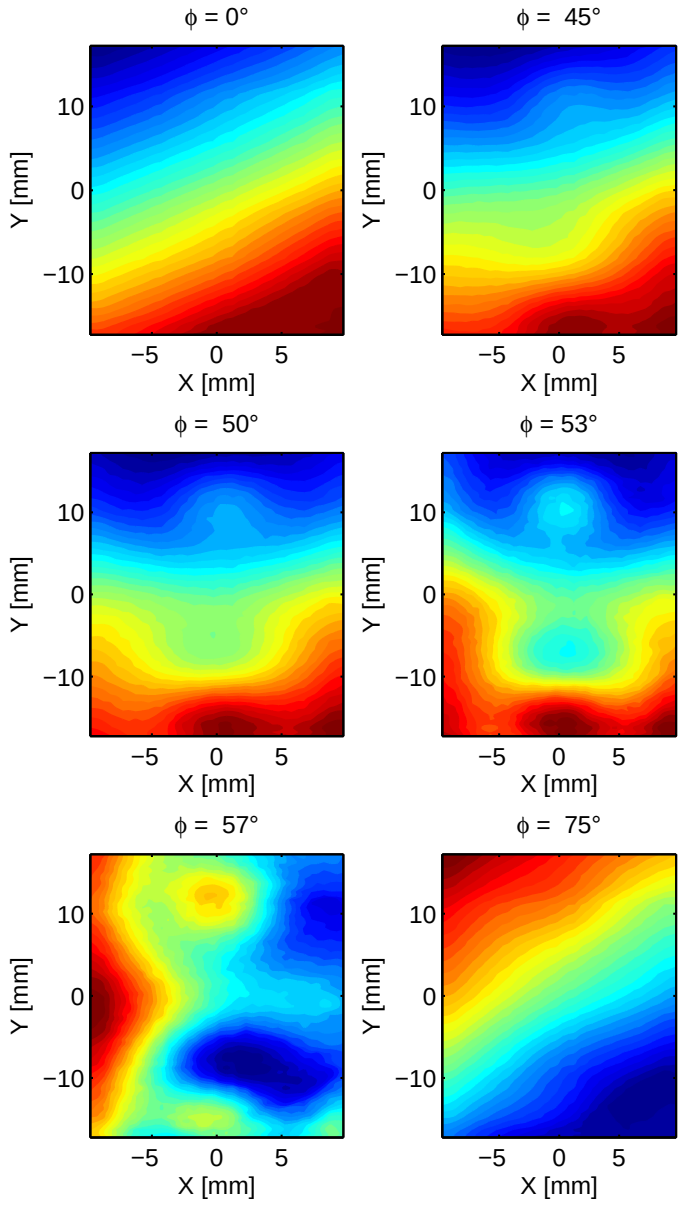

Figure 3.20: *The phase angle rotation analysis in the excited magnetic field applied to a specimen, three aluminium alloy plates with a simulated fatigue crack close to the rivet in the third plate. At $\phi = 0^o$, the component of the signal in phase with the exciting field does not give information about the presence of hidden defects; by increasing the values of the phase angle, we observe that for $\phi = 53^o$ the signal due to the hidden defects has the largest increase since the lift-off effect is completely removed. At $\phi = 75^o$ the signal reverses its polarity.*

Chapter 4

Scanning SQUID Microscopy: DC Technique

NDE DC technique based on high-T_c scanning SQUID microscope with samples at room temperature is a promising technique that we propose to apply in new fields of interest. Using the DC technique, magnetic field distribution produced by remanent magnetization or induced magnetization of ferromagnetic sample can be visualized. The worst limitation of a SSM is the limited spatial resolution for the analysis of objects at room-temperature. On the contrary, the main advantage is a direct measure of magnetic macro-domain structure and the capability to extract quite easily information on their orientation and magnetization.

In the first section, an important aspect such as the *visualization of the magnetic moment* of ferromagnetic particles, is focused on taking into account the quantitative analysis of the data. We introduce a model for magnetic data interpretation, starting from the analytical expression of "point magnetic dipole", and show the necessity to developed a new theoretical approach, describing the magnetic sources in terms of magnetic moment of "extended" dipoles. Theoretical aspects are illustrated and

confirmed experimentally by measuring magnetic dipole samples.

The second section is entirely dedicated to the understanding of the *detection of magnetic dipole domains* in different fields. For example, the imaging of magnetic particles on *magnetic data storage* is reported as a function of an external applied magnetic field. On the other hand, we propose to apply this non destructive technique in archeometry, it may be used to date *ancient mural paintings* on the base of magnetization direction of the magnetic components.

In the last section, it has been exploited the system capability and advantages of Scanning SQUID Microscope for the detection of crack initialization in structural stainless steel objects. It has been implemented by monitoring the residual magnetization above the surface, as a consequence of mechanical stress or fatigue cycles. Dislocation movements and magnetic filed distributions in proximity of the crack have been well detected. The series of experimental results are really novel in this field due to the high performances of our system.

4.1 Magnetic dipoles detection

in this paragraph we introduce the model for magnetic data starting from the expression of the vector potential of "point magnetic dipole". We emphasize the fact that real samples are represented by a collection of magnetic dipoles and show how SSM images can be nicely reproduced if magnetic dipoles are distributed appropriately. The analysis serves as a reference for samples of more complex unknown structures and to determine characteristics of magnetic material, such as magnetization.

In the first example shown in figure 4.1, two different magnetic dipole orientations have been considered. In fig. 4.1 (a) and (b), the magnetic dipole moment of the magnetic particle was oriented parallel to the x-axis; in the second case, fig. 4.1 (c) and (d), the magnetic moment was oriented vertically along the z-axis.

The quantitative analysis of the scanned data can be performed on the basis of the magnetic field distribution $\mathbf{B}$ [T] generated by the magnetic dipole $\vec{m}$ that is directly correlated to the vector potential $\mathbf{A}$ by the relation $\mathbf{B} = \nabla \times \mathbf{A}$. The vector potential $\mathbf{A}(\vec{r})$ at position $\vec{r}$(x, y, z) due to the magnetic moment $\vec{m}$ is

$$\mathbf{A} = \frac{\mu_0}{4\pi} \frac{\vec{m} \times \vec{r}}{\vec{r}^3} \tag{4.1.1}$$

where $\mu_0 = 4\pi \times 10^{-7} Hm^{-1}$ is the vacuum permeability, $\vec{m}$ $[Am^2]$ is the magnetic moment of the dipole, and $\vec{r}$ is the distance from the dipole to the measurement point. In general, it is possible to calculate the components of the magnetic field generated

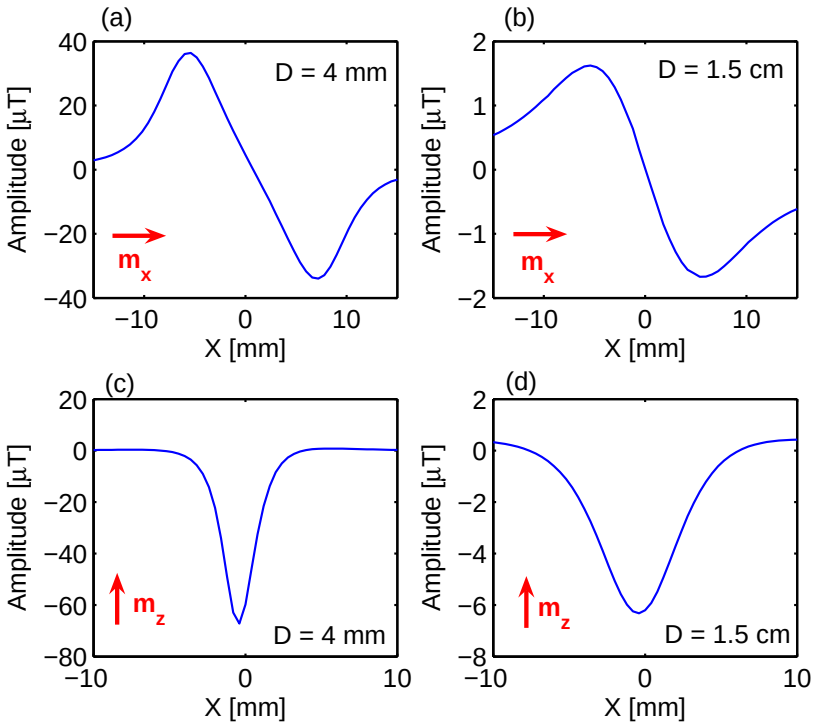

Figure 4.1: *Examples of the measurement when the magnetic moment of the particle is (a) parallel to the x-axis and (c) parallel to the z-axis. The effect of the increment of sensor-to-sample distance for particle (b) parallel to the x-axis and (d) parallel to the z-axis.*

by a magnetic moment $\vec{m}$ at a generic point $\vec{r}$ (x, y, z) in the space. Since our magnetometer is oriented along the z-axis and it is placed in the XY-plane at height h, we are interested to calculate the magnetic field component parallel to the z-axis, B_z(x, y, h).

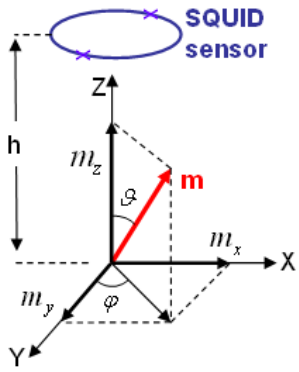

Figure 4.2: *Schematic representation of the three components m_x, m_y and m_z of a magnetic moment $\vec{m}$ arbitrarily oriented in the space.*

In figure 4.2, we consider the SQUID sensor at a distance h above a point magnetic dipole of moment $\vec{m}$, located at the origin of the cartesian coordinate system. The magnetic moment $\vec{m}$ can be expressed as the sum of the three components on the axes

$$\begin{aligned} m_x &= m\cos\varphi\sin\vartheta \\ m_y &= m\sin\varphi\sin\vartheta \\ m_z &= m\cos\vartheta \end{aligned} \tag{4.1.2}$$

where ϑ is the angle between the magnetic moment $\vec{m}$ and the z-axis, and φ is the angle of the vector projection between the y-axis and the XY plane.

As a matter of fact, the scan data curve shown in figure 4.1 (a), with the magnetic moment parallel to x-axis, can be described by the following equation:

$$B_{z,x}(x,y,z) = \frac{\mu_0}{4\pi} 3m_x \frac{xz}{(x^2+y^2+z^2)^{5/2}} \tag{4.1.3}$$

and, if the the magnetic moment is parallel to the y-axis, the equation becomes

$$B_{z,y}(x,y,z) = \frac{\mu_0}{4\pi} 3m_y \frac{yz}{(x^2+y^2+z^2)^{5/2}} \tag{4.1.4}$$

When the scan data curve with the magnetic dipole parallel to z-axis (fig. 4.1 (c)) can be described by the equation

$$B_{z,z}(x,y,z) = \frac{\mu_0}{4\pi} m_z \frac{(3z^2-(x^2+y^2+z^2))}{(x^2+y^2+z^2)^{5/2}} \tag{4.1.5}$$

Finally, for a sensor to sample distance h and a magnetic dipole arbitrarily oriented in the space, the magnetic field measured by the SQUID sensor is equal to the sum of the three components $B_{z,i}$, with $i = x, y, z$:

$$B_z(x,y,h) = B_{z,x}(x,y,h) + B_{z,y}(x,y,h) + B_{z,z}(x,y,h) \tag{4.1.6}$$

By the light of this considerations, the scanning SQUID microscope system can be applied to determine the distribution of magnetic particles in the sample. This can be done in principle by recording the 2D magnetic dipole distribution maps followed by a computer deconvolution of the inverse dipole problem. In figure 4.3, the magnetic

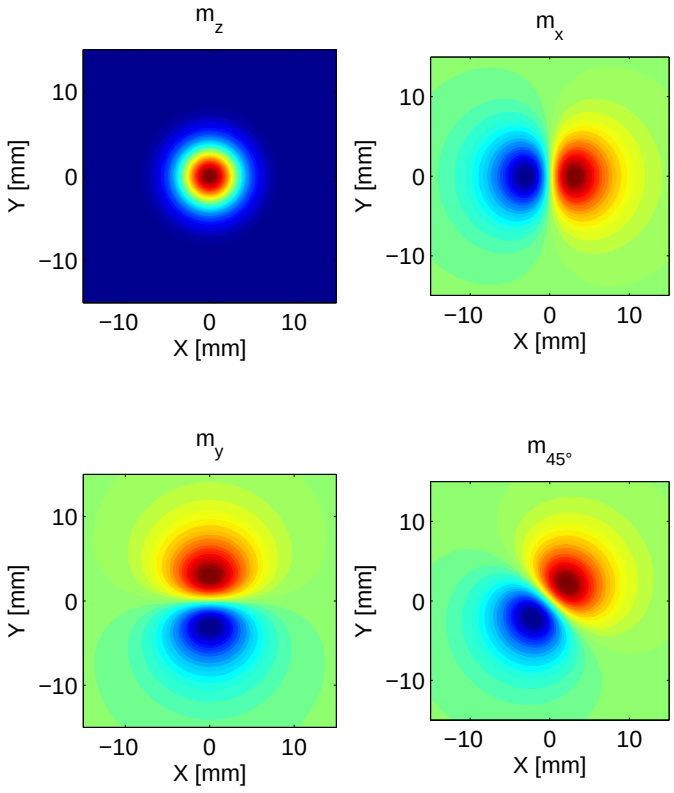

Figure 4.3: *2D magnetic maps simulating magnetic field distributions for different relative orientations of the sensor and magnetic moment $\vec{m}$ of the dipole: (a) $\vec{m}$ is parallel to z, (b) $\vec{m}$ is parallel to x, (c) $\vec{m}$ is parallel to y and (d) $\vec{m}$ is oriented at 45^o between the x and y axis.*

2D maps of different relative orientations of the magnetic moment with respect to the sensor orientation have been simulated using the eqs. 4.1.3-4.1.5: (a) $\vec{m}$ is parallel to z, (b) $\vec{m}$ is parallel to x, (c) $\vec{m}$ is parallel to y and (d) $\vec{m}$ is oriented at 45^o between the x and y axes.

In addition, the azimuthal angle ϑ of the magnetic moment $\vec{m}$ may vary arbitrarily with respect to the z-axis and the dipole will be out-of-XY plane. This other situation is represented in figure 4.4, where 2D magnetic images of the magnetic moment $\vec{m}$ oriented at $\varphi = 45^o$ between the x and y axes have been obtained varying the ϑ angle from 90^o to 0^o. Six different configurations are reported: $\vartheta = 90^o$, corresponding to the case in which $\vec{m}$ is placed in the XY plane and the positive and negative peaks are symmetric; decreasing ϑ from 60^o to 30^o, $\vec{m}$ is moving out-of-XY plane and the positive peak is more intensive than the negative peak; $\vartheta = 0^o$, where $\vec{m}$ is parallel to the z-axis and finally, $\vartheta = -45^o$, in which $\vec{m}$ inverts its polarity. This example shows how the magnetic source visualization can vary as a function of its slight inclination (few degrees) with respect to the sensor plane. For this reasons, the interpretations of experimental data could be not trivial and in some uncertain cases, it could be necessary to use additional scans with different sensor orientations for a unique problem solution.

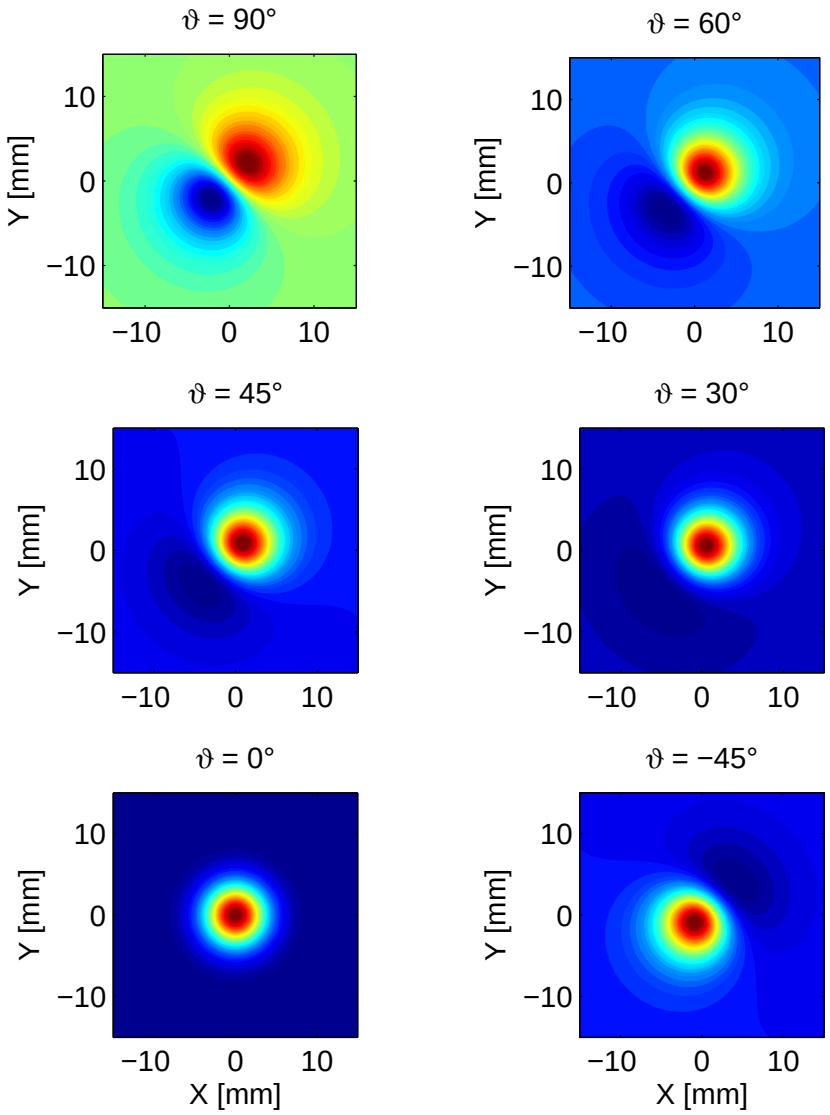

Figure 4.4: *2D magnetic maps simulating magnetic field distributions for different relative orientations of the SQUID and magnetic moment $\vec{m}$ of a single dipole when the angle φ is 45^o and the angle ϑ varies from 90^o to 0^o. (a) $\vartheta = 90^o$, $\vec{m}$ is placed in the XY plane as shown by the symmetrical poles; from (b) to (d), ϑ varies from 60^o to 30^o, $\vec{m}$ is moving out-of-XY plane as shown by the asymmetrical poles; (e) $\vartheta = 0^o$, $\vec{m}$ is parallel to the z-axis; (f) $\vartheta = -45^o$, $\vec{m}$ inverts its polarity.*

4.1.1 Imaging resolution and magnetic source sensitivity

As defined by Wikswo [120] and shown in figure 4.5, the *imaging resolution* is the ability to discriminate between two closely spaced sources, such as a pair of magnetic dipoles and a single source with the total strength equal to the sum of the single dipoles.

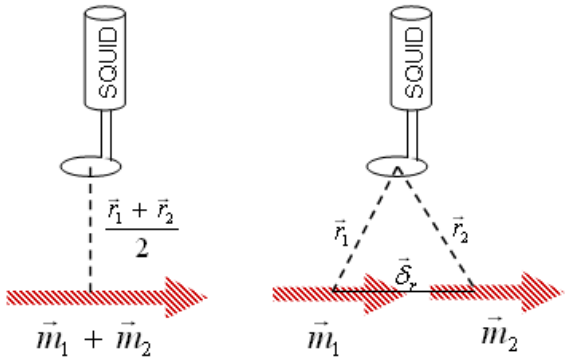

Figure 4.5: *Imaging resolution as reported in [120]: the ability of a magnetometer to distinguish between one single source and a pair of closely spaced sources with the same total strength.*

Using a point moment approximation, we can derive the analytical expressions to estimate both the smallest detectable magnetic moment m^{min} and the imaging resolution δ of our microscope. To this aim, we consider as a source a point magnetic dipole $\vec{m}$ oriented along the z-axis ($m_x = m_y = 0$), a SQUID pick-up coil radius r_s = 35 μm (congruously with our sensor) and assume that the magnetic flux through the SQUID sensor Φ_{c0} is of the order of $\sqrt{S_\Phi \Delta f}$, where S_Φ is the flux noise spectral density of the system and Δf the bandwidth of data acquisition. The estimated SSM flux noise is $S_\Phi^{1/2} = 50 \times 10^{-6} \Phi_0 / Hz^{1/2}$, so that we calculate the minimum magnetic

moment we can detect by the relation, as reported in [117],

$$m^{min} = \frac{2(h^2 + r_s^2)^{3/2}\sqrt{S_\Phi \Delta f}}{\mu_0 r_s^2} \tag{4.1.7}$$

Choosing a sensor-to-source distance h = 200 μm and a bandwidth of 10 Hz, we obtain the minimum detectable magnetic moment $m^{min} = 3.5 \times 10^{-15} Am^2$.

For small displacement $\delta \ll (r_s, h)$, we find an analytical solution for the spatial resolution δ of a circular loop SQUID sensor as a function of the geometrical parameters r_s and h, (see [2]):

$$\delta = \{\frac{(S_\Phi \Delta f)^{1/2}}{\mu_0 m G(r_s, h)}\}^{1/2} \tag{4.1.8}$$

where $G(r_s, h)$ is a geometrical factor. Using the previous values for r_s and h, we estimate an image resolution $\delta \simeq 120\ \mu m$, for the case corresponding to the minimum detectable magnetic moment.

As a consequence, if the size of the particle is much smaller than the distance between the particle and the SQUID sensor, the model of localized point magnetic dipole can be applied for particle data analysis. As an example, figure 4.6 shows the 2D magnetic images generated by a point magnetic dipole oriented along the y-axis ($m_x = m_z = 0$), simulated by using equation 4.1.4. The dipole strength is chosen as $m_y = 10^{-6} Am^2$, providing a magnetic field value in the range $0.05 - 50\ \mu T$, at four different h values: $h_1 = 1$ mm, $h_2 = 2$ mm, $h_3 = 5$ mm and $h_4 = 10$ mm. When h

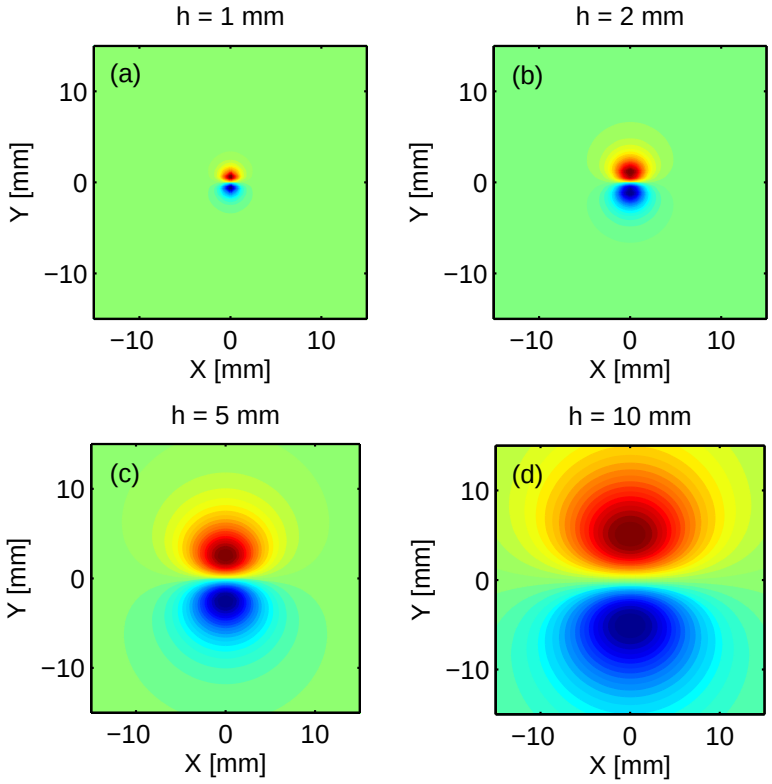

Figure 4.6: *Simulated 2D magnetic distribution maps of a point dipole positioned in the XY plane and oriented along the y-axis. The maps are obtained for four different sensor-to-source distances: (a) $h_1 = 1$ mm, (b) $h_2 = 2$ mm, (c) $h_3 = 5$ mm, and (d) $h_4 = 10$ mm.*

decreases, we may observe a corresponding reduction of the axial distance between the positive and negative poles representing the magnetic moment strength. This is a direct consequence of dimensionless point moment model.

On the other hand, since the SSM spatial resolution is evaluated to be $\delta \approx 70$ μm, the point magnetic dipole approximation becomes an unrealistic attainable limit, except for very large h values or very small magnetic sources. Indeed, the comparison between experimental and simulated magnetic dipole shown in figure 4.7 demonstrate that a different approach is needed to reproduce the magnetic field distribution of real extended magnetic sources with dimensions larger than the SSM spatial resolution. As shown in this case, where the source is a ferromagnetic rod specimen 10 mm long, if the sensor-to-source distance is longer than the source dimension ($h = 16$ mm), the point magnetic model fits pretty good the results (compare (b) and (d) in figure 4.7), while if the source dimension is comparable or less than the sensor-to-source distance ($h = 5$ mm), the point magnetic dipole does not work well (compare (a) and (c) in figure 4.7).

Consequently, in the next section we derive a simple theoretical approach which allows the description and simulation of extended magnetic dipoles to be applied in the case of 1D ferromagnetic particle of finite dimensions.

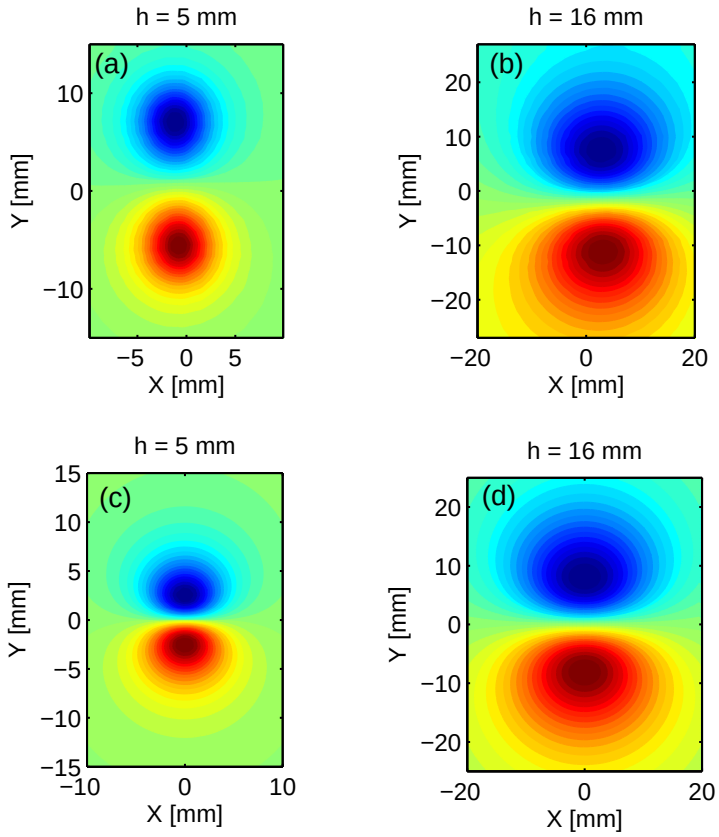

Figure 4.7: *Comparison between experimental (a-b) and simulated (c-d) 2D magnetic image distribution of a magnetic source positioned in the XY plane and oriented along the y-axis. The experimental source is a 1D ferromagnetic rod specimen 10 mm long. The maps are obtained by solving the equation 4.1.4 for two different sensor-to-source distances: (a) $h_1 = 5$ mm and (b) $h_2 = 16$ mm. The amplitude of the magnetic field ranges between $2 and 30$ μT peak-to-peak, depending on the distance.*

4.1.2 Extended magnetic dipole approximation

As said before, if the magnetic source dimension is comparable with the image resolution δ of our system, its signal cannot be simulated in the framework of the point magnetic moment approximation. For this reason, it is useful to introduce a finite length magnetic dipole approximation, that we call the *multi-dipole* (MD) model.

The idea is to consider an extended dipole as made of N aligned point magnetic dipoles spaced $\Delta c \approx \delta$, which constitutes a single 1D macro-domain. The magnetic field of an extended dipole of length L will be the sum of the magnetic fields of N single point magnetic dipoles of length $L = N\Delta c$. More details about the development of this model and different kinds of magnetic dipole configurations are treated by Adamo et al. in [2].

Thus, the magnetic field components $B_{z,i}$ generated by an extend magnetic dipole can be still expressed as a function of the magnetic moment components m_x, m_y and m_z, as reported in [2] and summarized in the following equations:

$$B_{z,x} = \frac{\mu_0}{4\pi} 3 m_x z \sum_{i=1}^{N} \frac{(x - \Delta c_{ix})}{[(x - \Delta c_{ix})^2 + (y - \Delta c_{iy})^2 + (z - \Delta c_{iz})^2]^{5/2}} \tag{4.1.9}$$

$$B_{z,y} = \frac{\mu_0}{4\pi} 3 m_y z \sum_{i=1}^{N} \frac{(y - \Delta c_{iy})}{[(x - \Delta c_{ix})^2 + (y - \Delta c_{iy})^2 + (z - \Delta c_{iz})^2]^{5/2}} \tag{4.1.10}$$

$$B_{z,z} = \frac{\mu_0}{4\pi} m_z \sum_{i=1}^{N} \frac{3z^2 - [(x-\Delta c_{ix})^2 + (y-\Delta c_{iy})^2 + (z-\Delta c_{iz})^2]}{[(x-\Delta c_{ix})^2 + (y-\Delta c_{iy})^2 + (z-\Delta c_{iz})^2]^{5/2}} \tag{4.1.11}$$

where Δc_{ix}, Δc_{iy} and Δc_{iz} are the projections of the point magnetic dipole displacement Δc on x, y and z-axis, respectively.

The first important consequence obtained introducing the MD model, is that it is possible to fit the data for a magnetic dipole with finite dimensions comparable or larger than the spatial resolution of the system. As an example in figure 4.8, we consider again the case of 1D magnetic dipole source of length L = 10 mm, laying in the XY plane and parallel to the y-axis (see figure 4.8 (a) and (b)). Using the eq 4.1.10 and choosing N = 110 point magnetic dipoles with strength $m_y = 10^{-6} Am^2$ spaced of $\Delta c = 100\ \mu m$, we computed the responses at two different distances, $h_1 =$ 5 mm and $h_2 = 16$ mm (see figure 4.8 (c) and (d), respectively). As shown in this example, using the MD model, there is an excellent quantitative agreement between experimental and simulated data, either in the case in which the sensor-to-source distance is larger than the dimension of the magnetic particle (figure 4.8 (b) and (d)), or when tit is less than the magnetic particle dimension (figure 4.8 (a) and (c)).

Moreover, in the next section, we want to stress the attention to the fact that the MD model is valid either when the dimension of single dipole is smaller than the system image resolution δ, or in the opposite limit, when the sensor-to-sample distance h is comparable or less than the dimension of a single magnetic particle. This concept will be more clear when we apply the MD model to a magnetic sources

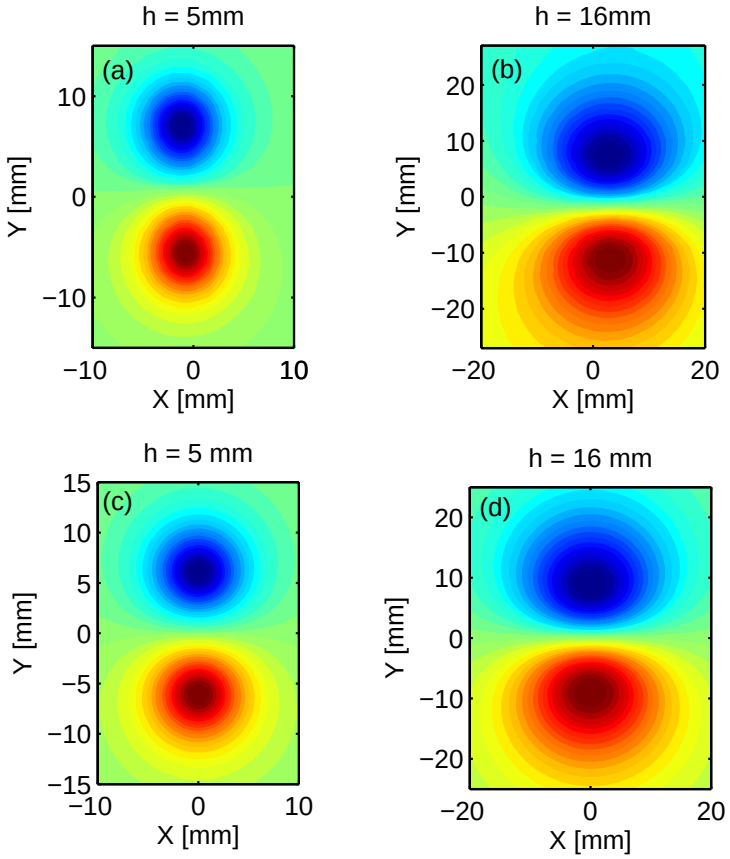

Figure 4.8: *Comparison between experimental (a-b) and simulated (c-d) 2D magnetic source distribution using the MD model. A magnetic source 10 mm long is positioned in the XY plane and oriented along the y-axis. The parameters used for the simulations are: $N = 110$ point magnetic dipoles, each with strength $m_y = 10^{-6} Am^2$, spaced by $\Delta c = 100\ \mu m$. The responses are computed at two different distances, $h_1 = 5$ mm and $h_2 = 16$ mm. The amplitude of the magnetic field ranges between 2 and 30 μT peak-to-peak, depending on the distance.*

composed of multiple dipoles randomly oriented in the space.

4.1.3 Extended model for two magnetic sources

We describe the MD model for the detection of two different magnetic particles positioned in the XY plane. In particular, the two experimental particles are both 4 mm long: the magnetic source $\vec{m}_1$ is oriented along the y-axis and $\vec{m}_2$ forms an angle of 45^o between the x and y-axis, as shown in the sketch of figure 4.9.

We performed two kinds of measurement. In the first case, the magnetic field distribution B_z, above the two magnetic sources $\vec{m}_1$ and $\vec{m}_2$, is obtained at the height $h = 1.5$ mm, smaller than the length of the single 1D magnetic particle. The two sources, both 4 mm long, are well detected and their magnetic field distributions do not affect considerably each other, as shown in figure 4.9 (a). In the second case, the magnetic field distribution B_z is obtained at the height $h = 5$ mm, larger than the single dipole length, thus the magnetic signatures overlap and the imaging resolution gets worse. As it is evident, this time we cannot distinguish the two different magnetic sources (figure 4.9 (b)). We have also made measurements for the same different heights when the polarity of $\vec{m}_2$ source is inverted, as shown in figure 4.9 (c) and (d), for $h = 1.5$ mm and $h = 5$ mm, respectively.

Using the MD model and choosing as fitting parameters N = 10 point magnetic dipoles spaced by $\Delta c = 400$ μm, we computed the responses at two different distances, $h_1 = 1.5$ mm and $h_2 = 5$ mm obtaining a magnetic dipole strength for both

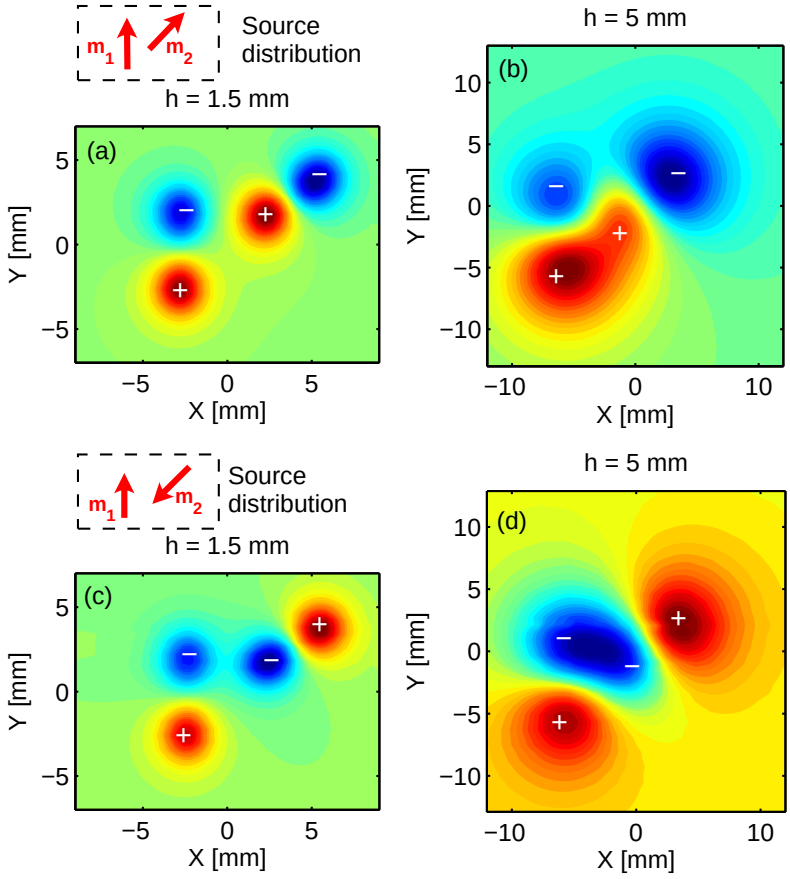

Figure 4.9: *Experimental 2D magnetic maps of two magnetic rods 4 mm long, positioned in the XY plane. The dipole $\vec{m}_1$ is oriented along the y-axis, while the dipole $\vec{m}_2$ forms an angle of 45^o between the x and y-axis. Two different configurations are measured, obtained by 180^o in-plane rotation of $\vec{m}_2$ at two different sensor-to-source distances: $h_1 = 1.5$ mm and $h_2 = 5$ mm. The amplitude of the magnetic field ranges between 5 - 60 μT peak-to-peak, depending on the distance.*

sources of order of $m \simeq 10^{-6} Am^2$. This value can be used to calculate the magnetization M [A-turn m^{-1}] of the sample, that is defined as the magnetic moment per unit volume: $M = N\mathrm{m}/V$. The estimate magnetization for the ferromagnetic rod particle specimens, of radius 400 μm and 4 mm long, is about $M \simeq 5\ kAturn\ m^{-1}$.

However, it is worth nothing that, even in the case of a single dipole, the interpretation of magnetic maps may need additional information. Using the MD model, the inverse problem for the magnetic moment could be solved, but additional scans with other sensor orientations are necessary for a unique solution of the problem.

4.2 Imaging magnetic domain structures

Since real samples under investigation often show a collection of extended magnetic dipoles with different orientations, we present in this section the measurements performed by SSM over different magnetic samples. Because of its extremely large sensitivity (few tens of $pT/Hz^{1/2}$), combined with a good spatial resolution (few tens of μm), the SSM is able to detect information contained in thin magnetic films or other type of magnetic objects.

Quite recently, *magnetic recording media* (computer storage, credit cards, etc.) is a large and growing field of use of magnetic materials. The trend is to require high-density magnetic recording systems. We report a two-dimensional magnetic image produced above a magnetic material surface that can be used to estimate the spatial variation of magnetization, which is of interest in magnetic recording materials [49].

In a totally different field, there is a particular interest in the *archeometry dating*, which widely used to acquire information of the physical data of an ancient find, comparing the "frozen" direction of magnetization within an archaeological feature with a time reference curve. Here we propose to apply this non-destructive technique, completely innovative in the archeological field, to find information on magnetization direction and, at the same time, as a form of authentication of artistic patrimony.

4.2.1 Imaging magnetic recording media

This experiment was performed to test the feasibility to use a scanning SQUID microscope from reading information from magnetic recording media, in this case a commercial floppy disk, and to estimate the value of magnetic signals.

The floppy disk presents a thin layer of Fe-Co based microparticles with size of about 1 μm. These magnetic particles have in-plane oriented magnetic moments. The coercivity value, the intensity of the applied magnetic field required to reduce the magnetization of such ferromagnetic materials to zero, is of about 30-70 kA m^{-1}. Such magnetic moments are initially in-plane randomly oriented. During the formatting process, the magnetic tracks are created and each magnetic moment orientation is equivalent to a "*zero*" state of data. During recording process, some magnetic moments are magnetized in the opposite direction, thus some magnetic pole orientations are equivalent to "*unit*".

The sample we measured was a fragment of a floppy disk with some recording data corresponded to text information. Figure 4.10 (above) shows the magnetic image of the fragment portion taken at the sensor-to-sample distance of about 100 μm. The intensity of the magnetic field distribution varies from about -3 μT (blue peaks) to +3 μT (red peaks). The minimum size of a single spot is about 200 μm, corresponding to the used step resolution. Thus, our imaging resolution makes impossible to resolve the single magnetic domain of recording media (one bit of information of order of few microns).

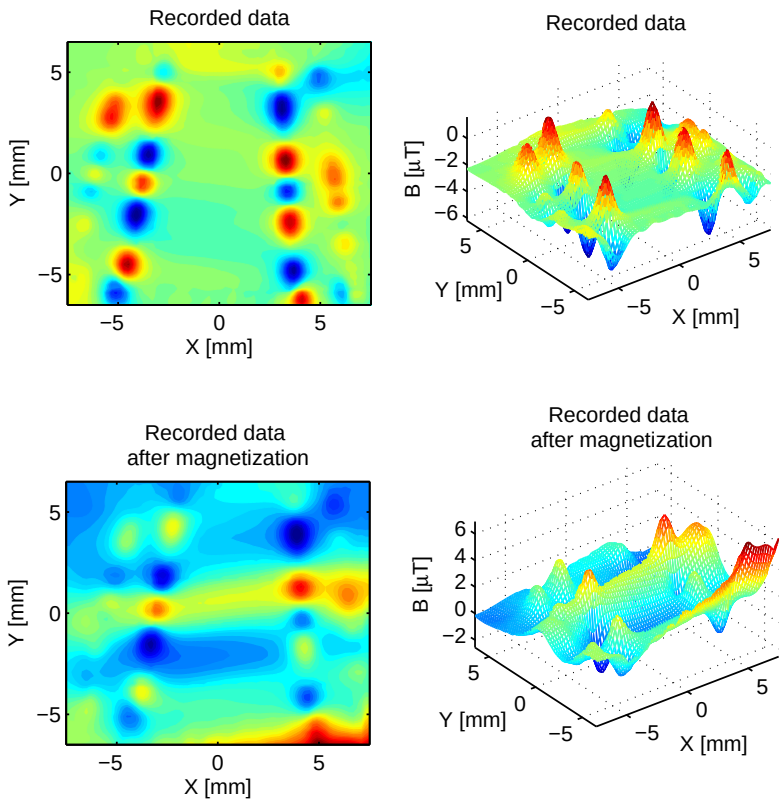

Figure 4.10: *Magnetic images of recorded data on a commercial floppy disk (above) and the effect of the distortion of some recorded data after magnetization of the sample (below). The amplitude of the magnetic field ranges between -3 to 3 μT peak-to-peak.*

Figure 4.10 (below) shows the magnetic image of the fragment portion taken at sensor-to-sample distance of about 100 μm when the sample was previously magnetized with a static magnetic field. The intensity of the magnetic field distribution still varies in the range of $\pm$ 3 μT, but the less intensive magnetic domains are destroyed. However, the effect of the pre-magnetization is that the periodic structure of the recorded information is modified with the consequent loss of data.

4.2.2 Imaging magnetic particles in ancient mural painting

In this section we give a quick look to the analysis of archaeological ruins. For sake of completeness, the archaeological activity based on magnetic techniques can be divided into two main categories:

Magnetic survey. It is based on geophysical prospecting which deals with iron minerals within the soils and sediments forming archaeological sites, that often provide a valuable record of past human activity. This technique represents an important aid for the location and interpretation of archaeological ruins. This aspect is obviously not of interest for the magnetic microscopy and so we do not treat it in this contest.

Archaeomagnetic dating. It is based on the measurement of magnetic properties from samples recovered during excavation. Naturally occurring processes of magnetization can result in the alignment of individual magnetic grains along the orientation of the earth magnetic field. Since this field has constantly changed direction during geological time scales, the determination of a "frozen" direction of magnetization can

provide information of physical data, when compared to a suitable reference curve.

In this section we want to focalize the attention on the measurement of surface magnetic dipole orientation as a consequence of the remanent magnetization of ancient paintings present on archaeological samples. The magnetic DC technique here proposed is absolutely innovative in this field and it could give a great aid who works with ancient specimen dating problems. For this reasons, the remanent magnetization of red and yellow color specimens from different mural paintings, coming from *Pompei archeological site, in Napoli (Italy)*, has been investigated using the DC technique. All specimens have a strong remanent magnetization carried on by iron oxides, probably *hematite*, as reported by Chiari and Lanza [23]. They demonstrated that a red colored mural painting, prepared using hematite as a pigment, acquires a remanent magnetization parallel to the earths field, thanks to the fact that the magnetic moment of the hematite grains orients itself as long as the color is fluid, and it maintains its orientation once the paint has dried.

As an evidence of all this discussion, in figure 4.11 is shown the magnetic measurements a yellow color mural painting specimen (picture in figure 4.11 (a)) taken at a sensor-to-sample distance of about 100 μm. It is evident the magnetic dipole domain structure on the surface of the sample (fig. 4.11 (b)) carried by a slow orientation of the iron oxides in the earth's magnetic field. The magnetic image reproduces faithfully the specimen contour and that has been obtained with a step size of 1 mm. Figure 4.11 (c) shows an area zooming (marked by the dashed box in (b)) on the center of the sample, obtained reducing the scan step size to 200 μm. The magnetic

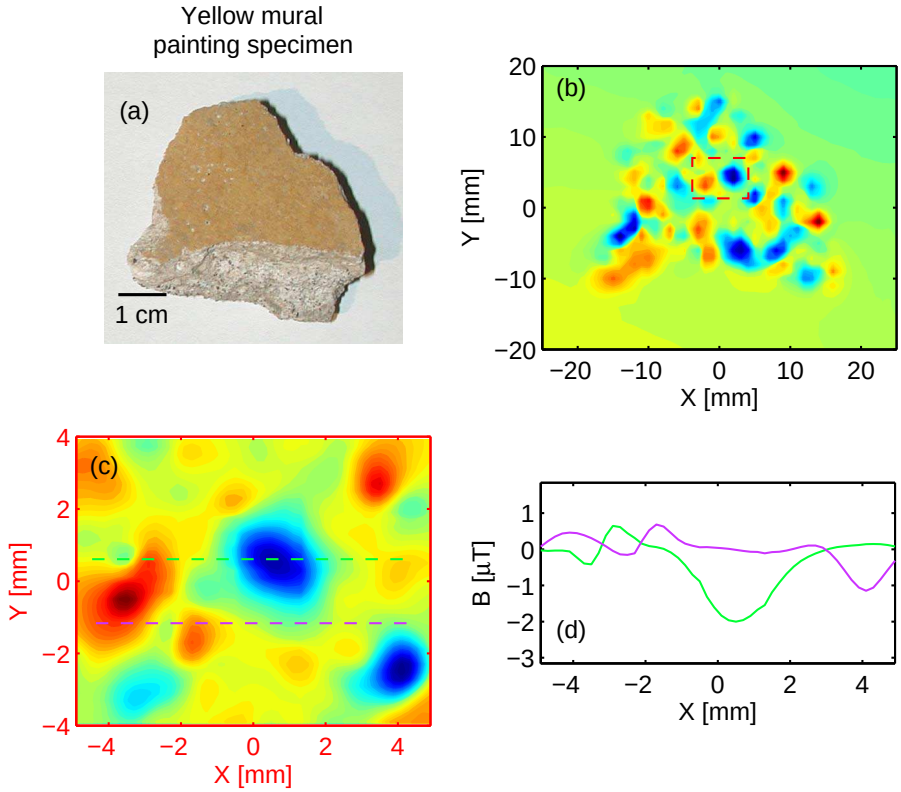

Figure 4.11: *Magnetic images of a yellow color mural painting specimen coming from Pompei archeological site (Italy) taken at a sensor-to-sample distance of about 100 µm. (a) picture of the specimen; (b) magnetic image of the sample with the evident surface magnetic dipole distribution as a consequence of iron oxides orientation in earth's magnetic field; (c) magnetic image zooming on the center of the sample, as marked by the dashed box in (b), using 200 µm scan step size; (d) two line scans of the magnetic field, as marked by the dashed lines in (c).*

field varies in the range of $\pm$ 2 μT peak-to-peak, as reported in figure 4.11 (d), where two line scans along the dashed lines in figure 4.11 (c) are reported.

The second red color mural painting specimen, shown in figure 4.12 (a), has similar characteristics. The magnetic image, taken at a sensor-to-sample distance of about 100 μm, still shows the magnetic dipole domain distribution on the surface of the sample (figure 4.12 (b)), as a consequence of the slow orientation of the iron oxides in the earth's magnetic field. The zooming images (figure 4.12 (c)) on a central area of the sample (marked by the dashed box in (b)) is obtained using 400 μm scan step size. The magnetic field variation is once again of $\pm$ 2 μT peak-to-peak as shown in figure 4.12 (d), where two line scans along the dashed lines in figure 4.12 (c) are reported.

Due to the quite recent development of the used DC technique, it is the first time that this kind of magnetic domain distribution is observed on ancient mural paintings whit ferromagnetic properties. Something similar has been made when some authors visualized magnetic images of rocks of geological interest.

In the following, we want to focus on another important aspect. Some colors, especially reds and yellows, used today for the conservation of artistic painting patrimony, are characterized by ferromagnetic properties due to iron oxide pigments. However, the patterns shown in figures 4.11 and 4.12 are typical of ancient finds and, in the future, they can probably be used for the identification of the authenticity of the ancient paintings and maybe to date a specific piece of art. From this point of view, non destructive forms of authentication is of great importance since it contributes to the preservation and conservation of artistic patrimony and even to prevent forgery.

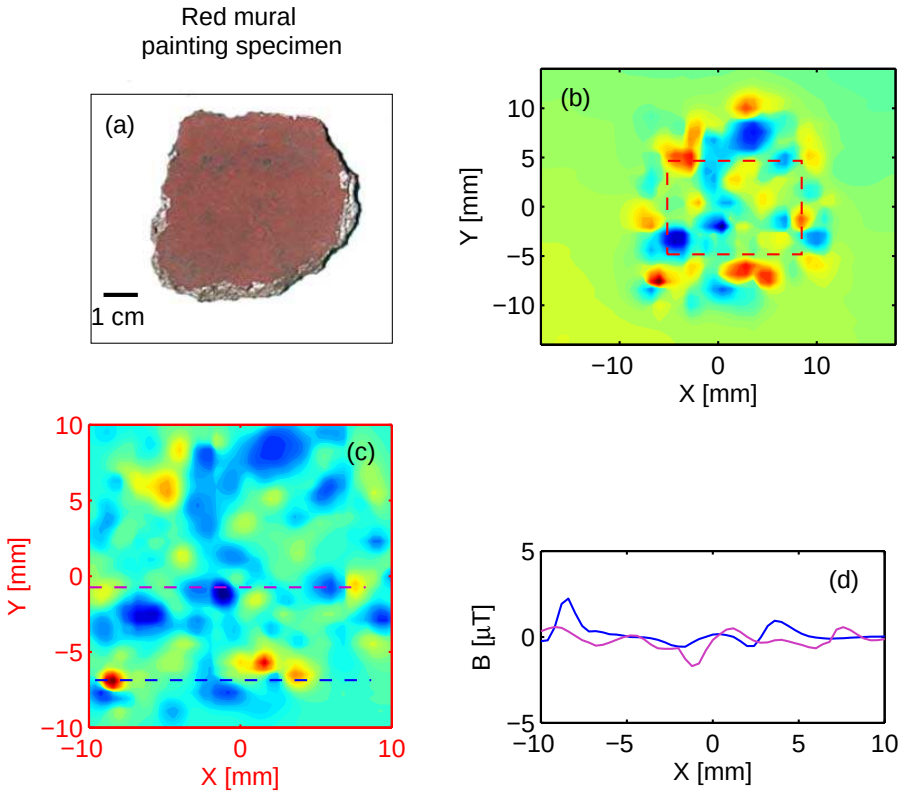

Figure 4.12: *Magnetic images of a red color mural painting specimen coming from Pompei archeological site (Italy), taken at a sensor-to-sample distance of about 100 µm. (a) picture of the specimen; (b) magnetic image of the sample, with the evident surface magnetic dipole distribution, as a consequence of ferromagnetic properties of iron oxide pigments; (c) magnetic image zooming on the center of the sample, as marked by the dashed box in (b), using 400 µm scan step size; (d) magnetic field along two line scans, as marked by the dashed lines in (c).*

4.3 Magnetic detection of mechanical degradation of steel

It is a considerable problem to estimate non destructively the degradation of mechanical property of metallic alloys, as a consequence of local plastic deformation due to fatigue cycles, especially crack formation as a precursor of failure. This kind of investigation may be used to examine ferromagnetic materials such as the steels used in nuclear pressure vessels, ship hulls and other critical structures to insure safety, as well as for on-line quality control in the manufacture of structures.

It is well known that plastic deformation of metals increases the density of dislocations within them. The increase in dislocation density hardens the material and the phenomenon is known as *strain-hardening*. The dislocation substructure evolves slowly and becomes increasingly heterogeneous, leading to the formation of the persistent slip band (*Lüders bands*) that will eventually nucleate cracks. They also interact with magnetic domain walls and, therefore, change the magnetization of the steel. The last stage of fatigue cycle is characterizes by the formation of the fatigue cracks and ends with final failure. Since fatigue cracks can propagate under loads that are small compared to those required to nucleate them, the time interval for crack detection between nucleation and catastrophic failure may be very short.

Therefore, since significant microstructural changes occur during the fatigue stages, researchers have had some success in developing NDE methods probing them. Magnetic methods are particularly promising for ferromagnetic materials such as structural steels. Parameters such as the saturation magnetization, coercivity, Barkhausen

noise and magnetic hysteresis change significantly during the initial and final stages of fatigue [90, 93]. Magneto-mechanical effect has been detected using a SQUID magnetometer, measuring changes in the magnetic hysteresis of metallic alloys and structural steel. Indeed, a magnetic field sensor with high field sensitivity and spatial resolution as the SSM is required to measure the low magnetic field signals characterizing dislocation motion. These properties are successfully satisfied by the SQUID microscope that has already been used in the detection of fatigue damage [118, 109, 87, 17].

In this section, the change of the pattern by a tensile deformation has been investigated in two different structural steel samples (Fe360), without applying any external magnetic field. The specimen configurations are shown in figure 4.13. In particular, the two different geometries are used to detect different effects: sample (1) is used to study the initiation and crack propagation on slot tip and sample (2) to detect the surface slip bands as a consequence of plastic deformation.

In the first subsection, a local tensile stress concentration on slot tip is visualized

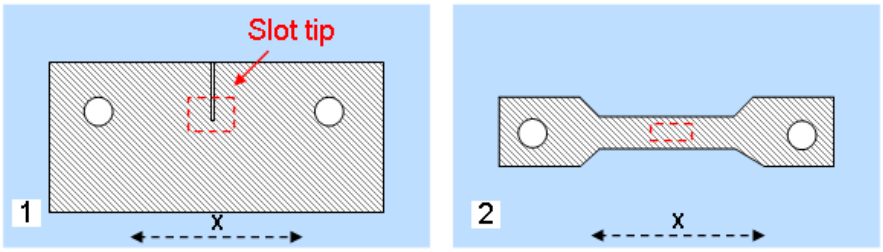

Figure 4.13: *Geometry of 5 mm thick structural steel (Fe360) specimens. Sample (1), with a slot 100 µm wide, is used to study the initiation and crack propagation on slot tip; sample (2) to detect the surface slip bands. A mono-axial tensile stress was applied along the x-direction and measured by the strain-gauges glued on both side of the samples. The dashed boxes indicate the inspected regions.*

before and after tensile stress cycles. The mechanical effect is correlated to the magnetic field gradient component dB_z/dx. The capability of the SSM to detect magnetic signals, produced by plastic deformation, has been demonstrated.
In the second subsection, Lüders bands, which are groups of slip bands, appearing on the plate surface after one tensile stress cycle, were observed at the corresponding locations of the stripes. This shows that fine deformation can nondestructively be detected using SSM.

4.3.1 Detection of fatigue crack in steel due to fatigue cycles

In the first example, ten mono-axial tensile stress cycles, along the x-direction and ranging from 0 to 32 kN, was applied to a pre-demagnetized rectangular specimen with 100 μm width slot, shown in figure 4.13 (1). This specimen configuration has been used to study the initiation and propagation of a crack raised on the slot tip.

A magnetic hysteresis loop due to the tensile stress cycles was measured using Hall probe field sensor above the sample in two different positions, in proximity of the slot tip and 20 mm far away from it. The hysteresis strength at slot tip position was ten times greater than the value measured 20 mm away from the slot tip. as expected, this effect is correlated to the increased number of dislocations around the slot tip and the decreased density moving far away from it. More information on this analysis is reported in [17].

To detect the plastic deformation produced by the tensile stress, magnetic measurements of specimen 1 have been carried out on the tip slot area before and after stress cycles. The magnetic images are obtained with a scan step size of 200 μm and a sensor-to-sample distance of 5 mm. Results are shown in figure 4.14, where 2D

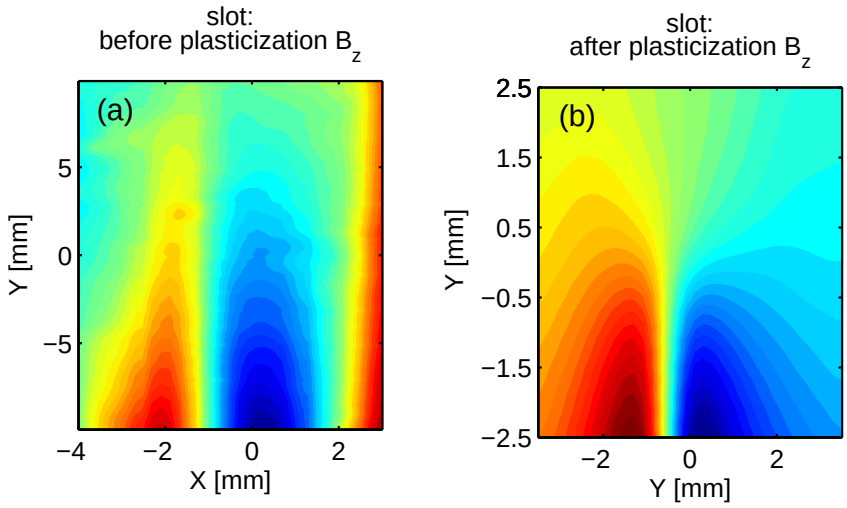

Figure 4.14: *2D magnetic maps of magnetic field component B_z measured on slot tip (as marked by the dashed box in fig. 4.13 (1)) before the tensile stress (a) and after the mechanical load (b).*

magnetic maps reporting the normal component of the magnetic field B_z measured before any tensile stress cycle (a) is compared with the magnetic field component B_z measured after applying tensile stress cycles (b). It could be noted that there is a remanent magnetization concentrated around the slot border, represented by the positive and negative area (red and blue area, respectively). This magnetization distribution is evident also after the demagnetization process (fig. 4.14 (a)). The

magnetic field varies in the range of $\pm$ 15μT before applying the tensile stress and $\pm$ 20μT after the mechanical load.

In addition, we can observe that the effect of mechanical stress on the slot tip can be enhanced if we report the magnetic field gradient dB_z/dx, as shown in figure 4.15, where a comparison between the direct signal B_z acquired by the SQUID sensor and the gradient of signal dB_z/dx across the slot tip has been reported. In particular, in figure 4.15 (a), the 2D magnetic map of the direct signal B_z measured by the sensor and corresponding to the slot tip has been reported. This signal can be compared with the magnetic field gradient dB_z/dx (figure 4.15 (b)), where it is more evident a well-defined circular area around the tip, that represents the plastic deformation. In figure 4.15 (c), a zoom area close to the tip, marked by the dashed box in figure 4.15 (a), is shown. This signal can be again compared with the magnetic field gradient dB_z/dx (figure 4.15 (d)), where it is more clear the magnetic deformed area, which represents the crack initialization.

Based on our experience, the magnetic DC technique using SQUID microscope could allow to detect the dynamic evolution of magnetic dislocation arising from different mechanical tensile stress cycles until crack initialization and the consequent specimen failure.

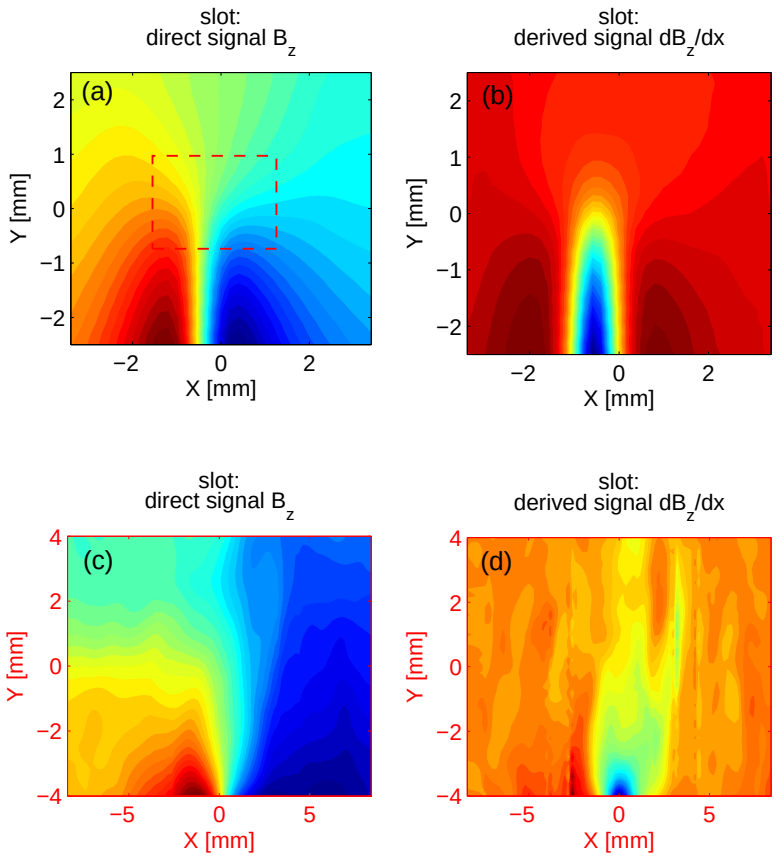

Figure 4.15: *2D magnetic map comparison between the direct signal B_z acquired by the SQUID sensor and the signal gradient dB_z/dx across the slot tip. (a) direct signal B_z measured by the sensor in the correspondence of the slot tip and (b) magnetic field gradient dB_z/dx of the same area; (c) is the direct signal of the zoomed area, marked by dashed box in (a), and (d) is the the gradient signal on the same zoomed area.*

4.3.2 Imaging dislocations in steel due to tensile deformation

In the second example, only one mono-axial tensile stress cycle, along the x-axis and ranging from 0 to 40 kN, was applied to a pre-demagnetized dog-bone shaped specimen, shown in figure 4.13 (2). This specimen configuration gives the possibility to investigate the effect of plastic deformation detecting the surface slip bands.

A magnetic hysteresis loop due to the tensile stress cycle was measured using Hall probe field sensors. This means that the residual magnetization of the sample is affected by the applied tensile stress in a reversible way. However, to detect the magnetic field variation induced by the interaction between the dislocation motion and the magnetization, magnetic measurement of specimen 2 has been carried out on a scanning area with visible slip bands, as marked by the dashed box in figure 4.16 (a).

In figure 4.16 (b), the 2D magnetic map of the direct signal B_z measured by the sensor and corresponding to some slip bands has been reported. The magnetic image is obtained with a scan step size of 100 μm and a sensor-to-sample distance of 5 mm. As we can observe, the dislocation signal was not easily distinguishable by the overall residual magnetization of the sample. For this reason, we reported the magnetic field gradient dB_z/dx, in figure 4.16 (c), where the two slip bands are more evident. Typically, these slip bands precede the fatigue crack initialization after plastic deformation.

The SQUID microscope inspection, thanks to its high sensitivity to low magnetic field and good spatial resolution, allowed us to detect and localize the band position.

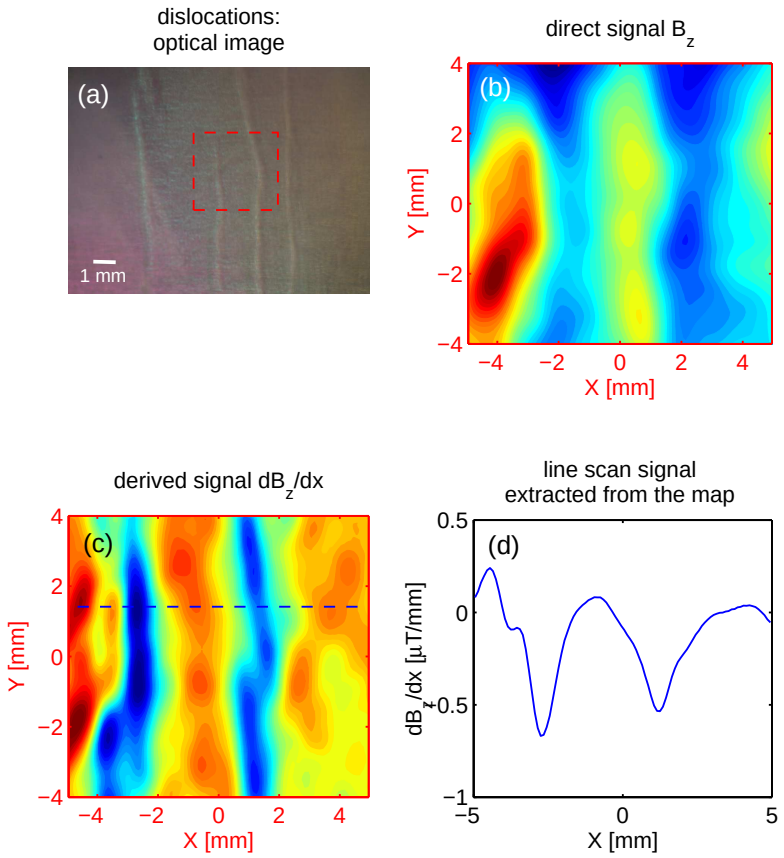

Figure 4.16: *Magnetic field measurements induced by the interaction between the dislocation motion and the magnetization sample. (a) Visible slip band optical image; (b) the 2D magnetic map of the direct signal B_z measured on the slip bands (marked by dashed box in (a)); (c) magnetic field gradient dB_z/dx on the same area; (d) line scan trough two slip bands as marked by the dashed lines in (c).*

Since it is evident that the slip bands are already visible on the sample surface, the magnetic field gradient yielded useful information on the presence of slip bands. The increment of this density is a consolidated precursor of strain-hardening phenomenon and thus its detection represents a very important information concerning material properties before the fracture is reached. Moreover, by means of SQUID microscope detection, it is possible to obtain information about magnetization strength due to the single slip band. In this way, it is possible to study where the mechanical stress produces locally changes of the sample magnetization. An example of that is presented in figure 4.16 (d), where a single line scan, extracted by the magnetic field map as marked by the dashed lines in figure 4.16 (c), has been reported. The line plot represents the normal component of the magnetic field gradient across two slip bands.

Conclusions

In this research activity a Non Destructive Analysis (NDA) for the investigation of surface and sub-surface material properties based on a high-resolution Scanning Magnetic Microscope for room-temperature objects has been presented.

The magnetic sensor used in this activity is a Superconducting QUantum Interference Device (SQUID), which is the most sensitive detector of magnetic flux that is currently available. The present work used a semi-commercial Scanning Magnetic Microscope prototype (SMM-770 model, by Tristan Technologies), equipped with liquid-nitrogen cooled SQUID sensor, which has been purchased in the framework of the regional project "Centro di Competenza Regionale per la valorizzazione e fruizione dei Beni Culturali e Ambientali" (CRdC-INNOVA).

The first part of this work has been dedicated to the set-up of the SSM prototype and to its implementation. An accurate analysis in terms of spectral density noise of the sensor and external sources of noise has been performed. The first evident source of noise has been identified in the moving mechanism used to scan the sample under the sensor. Indeed, during the measurement, the movement of the stepper motors increases the environmental spectral density noise detected by the sensor of about 10 times at 100 Hz. For this reason, we have proposed to the manufacturing industry a

modification of the system software control, assuring that the motors are turned off when the sensor is fixed in a measurement position. Although we used such caution, a DC signal carried by a remanent magnetization of the metallic parts, which form the rotational mechanisms, in principle cannot be reduced. However, we obtained an enhancement of the signals by subtracting the sample-signal and the background signal (that is a measurement obtained without the sample). In this way, we achieved a further reduction of the intrinsic noise of the system and the best value we measured for the smallest measurable magnetic field variation is of order of 0.2 -0.3 nT.

The efforts in this direction and the optimization of such aspects, as consequence of a strictly collaboration with the Tristan Technologies, have actually made our SSM as a reference system for their international customers. In this way, a frequent exchange of mutual knowledge is going on.

The second part of this work is completely dedicated to the analysis of samples at room-temperature by means of SSM. The sensitivity of the SQUID sensor at low frequencies allows to work as eddy-current sensor with high depth resolution. This was used to detect flaw on paramagnetic materials. The development of SSM in the field of eddy current non-destructive evaluation (NDE), is possible by the good combination of sensitivity of about 20 pT/$\sqrt{Hz}$ and spatial resolution of order of 70 μm of sensor, which are actually the best values compared with the other common sensors (flux gate, Hall probe, GMR, etc.) used for such applications.

Non destructive testing are used to determine the integrity of the structures and flaw detection, as requirement of quality controls. This technique is widely applied to search for flaws in joined metallic structures for aeronautical applications (part

of fuselage or wings). The detection of hidden defects has been widely carried out, focusing the attention on the enhancement of the signal flaw response with respect to the rivet signal on the surface. Indeed, hidden flaws, 100 μm wide, located under two aluminium-titanium alloy plates has been well detected at distance more than 10 mm under the surface. To obtain these results, we have applied the method of *phase rotation analysis*, which is an innovative way to enhance the signatures of the signal under the surface respect to the signal on the surface. This method is based on the principle of penetration depth of the eddy current analysis. Indeed, an important property of a defect signal is the variation of its own phase, as a function of its depth under the surface. The results obtained in this work applying such method are really competitive in this field.

We have also developed a theoretical model describing eddy current distributions, generated by a circular flaw, in a "thin" conducting plate. In this assumption, we can neglected the magnetic field variation along the thickness of the sample. Although this hypothesis introduces a simplification of the problem, the solution of the *diffusion equation*, used to describe electromagnetic problems in the intermediate frequency range, become quickly complex in the presence of flaws. However, the novel analytical solution we found is in good agreement with the experimental one and has been used to analyze the response of the SQUID sensor in presence of flaws.

The last section is focused on the investigation of novel methods and new prospects of SSM employment. We have exploited the SQUID capabilities that make it suitable to image magnetic domain structures in ferromagnetic objects. Since the spatial resolution of the system allows to visualize magnetic domains of order of 70 μm, a

theoretical approach, which describes the magnetic source as magnetic moments of "extended" dipoles, has been developed. The model shows a great agreement with the experimental data and it has helped us to obtain a good interpretation and a better perspective of our results. Two innovative fields of application have been proposed.

One of this provides a direct imaging of the magnetic particle dipoles on samples with ferromagnetic components (for example, on magnetic data storage or ancient mural paintings). These information may be useful to estimate quite simply the sample magnetization, and in same cases, to follow the variation of the magnetic dipole orientations when they are subject to an external applied magnetic field. For example, one could use this effect to provide dating of ancient work arts.

The second application concerns the requirement to estimate non destructively the degradation of structural metallic alloys, as a consequence of local plastic deformation due to fatigue cycles, especially crack formation as a precursor of failure. Due to the capability of SQUID sensor to work in relatively high external magnetic field, the significant microstructural changes (*dislocation* movement), which occur during the fatigue stages, can be detected with high spatial resolution. The results are novelty in this field. At present time, in a stress-strain mechanical test, the sample is subject to a different numbers of fatigue cycles until it reaches the rupture. This method may be used to follow the different stages of fatigue cycle and search for crack initialization as failure precursor. This point is useful in applications in which safety or on-line quality control in critical structures, such as nuclear pressure vessel, ship hulls, etc, is required.

In the next future, we will focus our research on *eddy current* non destructive

analysis applied to innovative aeronautical structures, such as composite materials. In the same way, also the *injection current* technique has shown high resolution and field sensitivity to search for fault currents. Several electronic devices have successfully been tested. For this reason we think that also electronic industry may derive benefits from this SSM application.

In summary, the SSM prototype has been carefully tested and optimized in terms of spatial resolution and field sensitivity. Both theoretical and experimental progress for NDA on materials of aeronautical interests has been done. Novel applications, such as NDA for electronic industry or cultural heritage, have been successfully investigated. We believe that the SSM may give further benefits also in other unexplored research fields.

Bibliography

[1] D. Drung (a). Advenced SQUID read-out electronics. *in: H. Weinstock and R. W. Ralston (Ed.),* SQUID *Sensors: Fundamentals, Fabrication and Applications, NATO ASI serie E, vol. 329, Kluwer, Dordrecht*, pages 63–116, 1996.

[2] M. Adamo (a), C. Nappi, and E. Sarnelli. Magnetic dipole imaging by a scanning magnetic microscope. *Meas. Sci. Technol.*, 19:1–10, 2008.

[3] K. Allweins, G. Gierelt, H.-J. Krause, and M.v. Kreutzbruck. Defect dtection in thick aircraft samples based on HTS SQUID Magnetometry and pattern recognition. *IEEE Trans. Appl. Supercond.*, 13:250–253, 2003.

[4] P. W. Anderson and J. M. Rowell. Probable observation of the Josephson superconducting tunneling effect. *Phys. Rev. Lett.*, 10:230–232, 1963.

[5] D. Drung (b). High-T_c and low-T_c dc SQUID electronics. *Supercond. Sci. Technol.*, 16:1320–1336, 2003.

[6] M. Adamo (b), C. Nappi, and E. Sarnelli. Eddy current solution for circular flaws in conducting thin plate. *Unpublished.*

[7] J. Bardeen, L. N. Cooper, and J. R. Schrieffer. Microscopic theory of superconductivity. *Letters to the Editor*, 1957.

[8] A. Barone and G. Paterno. Physics and applications of the Josephson effect. *John Wiley and Sons, New York*, 1982.

[9] F. Baudenbacher, L. E. Fong, J. R. Holzer, and M. Radparvar. Monolithic low-transition-temperature superconducting magnetometers for high resolution imaging magnetic fields of room temperature samples. *Appl. Phys. Lett.*, 82(20):3487–3489, 2003.

[10] F. Baudenbacher, N. T. Peters, P. Baudenbacher, and J. P. Wikswo Jr. High resolution imaging of biomagnetic fileds generated by action currents in cardiac tissue using LTS-SQUID microscope. *Physica C*, 368:24–31, 2002.

[11] F. Baudenbacher, N. T. Peters, and J. P. Wikswo Jr. High resolution low-temperature superconductivity superconducting quantum interference device microscope for imaging magnetic fields of samples at room temperatures. *Rev. Sci. Instrum.*, 73(3):1247–1254, 2002.

[12] J. G. Bednorz and K. A. Müller. Possible high-T_c superconductivity in the Ba-La-Cu-O system. *Z. Phys.*, B64:189–193, 1986.

[13] R. C. Black, A. Mathai, F. C. Wellstood, E. Dantsker, A. H. Miklich, D. T. Nemeth, J. J. Kingston, and J. Clarke. Magnetic microscopy using a liquid nitrogen cooled $YBa_2Cu_3O_7$ superconducting quantum interference device. *Appl. Phys. Lett.*, 62(17):2128–2130, 1993.

[14] R. C. Black, F. C. Wellstood, E. Dantsker, A. H. Miklich, J. J. Kingston, D. T. Nemeth, and J. Clarke. Eddy-current microscopy using a $77-\mathrm{K}$ superconducting sensor. *Appl. Phys. Lett.*, 64(1):100–102, 1994.

[15] R. C. Black, F. C. Wellstood, E. Dantsker, A. H. Miklich, D. Koelle, F. Ludwig, and J. Clarke. Imaging radiofrequency fields using a Scanning SQUID Microscope. *Appl. Phys. Lett.*, 66(10):1267–1269, 1995.

[16] R. C. Black, F. C. Wellstood, E. Dantsker, A. H. Miklich, D. T. Nemeth D. Koelle, F. Ludwig, and J. Clarke. Microwave microscopy using

a Superconducting Quantum Interference Device. *Appl. Phys. Lett.*, 66(1):99–101, 1995.

[17] C. Bonavolontà, M. Valentino, M. Adamo, and E. Sarnelli. Detection of plastic deformation in structural steel using scanning SQUID microscopy. *Meas. Sci. Technol.*, 18:2116–2120, 2007.

[18] A. I. Braginski. Fabrication of high-temeprature SQUID magnetometers. *in: H. Weinstock and R. W. Ralston (Ed.),* SQUID *Sensors: Fundamentals, Fabrication and Applications, NATO ASI serie E, vol. 329, Kluwer, Dordrecht*, pages 235–288, 1996.

[19] A.I. Braginski and H.-J. Krause. Nondestructive evaluation using high-temperature SQUIDs. *Physica C*, 335:179–183, 2000.

[20] Y. Bruynseraede, C. Vlekken, C. Van Haesendonck, and V. V. Moshchalkov. Fundamentals of Giaever and Josephson tunneling. *in: H. Weinstock and R. W. Ralston (Ed.), The New Superconducting Electronics, NATO ASI serie E, vol. 251, Kluwer, Dordrecht*, pages 1–28, 1993.

[21] S. Chatraphorn, E. F. Fleet, F. C. Wellstood, and R. C. Black. Imaging high-frequency magnetic and electric fields using a high-T_c SQUID microscope. *IEEE Trans. Appl. Supercond.*, 9(2):4381–4384, 1999.

[22] S. Chatraphorn, E. F. Fleet, F. C. Wellstood, L. A. Knauss, and T. M. Eiles. Scanning SQUID microscopy of integrated circuits. *Appl. Phys. Lett.*, 76(16):2304–2306, 2000.

[23] G. Chiari and R. Lanza. Pictorial remanet magnetization as an indicator of secular variation of the Earth's magnetic field. *Phys. Earth. Planet.*, 101:79–83, 1997.

[24] Y. Choua, L. Santandrea, Y. Le Bihan, and C. Marchand. Specific developments on a finite element tool for thin crack modelling in EC testing. *Proceedings of ECNDT*, 2006.

[25] Clarke. Squid fundamentals. *in: H. Weinstock and R. W. Ralston (Ed.),* SQUID *Sensors: Fundamentals, Fabrication and Applications, NATO ASI serie E, vol. 329, Kluwer, Dordrecht*, pages 1–62, 1996.

[26] J. Clarke. Small-scale analog applications of high transition temperature superconductors. *Nature*, 333:29–35, 1988.

[27] J. Clarke, W. M. Goubau, and M. B. Ketchen. Tunnel Junction Dc SQUID - Fabrication, Operation, and Performance. *J. Low Temp. Phys.*, 25(1-2):99–144, 1976.

[28] J. Clarke and R. H. Koch. The impact of high-temperature superconductivity on squid magnetometers. *Science*, 242:217–223, 1988.

[29] J.R. Claycomb, N. Tralshawala, H.M. Cho, M. Boyd, Z. Zou, X.W. Xu, and J.H. Miller Jr. Simulation and design of a superconducting eddy current probe for nondestructive testing. *Rev. Sci. Instrum.*, 69:499–506, 1998.

[30] E. D. Dahlberg and R. Proksch. Magnetic microscopies: the new additions. *J. Magn. Magn.*, 200:720–728, 1999.

[31] E. Dantsker, S. Tanaka, and J. Clarke. High-t_c SQUIDs with slots or holes: low $1/f$ noise in ambient magnetic field. *Appl. Phys. Lett.*, 70:2037–2039, 1997.

[32] B. S. Deaver and W. M. Fairbank. Experimental evidence for quantized flux in superconducting cylinders. *Phys. Rev. Lett.*, 7:43–46, 1961.

[33] M. S. Dilorio, S. Yoshizumi, M. Maung, K.-Y. Yang, J. Zhang, and N. Q. Fan. Manufacturable low-noise SQUIDs operating in liquid nitrogen. *Nature*, pages 513–515, 1991.

[34] C.V. Dodd and W.E. Deeds. Analytical solutions to eddy-current probe-coil problems. *J. Appl. Phys.*, 39:2829–2838, 1968.

[35] C. Dolabdjian, A. Qasimi, D. Bloyet, and V. Mosser. Spatial resolution of SQUID magnetometers and comparison with low noise room temperature magnetic sensors. *Physica C*, 368:84–84, 2002.

[36] G.B. Donaldson, A. Cochran, and D.A. McKirdy. The use of SQUIDs for nondeestructive evaluation. *in: H. Weinstock (Ed.),* SQUID *Sensors: Fundamentals, Fabrication and pplications, NATO ASI serie E, vol. 329, Kluwer, Dordrecht*, pages 599–628, 1996.

[37] D. Drung, R. Cantor, M. Peters, H. J. Scheer, and H. Kock. Low-noise high-speed dc superconducting quantum inteference device magnetometer with semplified feedback electronics. *Appl. Phys. Lett.*, 57(4):406–408, 1990.

[38] D. Drung, F. Ludwig, W. Müller, U. Steinhoff, L. Trahms, Y. Q. Shen, M. B. Jensen, P. Vase, T. Holst, T. Freltoft, and G. Curio. Integrated $YBa_2Cu_3O_{7-x}$ magnetometer for biomagnetic measurements. *Appl. Phys. Lett.*, 68:1421, 1996.

[39] D. Duret and P. Karp. Figure of merit and spatial resolution of superconducting flux tranformers. *J. Appl. Phys.*, 55(6):1762–1768, 1984.

[40] M. I. Faley, K. Pratt, R. Reineman, D. Schurig, S. Gott, C. G. Atwood, R. E. Sarwinski, D. N. Paulson, T. N. Starr, and R. L. Fagaly. High temperature superconductor dc SQUID micro-susceptometer for room temperature objects. *Supercond. Sci. Technol.*, 17:S324–S327, 2004.

[41] E. F. Fleet, S. Chatraphorn, F. C. Wellstood, L. A. Knauss, and S. M. Green. Closed-cycle refrigerator-cooled scanning SQUID microscope for room-temperature samples. *Rev. Sci. Instrum.*, 72(8):3281–3290, 2001.

[42] V. Foglietti, W. J. Gallagher, M. B. Ketchen, A. W. Kleinsasser, R. H. Koch, S. I. Raider, and R. L. Sandstrom. Low-frequency noise in low $1/f$ noise dc SQUID's. *Appl. Phys. Lett.*, 49(20):1393–1395, 1986.

[43] L. E. Fong, J. R. Holzer, K. K. McBride, E. A. Lima, F. Baudenbacher, and M. Radparvar. High-resolution room-temperature sample scanning superconducting quantum interference device microscope configurable for geological and biomagnetic applications. *Rev. Sci. Instrum.*, 76:1–9, 2005.

[44] Y. Gim, A. Mathai, R. C. Black, A. Amar, and F. C. Wellstood. Angular dependence of the symmetry of the order parameter in $YBa_2Cu_3O_{7-\delta}$. *IEEE Trans. Appl. Supercond.*, 7(2):2331–2334, 1997.

[45] H. L. Grossman, Y. R. Chemla, T. S. Lee, J. Clarke, M. Adamkiewicz, and B. B. Buchanan. Squid detection of magnetic bacteria. *Biophys. J.*, 78(1):267A, 2000.

[46] F. Gruhl, M. Mück, M. von Kreutzbruck, and J. Dechert. A scanning superconducting quantum interference device microscope with high spatial resolution for room temperature samples. *Rev. Sci. Instrum.*, 72(4):2090–2096, 2001.

[47] S. A. Gudoshnikov, N. N. Ukhansky ans I. I. Vengrus, K. E. Andreev, A. M. Tishin, and O. V. Snigirev. A dc SQUID-based magnetic microscope study of the magnetic properties of Ni thin films. *IEEE Trans. Appl. Supercond.*, 7(2):2542–2544, 1997.

[48] S. A. Gudoshnikov, M. I. Koshelev, A. S. Kalabukhov, L. V. Matveets, M. Mück, J. Dechert, C. Heiden, and O. V. Snigirev. A scanning high-T_c dc SQUID microscopy of the $YBa_2Cu_3O_{7-\delta}$ thin-film samples at 77 K. *Paper presented at Applied Superconductivity Conference, 14-17 September, Spain*, 2:541–544, 1999.

[49] S. A. Gudoshnikov, O. V. Snigirev, and A. M. Tishin. Study of the magnetic recording media using a dc SQUID microscope. *Paper presented at Applied Superconductivity Conference, 14-17 September, Spain*, 2:553–556, 1999.

[50] Y. Hata, J. Suzuki, I. Kakeya, K. Kadowaki, A. Odawara, A Nagata, S. Nakayama, and K. Chinone. Flux quantization in a superconducting microdisk. *Physica C*, 388-389:719–720, 2003.

[51] T. Hayashi and H. Itozaki. The fine magnetic image of a high T_c SQUID probe microscope. *Supercond. Sci. Technol.*, 18:112–115, 2005.

[52] H. Hilgenkamp and J. Mannhart. Grain boundaries in high-T_c superconductors. *Reviews of Modern Physics*, 74(2):485–549, 2002.

[53] H.E. Horng, J.T. Jeng, H.C. Yang, and J.C. Chen. Evaluation of the flaw depth using high-T_c SQUID. *Physica C*, 367:303–307, 2002.

[54] A. Hubert, W. Rave, and S. L. Tomlinson. Imaging magnetic charges with magnetic force microscopy. *Phys. Stat. Sol.*, 204:817–828, 1997.

[55] I. Iguchi, A. Sugimoto, T. Yamaguchi, N. Chaki, T. Miyake, I. Tanaka, and S. Watauchi. Observation of diamagnetic precursor to the Meissner state above T_c in high-T_c $La_{2-x}Sr_xCuO_4$ cuprates by scanning SQUID microscopy. *Physica C*, 367:9–14, 2002.

[56] I. Iguchi, T. Yamaguchi, and A. Sugimoto. Diamagnetic activity above T_c as a precursor to superconductivity in $La_{2-x}Sr_xCuO_4$ thin films. *Nature*, 412(6845):420–423, 2001.

[57] R. C. Jaklevic, J. Lambe, A. H. Silver, and J. E. Mercereau. Quantum interferference effects in Josephson tunneling. *Phys. Rev. Lett.*, 12(7):159–160, 1964.

[58] J.T. Jeng, H.E. Horng, H.C. Yang, J.C. Chen, and J.H. Chen. Similations of the magnetic field due to the defects and verification using high-T_c SQUID. *Physica C*, 367:298–302, 2002.

[59] J.T. Jeng, S.Y. Yang, H.E. Horng, and H.C. Yang. Detection of deep flaws by using a HTS-SQUID in unshielded environment. *IEEE Trans Appl Supercond*, 11(1):1295–1298, 2001.

[60] W.G. Jenks, S.S.H. Sadeghi, and J.P. Wikswo Jr. Review article: SQUIDs for nondestructive evaluation. *J. Physics D: Appl. Phys.*, 30:293–323, 1997.

[61] B. D. Josephson. Possible new effects in superconductive tunneling. *Phys. Lett*, 1:251–253, 1962.

[62] J. P. Wikswo Jr. High-resolution magnetic imaging: Cellular action currents and other applications. *SQUID Sensors: Fundamentals, Fabrication and Applications. H. Weinstock, Ed. The Netherlands: Kluwer Academic Publishers*, pages 307–360, 1996.

[63] J.P. Wikswo Jr. SQUID magnetometers for biomagnetism and nondestructive testing: important questions and initial answers. *IEEE Trans Appl Supercond*, 5(2):74–120, 1995.

[64] E. Juzeliunas, Y.P. Ma, and J. P. Wikswo. Remote sensing of aluminium alloy corrosion by SQUID magnetometry. *J Solid State Electrochem*, 8:435–441, 2004.

[65] N. Kasai, S. Nakayama, Y. HAtsukade, and M. Uesaka. Magnetic detection of mechanical degradation of low alloy steel by SQUID-NDE system. *Paper presented at Applied Superconductivity Conference, 14-17 September, Spain*, 2:557–560, 1999.

[66] M. B. Ketchen and J. M. Jaycox. Planar coupling scheme for ultra low noise dc SQUIDs. *IEEE Trans. Magn.*, MAG-17:400–403, 1981.

[67] T.-Y. Kim, J. Nishimura, T. Fukumura, M. Kawasaki, T. Hasegawa, H. Koinuma, Y. Taguchi, and Y. Tokura. Magnetic domain structure of growth temperature-gradient $Sm_2Mo_2O_7$ thin film investigated by scanning SQUID microscopy. *Physica B*, 329-330:1048–1048, 2003.

[68] J. R. Kirtley. SQUID microscopy for fundamental studies. *Physica C*, 368:55–65, 2002.

[69] J. R. Kirtley and J.P. Wikswo Jr. Scanning SQUID microscopy. *Annu. Rev. Mater. Sci.*, 29:117–48, 1999.

[70] J. R. Kirtley, M. B. Ketchen, K. G. Stawiasz, J. Z. Sun, W. J. Gallagher, S. H. Blanton, and S. J. Wind. High-resolution scanning SQUID microscope. *Appl. Phys. Lett.*, 66(9):1138–1140, 1995.

[71] J. R. Kirtley, C. C. Tsuei, Ariando, H. J. H. Smilde, and H. Hilgenkamp. Antiferromagnetic ordering in arrays of superconducting π-rings. *Phys. Rev. B*, 72:214521, 2005.

[72] J. R. Kirtley, C. C. Tsuei, K. A. Moler, V. G. Kogan, J. R. Clem, and A. J. Turberfield. Variable sample temperature scanning superconducting quantum interference device microscope. *Appl. Phys. Lett.*, 74(26):4011–4013, 1999.

[73] J. R. Kirtley, C. C. Tsuei, M. Rupp, J. Z. Sun, L. S. Yu-Jahnes, A. Gupta, M. B. Ketchen K. A. Moler, and M. Bhushan. Direct imaging of integer and half-integer Josephson vortices in high-T_c grain boundaries. *Phys. Rev. Lett.*, 76(8):1336–1339, 1996.

[74] J. R. Kirtley, C. C. Tsuei, J. Z. Sun, C. C. Chi, L. S. Yu-Jahnes, A. Gupta, M. Rupp, and M. B. Ketchen. Symmetry of the order parameter in the high-T_c superconductor $YBa_2Cu_3O_{7-\delta}$. *Nature*, 373(6511):225–228, 1995.

[75] R. H. Koch, John Clarke, W. M. Goubau, J. M. Martinis, C. M. Pegrum, and D. J. van Harlingen. Flicker $(1/f)$ noise in tunnel junction dc SQUIDs. *J. Low Temp. Phys.*, 51(1-2):207–224, 1983.

[76] R. H. Koch, W. Eidelloth, B. Oh, R. P. Robertazzi, S. A. Andrek, and W. J. Gallagher. Identifying the source of $1/f$ noise in SQUIDs made from high-temperature superconductors. *Appl. Phys. Lett.*, 60(4):507, 1992.

[77] R. H. Koch, C. P. Umbach, G. J. Clark, , P. Chaudhari, and R. B. Laibowitz. Quantum interference devices made from superconducting oxide thin films. *Appl. Phys. Lett.*, 51:200–202, 1987.

[78] D. Koelle, R. Kleiner, F. Ludwig, E. Dantsker, and J. Clarke. High-transition-temperature superconducting quantum interference devices. *Reviews of Modern Physics*, 71(3):631–686, 1999.

[79] D. Koelle, A. H. Miklich, E. Dantsker, F. Ludwig, D. T. Nemeth, J. Clarke, W. Ruby, and K. Char. High performance dc SQUID magnetometers with single layer $YBa_2Cu_3O_{7-x}$ flux transformers. *Appl. Phys. Lett.*, 63(26):3630–3632, 1993.

[80] D. Koelle, A. H. Miklich, F. Ludwig, E. Dantsker, D. T. Nemeth, and J. Clarke. Dc SQUID magnetometers from single layers of $YBa_2Cu_3O_{7-x}$. *Appl. Phys. Lett.*, 63(16):2271–2273, 1993.

[81] H.-J. Krause, R. Holmann, and M. Grüneklee amd M. Maus. Aircraft wheel and fuselage testing with eddy current and SQUID. *Insight 42*, pages 148–151, 2000.

[82] H.-J. Krause and M.v. Kreutzbruck. Recent development in SQUID NDE. *Physica C*, 368:70–79, 2002.

[83] M.v. Kreutzbruck, K. Allweins, H.J. Krause, S. Gärtner, and W. Wolf. Defect detection of thick aircraft samples using HTS SQUID magnetometer. *Physica C*, 368:85–90, 2002.

[84] M.v. Kreutzbruck, U. Baby, A. Theiss, M. Mück, and C. Heiden. inspection of aircraft parts with high remanent magnetization by eddy current SQUID NDE. *IEEE Trans. Appl. Supercond.*, 9:3805–3808, 1999.

[85] M.v. Kreutzbruck, M. Mück, U. Baby, and C. Heiden. Detection of deep lying cracks by eddy current SQUID NDE. *in: B. Larsen (Ed.), Proceedings of 7th ECNDT, Broendby, Denmark*, page ?, 1998.

[86] M.v. Kreutzbruck, M. Mück, and C. Heiden. Similations of eddy current distributions and crack detection algorithms for a SQUID based NDE system. *in: B. Larsen (Ed.), Proceedings of 7th ECNDT, Broendby, Denmark*, pages 2513–2520, 1998.

[87] T.-K. Lee, D. M. Clatterbuck, J. W. Morris Jr., T. J. Shaw, S. Lee, and J. Clarke. Detecting damage in steel with scanning SQUID microscopy. *AIP Conf. Proc.*, 615:453–459, 2002.

[88] T. S. Lee, Y. R. Chemla, E. Dantsker, and J. Clarke. High-T_c SQUID microscope for room temperature samples. *IEEE Trans. Appl. Supercond.*, 7(2):3147–3150, 1997.

[89] T. S. Lee, E. Dantsker, and J. Clarke. High-transition temperature superconducting quantum interference device microscope. *Rev. Sci. Instrum.*, 67(12):4208–4215, 1996.

[90] C. C. H. Lo, F. Tang, S. B. Biner, and D. C. Jiles. Effects of fatigue-induced changes in microstructure and stress on domain structure and magnetic properties of FeC alloys. *J. Appl. Phys.*, 87(9):6520–6522, 2000.

[91] M.L. Lucia, R. Hohmann, H. Soltner, H.-J. Krause ad W. Wolf, H. Bousac, M.I. Faley, G. Spörl, and A. Binneberg. find title. *IEEE Trans Appl Supercond*, 7:2878, 1997.

[92] Y.P. Ma and J.P. Wikswo Jr. Technique for deth-selective, low frequency eddy current analysis for SQUID-based nondestructive testing. *J. Nondestruct. Eval.*, 14:149, 1995.

[93] F. Melquiod, A. Mouroux, J. Jouglar, P. L. Vuillermoz, and H. Weinstock. History dependence of magnetomechanical properties of steel. *J. Magn. Magn. Mater.*, 157-158:571–572, 1996.

[94] M. Mück, M.v. Kreutzbruck, U. Baby, J. Troll, and C. Heiden. Eddy current nondestructive material evaluation based on HTS SQUIDs. *Physica C*, 282:3275, 1997.

[95] M. Mück, C Welzel, A. Farr, F. Schlöz, and W. Singer. Nondestructive testing of niobium sheets for superconducting resonators. *IEEE Trans Appl Supercond*, 13(2):239–244, 2003.

[96] A. Oral, S. J. Bending, and M. Henini. Real-time scanning Hall probe microscopy. *Appl. Phys. Lett.*, 69(9):1324–1326, 1996.

[97] M. Pattabiraman, J. Nagendran, and N.P. Janawadkar. Rapid flaw depth extimation from SQUID-based eddy current nondestructive evaluation. *NDT & International*, 40:289–293, 2007.

[98] W N Podney. Performance measurements of a superconductive microprobe for eddy current evaluation of subsurface flaws. *IEEE Trans Appl Supercond*, 3:1914–1917, 1993.

[99] U. Poppe, M. I. Faley, E. Zimmermann, W. Glaas, I. Breunig, R. Speen, B. Jungbluth, H. Soltner, H. Halling, and K. Urban. High temperature superconductor dc-SQUID microscope with a soft magnetic flux guide. *Supercond. Sci. Technol.*, 17:S191–S195, 2004.

[100] U. Poppe, N. Klein, U. Dähne, H. Soltner, C. L. Jia, B. Kabius, K. Urban, A. Lubig, K. Schmidt, S. Hensen, S. Orbach, G. Müller, and H. Piel. Low-resistivity epitaxial $YBa_2Cu_3O_7$ thin films with improved microstructure and reduced microwave losses. *J. Appl. Phys.*, 71(11):5572–8, 1992.

[101] A. Prigiobbo and E. Sarnelli. Effective area reduction in directly coupled superconducting quantum interference device based micromagnetometers. *J. Appl. Phys.*, 103(4):043906, 2008.

[102] R. Proksch, G. D. Skidmore, E. D. Dahlberg, S. Foss, J. J. Schmidt, C. Merton, B. Walsh, and M. Dugas. Quantitative magnetic field measurements with the magnetic force microscope. *Appl. Phys. Lett.*, 69(17):2599–2601, 1996.

[103] D. Robbes. Highly sensitive magnetometers - a review. *Sensors and Actuators A*, 129:86–93, 2006.

[104] F. P. Rogers. A device for experimental observation of flux vortices trapped in superconducting thin films. *MS MIT*, 1983.

[105] J. M. Rowell. Magnetic field dependence of the Josephson tunnel current. *Phys. Rev. Lett.*, 11:200–202, 1963.

[106] A. Sandhu, H. Masuda, A. Oral, and S. J. Bending. Room temperature sub-micron magnetic imaging by Scanning Hall Probe Microscopy. *Jpn. J. Appl. Phys.*, 40:4321–4324, 2001.

[107] M. R. Scheinfein, J. Unguris, M. H. Kelley, D. T. Pierce, and R. J. Celotta. Scanning Electron-Microscopy with Polarization Analysis (Sempa). *Rev. Sci. Instrum.*, 61(10):2501–2526, 1990.

[108] J. H. Scofield. A frequency-domain description of a lock-in amplifier. *American Journal of Physics*, 62(2):129–133, 1994.

[109] T. J. Shaw, J. W. Chan, S. H. Kang, R. McDermott, J. W. Morris Jr., and J. Clarke. Scanning SQUID microscope differentiation of ferromagnetic steel phases. *Acta Materialia*, 48:2655–2664, 2000.

[110] A. H. Silver. How the SQUID was born. *Supercond. Sci. Technol.*, 19:S173–S178, 2006.

[111] S. Tanaka, H. Fujita, Y. Hatsukade, T. Otani, S. Suzuki, and T. Nagaishi. A high-T_c SQUID micro-detector with a high performance magnetic shield for contaminant detection in industrial products. *Supercond. Sci. Technol.*, 20:S385–S388, 2007.

[112] S. Tanaka, K. Matsuda, O. Yamazaki, M. Natsume, H. Ota, and T. Mizoguchi. Development of high-T_c SQUID microscope with flux guide. *Supercond. Sci. Technol.*, 15:146–149, 2002.

[113] S. Tanaka, M. Natsume, M. Uchida, N. Hotta, T. Matsuda, Z. A. Spanut, and Y. Hatsukade. Measurement of metallic contaminants in food with a high-T_c SQUID. *Supercond. Sci. Technol.*, 17:620–623, 2004.

[114] Y. Tavrin, M. Siegel, and J.-H. Hinken. Standard method for detection of magnetic defects in aircraft engine discs using a HTS SQUID gradiometer. *IEEE Trans. Appl. Supercond.*, 9(2):3809–3812, 1999.

[115] C. D. Tesche and J. Clarke. Dc SQUID noise and optimization. *J. Low Temp. Phys.*, 29(3-4):301–331, 1977.

[116] A. Ya Tzalenchuk, Z. G. Ivanov, S. V. Dubonos, and T. Claeson. SQUID and Hall-probe microscopy of superconducting films. *Paper presented at Applied Superconductivity Conference, 14-17 September, Spain*, 2:581–584, 1999.

[117] H. W. Wang, X. Y. Kong, Y. F. Ren, H. W. Yu, H. S. Ding, S. P. Zhao, G. H. Chen, L. H. Zhang, Y L. Zhou, and Q. S. Yang. Magnetic microscopy based on high-T_c SQUIDs for room temperature samples. *Supercond. Sci. Technol.*, 16:1310–1313, 2003.

[118] Y. Watanabe, S. H. Kang, J. W. Chan, J. W. Morris Jr., T. J. Shaw, and J. Clarke. Observation of magnetic gradients in stainless steel with a high-T_c superconducting quantum interference device microscope. *J. Appl. Phys.*, 89(3):1977–1982, 2001.

[119] F. C. Wellstood, Y. Gim, A. Amar, R. C. Black, and A. Mathai. Magnetic microscopy using SQUIDs. *IEEE Trans. Appl. Supercond.*, 7(2):3134–3138, 1997.

[120] J. P. Wikswo. The magnetic inverse problem for NDE. *in: H. Weinstock (Ed.),* SQUID *Sensors: Fundamentals, Fabrication and Applications, NATO ASI serie E, vol. 329, Kluwer, Dordrecht*, pages 629–695, 1996.

[121] A. Yashan, W. Bisle, and T. Meier. Inspection of hidden defects in metal-metal joints of aircraft structures using eddy current technique with GMR sensor array. *Proceedings of ECNDT*, page poster session, 2006.

[122] J. E. Zimmerman and J. E. Mercereau. Quantized flux pinning in superconducting niobium. *Phys. Rev. Lett.*, 13(4):125–126, 1964.